Modeling Air and Temperature Flow Inside a Wind Turbine Nacelle

Diploma Thesis

submitted by
Michael Santner
on August 30th, 2010

Graz University of Technology

Institute of Hydraulic Fluidmachinery

Assessor: o. Univ.-Prof. Dr.-Ing. Helmut Jaberg

Supervisors: Ass.Prof. Dipl.-Ing. Dr.techn. Helmut Benigni
and Dipl.-Ing. Sami Jaber, AMSC Windtec

Statutory Declaration

I declare that I have authored this thesis independently, that I have not used other than the declared sources / resources, and that I have explicitly marked all material which has been quoted either literally or by content from the used sources.

Graz, August 30th, 2010   Michael Santner

Eidesstattliche Erklärung

Ich erkläre an Eides statt, dass ich die vorliegende Arbeit selbstständig verfasst, andere als die angegebenen Quellen/Hilfsmittel nicht benutzt, und die den benutzten Quellen wörtlich und inhaltlich entnommenen Stellen als solche kenntlich gemacht habe.

Graz, am 30. August 2010   Michael Santner

Preface

This diploma thesis is the final project for receiving the *Diplomingenieur* degree in mechanical engineering at the Graz University of Technology. The topic of this diploma thesis was set up by AMSC Windtec GmbH in Klagenfurt, Austria.

AMSC Windtec GmbH - company profile

Following nearly a decade of wind power development and commissioning work by its founder, Windtec was founded in 1995 in Klagenfurt, Austria and has grown to become one of the world's leading wind turbine engineering organizations. AMSC Windtec's platforms range from 600 kW land-based wind turbines to 10 MW SeaTitan^{TM} wind turbines for the offshore market. In addition to its proprietary wind turbine designs, the organization develops and provides wind turbine electrical control systems for more than a dozen companies worldwide. AMSC Windtec became a wholly owned subsidiary of American Superconductor in early 2007.

Acknowledgements

I want to thank my supervisors at the Institute of Hydraulic Fluidmachinery Mr. Helmut Benigni and Mr. Jürgen Schiffer, for their advice and support.

I also want to thank my supervisors at AMSC Windtec, Mr. Sami Jaber and Mr. Andreas Tratnig.

A very warm thank you goes to my parents for always supporting me and for offering me the possibility of studying at the Graz University of Technology, even though I didn't always follow the shortest path.

Abstract

A description is presented how the commercial CFD-codes Ansys CFX and ICEM CFD are used to achieve qualitative results predicting the flow and temperature characteristics inside a wind turbine nacelle. The *WT2000* wind energy converter of AMSC Windtec is used for this study. The various steps beginning from treating CAD data, towards grid generation until the definition of a solution run and the interpretation of the results are discussed. A grid size study is conducted and the selection of an appropriate turbulence model is presented. In order to examine the solution results for transient behavior, a transient case is calculated and discussed. A number of flow and temperature characteristics inside the presented geometry are analyzed, which were defined by the initiator of the study. The last part of this thesis presents a comparison of the CFD results with measured values from a similar wind energy converter. The measurements were taken and provided by AMSC Windtec.

Kurzfassung

Der Einsatz der kommerziellen CFD Softwarepakete Ansys CFX und ICEM CFD zur qualitativen Vorhersage von Strömungs- und Wärmetransport innerhalb der Gondel einer Windkraftanlage wird beschrieben. Die Windkraftanlage WT2000 der Firma AMSC Windtec wird in dieser Arbeit untersucht. Beginnend mit der Bearbeitung der CAD Daten, über die Gittererstellung bis zur Definition eines Lösungsdurchlaufs und der Analyse der Ergebnisse werden die einzelnen Schritte diskutiert. Eine Rechengitter-Studie wird durchgeführt und die Auswahl eines geeigneten Turbulenzmodells wird vorgestellt. Um die Lösung auf transiente Einflüsse zu untersuchen wird ein transienter Solver-Lauf durchgeführt und die Ergebnisse diskutiert. Die Analyse einer Reihe von Strömungs- und Wärmetransport-Charakteristiken innerhalb der vorgestellten Geometrie wird durchgeführt, die vom Auftraggeber der Studie vorgeschlagen wurden. Im letzten Teil werden die Berechnungsergebnisse mit Messdaten von einer ähnlichen Windkraftanlage verglichen. Die Messdaten wurden von AMSC Windtec zur Verfügung gestellt.

Contents

Contents

1 Introduction

"Wind energy is perhaps the most advanced of the 'new' renewable energy technologies, but there is still much work to be done." This is certainly true when looking at the estimated goal of installing 2000 GW of worldwide installed capacity of wind energy converters until 2050. In 2008, there were 121 GW of worldwide installed capacity. [12]

Much work is to be done indeed, but an increase of the production capacities alone cannot bring us closer to this ambitious goal. Policy frameworks must create a further pull from the market side. Technology research and development must do their part to increase reliability and performance of wind turbines while reducing costs at the same time. Especially in the offshore market, a growth in size is to be expected to reduce costs due to the economy of scale and an increase of efficiency.

However, the development of larger wind turbines challenges researchers and engineers. When it comes to the thermal management of wind energy converters, the point of interest for this study becomes clear. An increase of power output will also lead to an increased heat release due to losses, as efficiency will unlikely rise at the same pace as the size of the wind energy converters does. Consequently, the thermal management inside the nacelle must be rethought and improved. To do this, computational fluid dynamics can be an indispensable tool. As stated by Smaïli, "the wind turbine industry would inevitably benefit from CFD tools" [14].

The cooling and heating characteristics inside a wind turbine nacelle play a major role in stop/operate scenarios of a wind turbine. It also affects gearbox and generator performance and their cooling system life. Electrical parts like converters and controllers need a suitable environment to operate in optimum performance. 3D flow and thermal calculation is needed to study these characteristics.
From the specification for this diploma thesis by AMSC Windtec.

Smaïli et al. and other groups have conducted two-dimensional approaches to predict the temperature situation inside a wind turbine nacelle already in the past, see [14]. Their studies were focused on the thermal management of a wind turbine nacelle. They also included the surrounding environment, i.e. the surrounding air of the nacelle. The generator (the main heat source) and the heat transfer through the hull of the nacelle were modeled. However, this was all done in two dimensions and with a very simple model of the geometry. They conclude that in order to "take typical physical problems (such as the buoyancy effect) into account, a three-dimensional formulation should be developed".

This diploma thesis shall make a first step into this direction. Buoyancy effects are taken into account and much emphasis is put on a detailed, three-dimensional geometric model of the nacelle.

The wind energy converter WT2000 is used for this study. One part of the present thesis is a detailed description of how the CAD files were converted, imported and processed, how the grid was generated and how the solution was set up using the commercial CFD code Ansys CFX and the grid generation code ICEM CFD. This part of the documentation was explicitly requested by AMSC Windtec.

2 Treatment of CAD Data

2.1 File Conversion

The CAD data of the wind turbine nacelle was delivered as Unigraphics NX 6 (UG) files. It was necessary to convert these files to a Pro/Engineer file format. This was done by using the export function in UG to create STEP files, which were imported into Pro/Engineer. However, the UG files contained by far too many details and therefore were too big to be processed in one step. Hence the geometry had to be segmented and exported in several parts.

2.2 Geometry Simplification

As already mentioned, the grade of detail of the data received was very high. Consequently, the first step was the simplification of the geometry, leaving away details which would not be of big influence for the expected results. Two different methods were applied in order to achieve a geometry with a sufficient grade of detail for the calculations.

2.2.1 Deleting Unnecessary Parts and Repairing Geometry

The first attempt was, to start from the original UG files with their very high grade of detail. It was tried to delete any unnecessary part and any detail which would not decisively influence the results. However, important problems were encountered when elements of the geometry were deleted, as the remaining parts very often were incomplete and had to be repaired.

Repairing the remaining parts was very difficult and time-consuming. Moreover, the resulting geometry was still too detailed and it would certainly not have been possible to create a structured grid of high quality in a reasonable amount of time. Hence, a different approach to simplify the geometry was necessary.

2.2.2 Rebuilding Important Parts Using the Original Geometry as a Guideline

The second attempt was, to start with a blank file in Pro/Engineer and reverse engineer only the essential parts of the original geometry. This was successfully done using the original data as a guideline. The UG files were imported into Pro/Engineer and all unnecessary parts were deleted in order to keep the representation of the main geometry clear. Cross-sections of the original geometry were made. The cross-sections were combined to a framework using Pro/Engineers surface creating functions in order to rebuild the geometry.

It was possible to achieve a simple and clean geometry which was exported as a number of STEP files, one for each part of the geometry. These files contained only surface definitions. They were imported into ICEM CFD where all the parts were combined in one file. It was not necessary to apply any transformation of the coordinate systems, so the assembly of the geometry parts in ICEM CFD was very straight-forward.

2.3 Presentation of the Final Geometry

The simplified geometry is displayed in figure 2.1. The hull of the nacelle and the tower segment are transparently displayed, so that the inner parts of the geometry can be seen. Apart from the two inlets at the hull and through the tower, no other inlets were defined. Leakages between the tower and the hull and the tower and the spinner (not represented) were neglected. For comparison, figure 2.2 displays a screenshot of the unchanged CAD data.
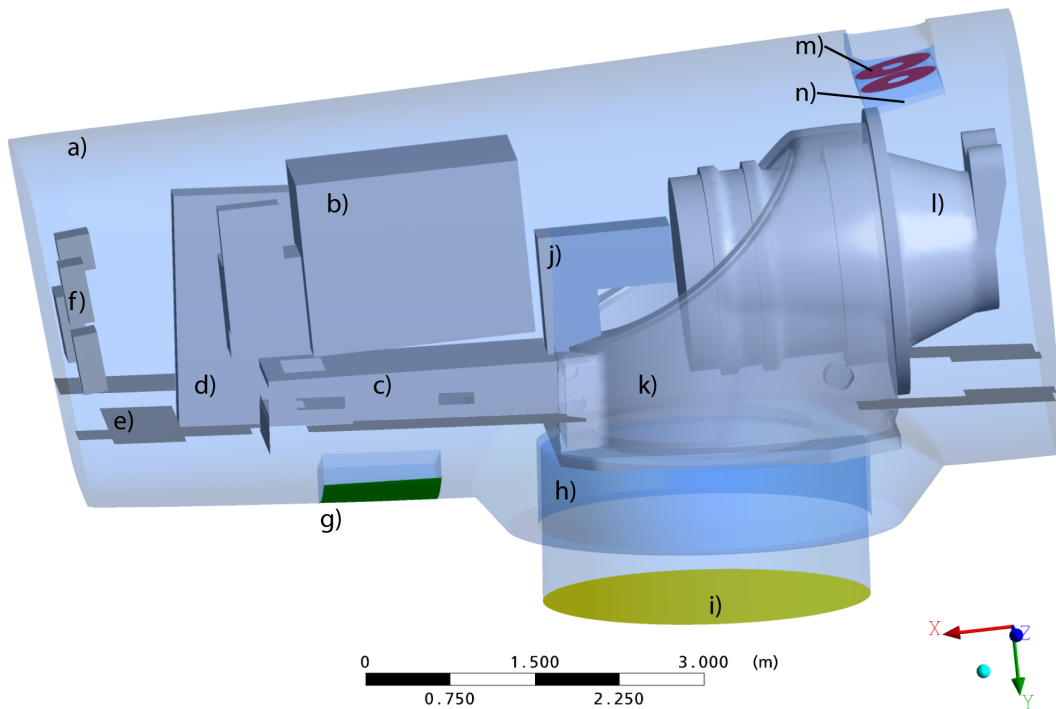
Figure 2.1: The simplified, rebuilt geometry

a) hull

b) generator

c) generator support

d) converter cabinet

e) floor elements

f) small control cabinets

g) hull inlet (green)

h) tower segment

i) tower inlet (yellow)

j) brake

k) mainframe

l) gearbox

m) outlet fans (purple)

n) gearbox oil-air heat exchanger

Figure 2.2: Screenshot of the original geometry

3 Generation of the Grid Using ICEM CFD

As the geometry of the wind turbine nacelle is very complex (see figure 2.2) and large in dimensions, it was obvious to split the problem into parts. The idea was, to simplify the mesh generation process by treating smaller parts of the problem at a time. Secondly, one can avoid re-meshing the whole geometry in case of changes to only a small part of the geometry. As an example, it would be possible to re-mesh only that part of the grid where the generator is situated in case that this component was replaced, changed or moved. Consequently, only the affected part or parts of the grid must be re-meshed and not the whole grid.
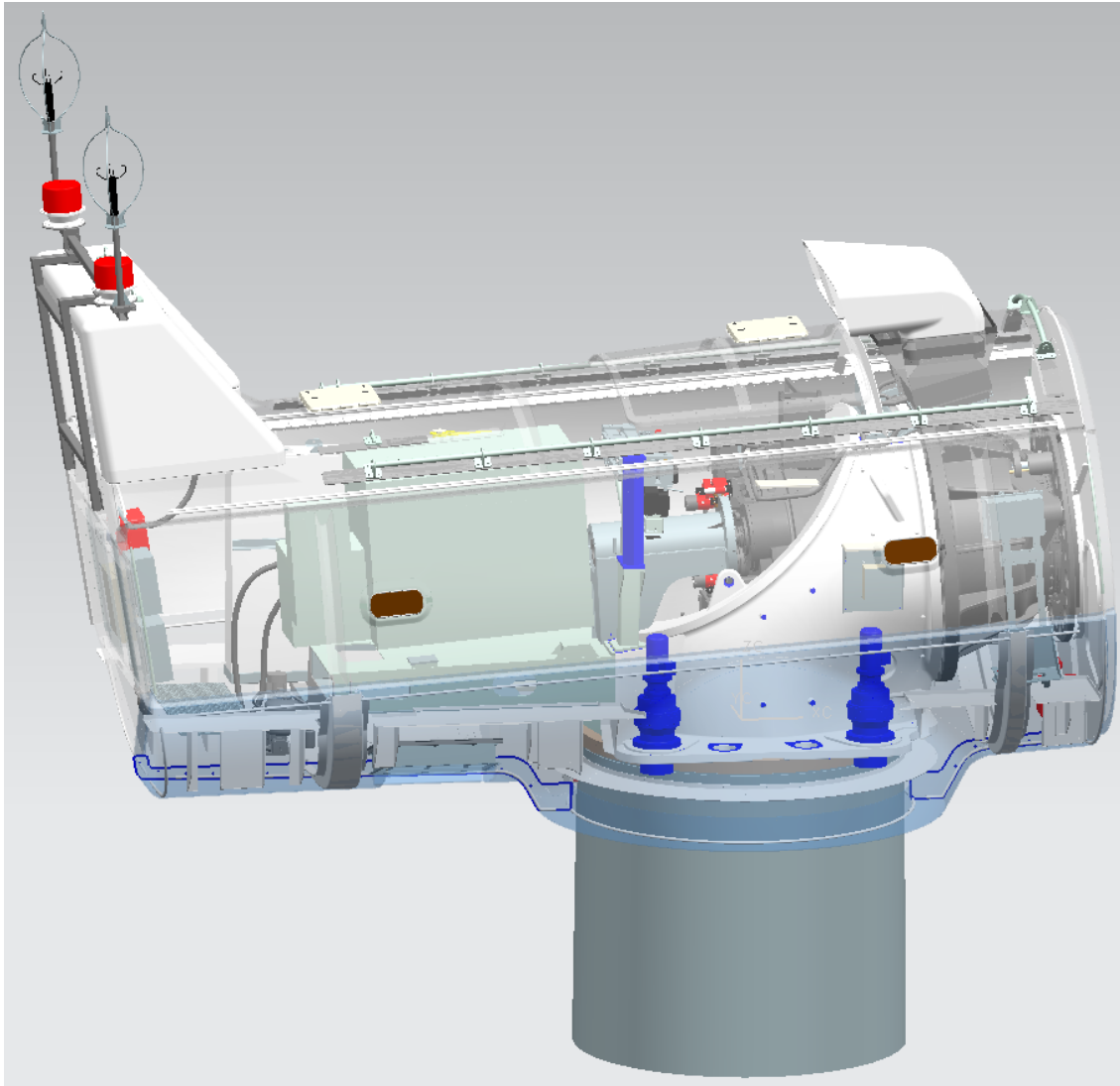
During the mesh generation process it became evident that a structured mesh can only be achieved on a geometry like this if the whole problem is split into parts. Complex geometry in combination with structured meshes leads to a very high number of elements in regions where no refinement is needed (very often in free stream regime) and, therefore, to a high consumption of memory, disk-space and CPU-time. So, the geometry was split into several parts which were meshed separately. This partly solved the problem with the refinement in the free stream regime. The different grid parts were later combined in Ansys Pre. The available steps will be described in detail in the following sections.

3.1 Splitting the Geometry into Parts

After the import of the geometry parts into one file in ICEM CFD, split surfaces were created directly in ICEM CFD. These surfaces were used to separate one grid part from the neighboring and later would serve to define the interfaces between the grid parts. After these surfaces were defined, a copy of the ICEM project file was saved and geometry details and interface surfaces were deleted, until only one geometry region necessary for a certain grid part was left. The presented process guarantees that the position of a single grid part is consistent in relation to the other parts, i.e. they use the same original coordinate system. Furthermore, the interface surfaces were identical and at the same position. These steps were repeated for each grid part resulting in several ICEM CFD project files, each representing one grid part. Each of these projects was then individually processed during mesh generation, resulting in a number of grids. Depending on the complexity of a given geometry part, either an unstructured topology for very complex geometries, or a structured grid topology was used.

The subdivision into the grid parts is displayed in figure 3.1. The transparently displayed surfaces represent the split surfaces and the domain interfaces at the same time. In the large representation, the grid part *Huelle* is hidden to better visualize the inner grid parts. In the top left corner, a small image of this grid part is given. It encloses the inner parts and contains mainly the wall-near grid at the cover of the nacelle. A small portion of the grid part *Turm* is also visible in the top left image.

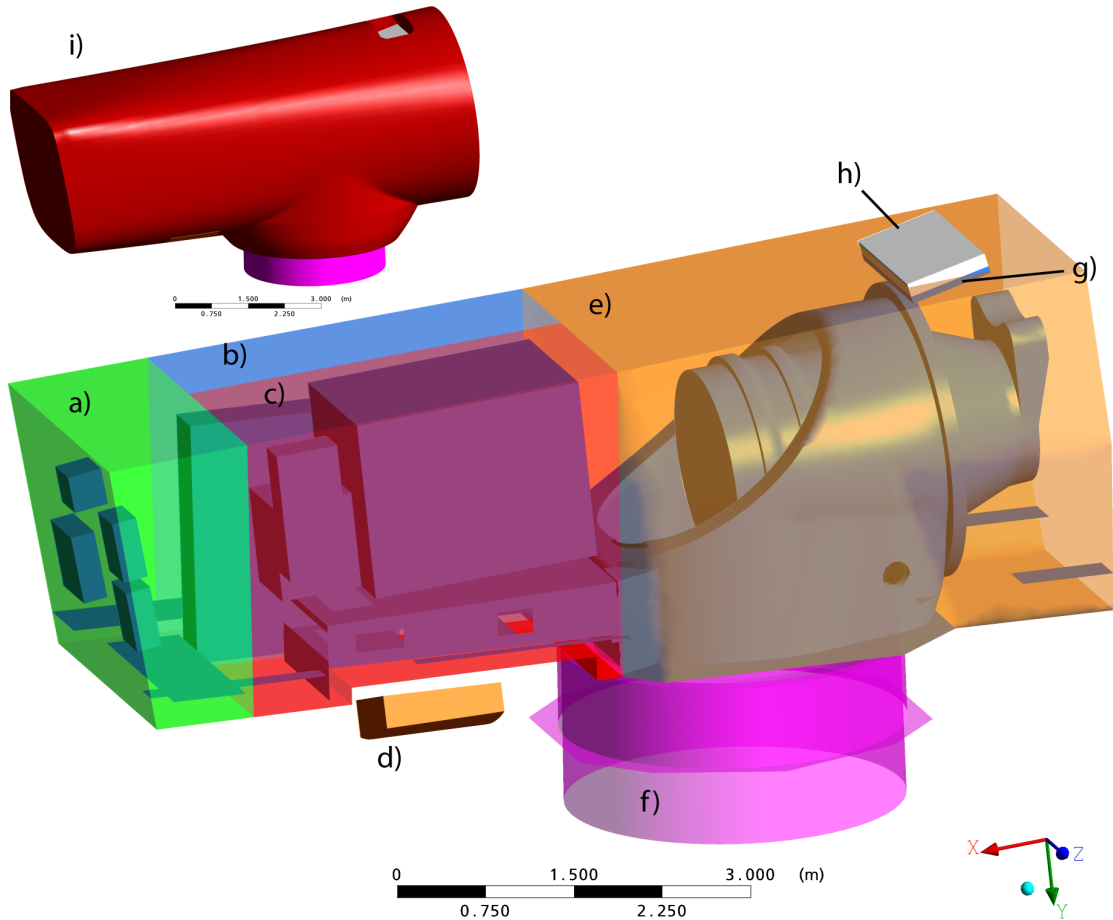**Figure 3.1:** Subdivision of the grid parts

a) *Hinten* (back)

b) *FU* (frequency converter cabinet)

c) *Generator*

d) *Inletgitter* (inlet)

e) *Vorne* (front)

f) *Turm* (tower)

g) *Kuehler* (oil chiller)

h) *Outlet*

i) *Huelle* (cover)

3.2 Differences Between Unstructured and Structured Meshes

Structured grids are constructed in a way "that grid points can be regarded as the points of intersection of curvilinear co-ordinate curves (in two dimensions) or surfaces (in three dimensions). [...] In two dimensions a grid point can be specified by a pair of integers (i, j), and neighboring points by (i + 1, j), etc.; the cartesian co-ordinates x(i,j), y(i,j) of a point can conveniently be stored as the elements of matrices" [10]. This means that the information about the neighbors of a particular grid point are stored in the position of the corresponding value in the matrix. In comparison to unstructured grids, where this information has to be stored in an additional data structure, this means a gain in performance for the solution algorithm and reduced memory consumption [5].

A disadvantage of structured grids is, that the refinement at certain geometry parts, say for example a boundary layer refinement at a wall, very often causes an unwanted refinement in regions where this is unnecessary. Figure 3.2 shows this kind of unwanted refinement in the free stream regime due to boundary layer refinement close to the wall. The figure displays a vertical, two-dimensional section through the domain where the converter box is situated. The fluid domain is colored in blue, whereas the magenta colored area is the cut through the solid domain of the converter box. Conjugate heat transfer takes place at the walls where the two domains meet. The walls must consequently be resolved very fine to allow the correct prediction of the flow and heat transfer characteristics in the boundary layer.

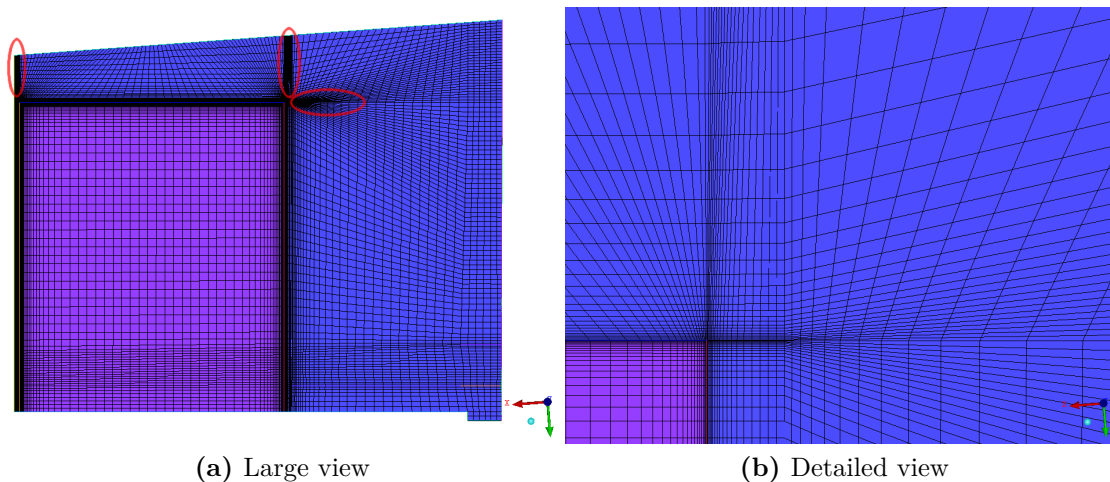(a) Large view   (b) Detailed view

Figure 3.2: Unnecessary grid refinement in structured grids

The refinement is visible as dark areas in 3.2a, because the black-colored grid lines are very narrow to each other. Figure 3.2b displays the upper right corner of the converter

box in detail in order to show the grid lines. The grid refinement, however, propagates into the free stream domain, as visible in the marked areas in figure 3.2a. The propagation of grid refinement occurs very often if structured grids are used in connection with very complex geometries, and as already mentioned, this is a waste of computational resources [6]. Such waste can be avoided by the use of unstructured grids.

Another disadvantage is the bad quality of the grid resulting from the increasing skewness and non-orthogonality of a structured grid when adopted to a complex geometry. Bad grid quality can provoke numerical errors and lower the efficiency of the numerical algorithm [16]. Here, the use of unstructured grids can help to improve the solution accuracy due to the higher flexibility of the node connections and an improved element quality. Especially boundary layer refinements can be realized very well as nodes can be placed anywhere in a volume with no limitation due to a certain grid structure.

As an example, figure 3.3 shows the two-dimensional grid for the simulation of the flow through a pipe bundle. The curved boundary lines represent the pipe walls, whereas the other (linear) boundaries are symmetry boundaries. The unstructured method displayed in 3.3a achieves a very orthogonal grid refinement at the curved walls with quadrilateral elements. The grid is refined only where needed. In the free stream regime there is a coarser grid of quite regular triangular elements.

The structured mesh in 3.3b is not refined at the walls. A refinement (split) of the elements close to the wall would influence all the elements colored in red and blue, although the blue elements are situated in the free stream regime, where a refinement is not wanted. In addition, the grid contains elements of bad quality (bad angle) in the corners and the elements in the free stream regime are quite irregular compared to the unstructured version.

During the grid generation process for the present study, the stringent node connections of structured grids slowed the grid generating process down compared to the unstructured parts. The amount of time consumed cannot be neglected as a disadvantage of structured grids. As a consequence, structured grids were used where possible and unstructured grids were used where it was not avoidable in the presented paper. The required combination of the two grid types leads to so-called *hybrid*-meshes or *hybrid*-grids. At the surfaces, where the different mesh types and grid parts meet each other, interfaces have to be defined to connect the parts. A detailed description of this process and of the types of interfaces can be found in chapter 4.1.

Additionally, Miles and Farrashkhalvat [10] mention that "unstructured grids have been found useful when employed in an 'adaptive' manner in the numerical solution of transient flows or moving boundary problems". Adaptive means that the grid is refined or coarsened during the solution run where needed. However, the CFD code Ansys CFX does not allow adaptive mesh refinement if multiple domains (grid parts) are used, so this option could not be used.
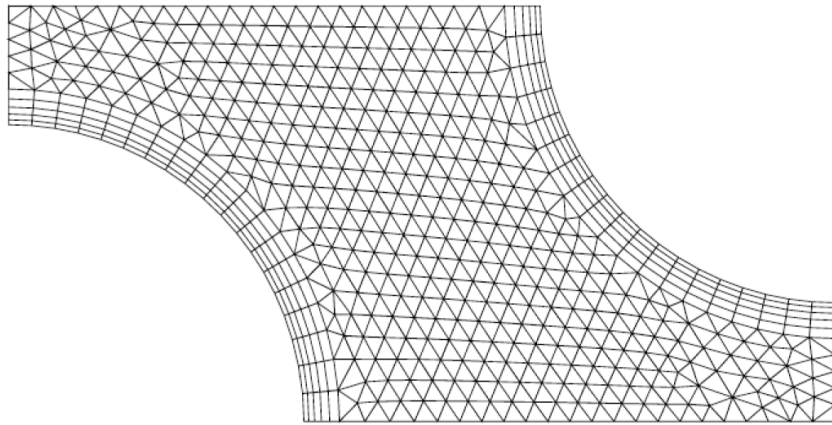
(a) Unstructured, refined grid at the example geometry
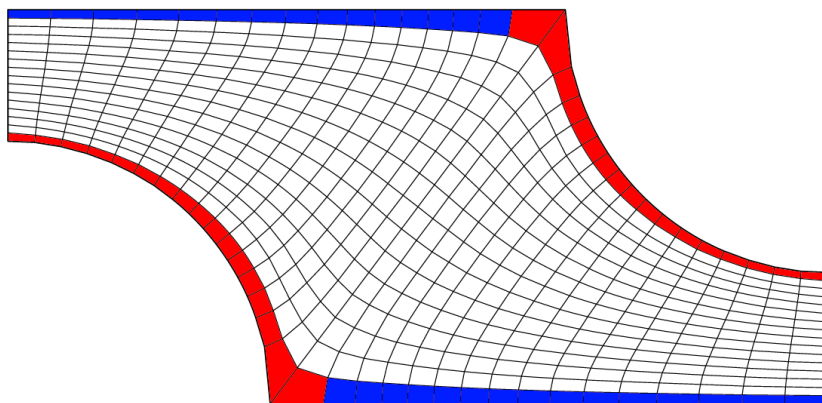
(b) Structured, unrefined grid at the example geometry

Figure 3.3: Comparison of unstructured and structured grids for a simple 2D geometry (figures taken from [6])

3.3 Example of a Structured Mesh

Figure 3.4 shows the example geometry of the grid part *Hinten*. The position in the global arrangement can be seen in figure 3.1. The geometry represents the back of the nacelle and contains four small cabinets as well as three floor elements. The surrounding surfaces represent the connecting interfaces to the neighboring grid parts. Each color represents the interface to one neighboring grid part, three in total. The connected grid parts are *FU*, *Generator* and *Huelle*, see also figure 3.1. The curves and surfaces shown are the result of importing the STEP file containing this grid part. The interface surfaces were generated in ICEM CFD, as explained in chapter 3.1.
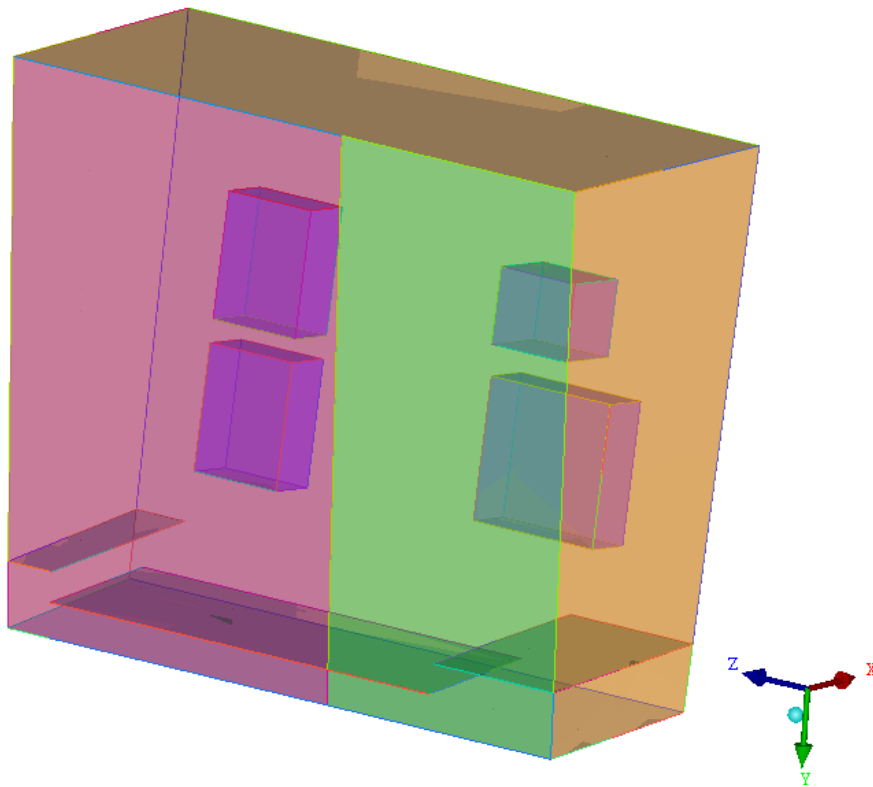
Figure 3.4: Overview of the example geometry

The first step in generating a structured mesh with ICEM CFD is, to initialize the first block. Thus, a default block is generated which is automatically fitted to the largest dimensions of the geometry. The default block is shown in figure 3.5. Compared to figure 3.6, one can see that the corners are not exactly positioned at the edges of the domain. The positioning is done with associations.

In order to adapt the block structure to the constraints of the geometry, this first block is split apart into a multi-block structure using the `Split Block` options. The result of this splitting is shown in figure 3.6. The default block was split to fit the visible floor elements and the hidden cabinets. The resulting block vertices, edges and faces are assigned to the corresponding geometry parts, i.e. points, curves and surfaces, using so-called `Blocking Associations`. The assigned blocking structure is moved to fit onto the corresponding geometry part. Mesh elements of an assigned face will for example be projected onto the corresponding surface. The result is a clean surface mesh which is placed exactly on the chosen surface. The whole process of adapting the block structure to the geometry takes its time for complex geometries, but is necessary to receive a good mesh. For unstructured meshes, this step does not exist.

In order to create the first mesh, it is necessary to define the global element seed size in the `Global Mesh Parameters` under the `Mesh` tab. Assigning the mesh parameters to the pre-mesh is done by selecting the `Blocking>Pre Mesh Params` tab and applying the `Recalculate Sizes` function to the block structure. ICEM CFD prints the results, i.e. the number of elements, to the log window. Now, it is possible to have a look at the first mesh by (re)calculating the `Pre-Mesh`. As the associations of the block structure to the geometry are already set, the result is a quite smooth mesh which is properly fit to the points, curves and faces of the geometry.
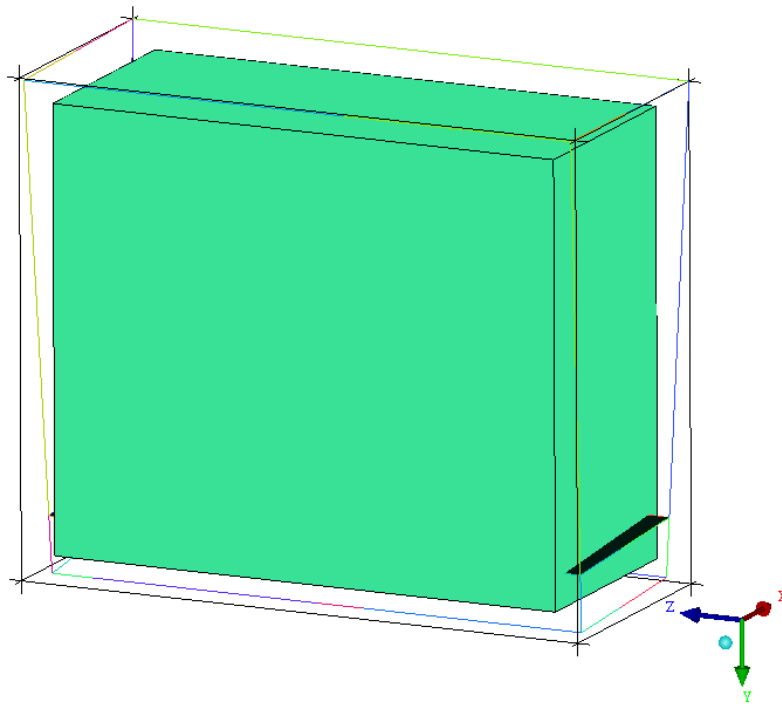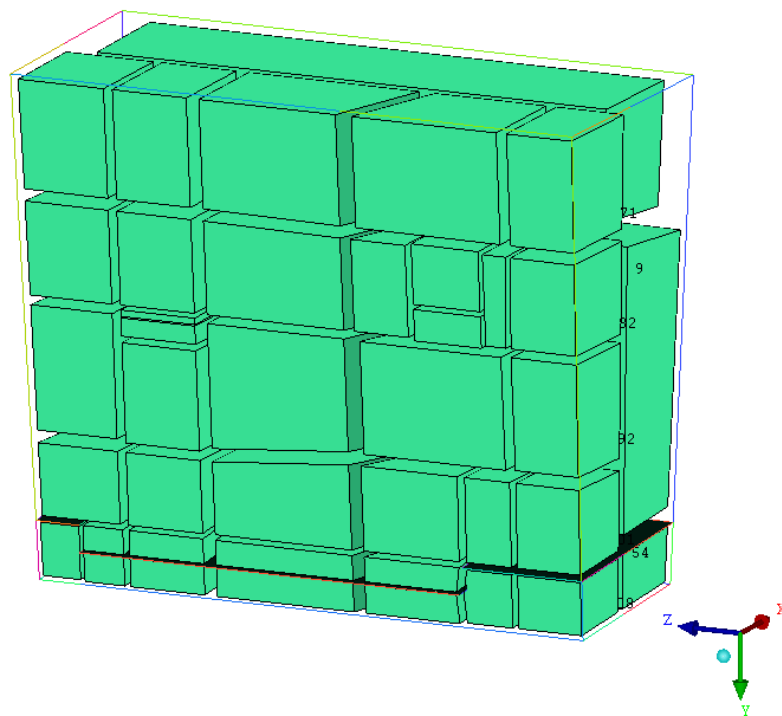
Figure 3.5: The default block

Figure 3.6: The multi-block structure after splitting and assigning associations

3.4 Mesh Refinement

The next step is the refinement of the mesh at surfaces using the `Part Mesh Setup` under the `Mesh` tab. Mesh constraints for each part in the parts tree can be defined here. A boundary layer refinement at a wall is defined by setting the height for the first element next to the wall and the growth factor for the following elements. A maximum number of layers and the maximum size in surface direction can as well be defined.

Mesh refinement or coarsening can be defined by using ICEM CFD's `Surface Mesh Setup`, `Curve Mesh Setup`, `Mesh Density` and `Mesh Curve` function. These options are of interest, if you want to modify one single element or a group of elements at a time which were not combined to a part in the parts tree beforehand.

3.5 Defining Thin Surfaces

The floor elements displayed in this example represent three-dimensional plates of steel. It was acceptable to reduce the floor elements by one dimension to a thin surface which prevents mass and energy from passing through it, neglecting its thickness. The model consequently represents the floor elements as one surface only, confined by curves and points. Important for thin surfaces is the checkbox `Int Wall` in the `Part Mesh Setup`. Checking this box makes the affected surfaces accessible as 2D-mesh regions in Ansys Pre, which is necessary to define the wall boundary condition.

3.6 Mesh Quality Improvement

After a satisfying mesh definition has been achieved, the pre-mesh has to be updated. Right-clicking the `Pre-Mesh` button with the mouse and choosing `Convert to Unstruct Mesh` converts the pre-mesh into a mesh which can be exported as a mesh file readable for Ansys Pre. Before using the export function, the mesh quality should be examined by using the `Display Mesh Quality` function in the `Edit Mesh` tab. A multitude of quality criteria can be chosen to evaluate the quality of the mesh. For meshes with cuboid elements the worst element angle and the aspect ratio are important. As a guide, the angle should be bigger than 20° and the aspect ratio should be below 100 to limit numerical errors during the solution run. The quality criteria depend on the solver and on other influences. If the quality does not match these criteria, the mesh can be smoothened using the function `Smooth Elements Globally`. The criterion to be improved can be selected. It may help to add or remove constraints for the blocking structure by changing the geometry associations if the smoothing does not lead to satisfying results. Especially the repositioning of single vertices and the association of edges to curves can improve the

mesh quality. Mesh quality can already be estimated before converting the pre-mesh by plotting `Pre-Mesh Quality Histograms` in the `Blocking` tab. A `Pre-Mesh Smoothing` option is also available in this menu.

Common problems are inverted or negative volume elements. In many cases, these problems are related to the blocking procedure itself, for example when all elements of one block are inverted. Such problems can be solved by running the `Block Checks` named `Run Check/Fix` and `Fix Inverted Blocks` on the blocking structure. It is recommended to run these functions at least once before the pre-mesh is converted to a so-called *unstruct mesh*.

If only a small number of negative or bad elements occurs, this fact is often related to a block structure which is not well adapted to the geometry. The adaption of the block structure can be improved by applying additional block splits, edge associations or by moving vertices.

After the improvements result in an acceptable mesh quality, the procedure is completed by the mesh output.

3.7 Mesh Output

Under `Solver Setup` in the `Output` tab, the right solver has to be chosen to write a mesh file which is readable in Ansys Pre. In this case, the option *ANSYS Cfx* was chosen as the output solver and *ANSYS* as the common structural solver.

Clicking on the `Write Input` button in the `Output` tab opens a window which lets you choose additional options and a file name for the output file. The options were left at the default values and, finally, a grid-file called *filename.cfx5* was written.

4 Defining the Simulation in Ansys Pre

After generating the different grid parts, they were reassembled in Ansys Pre. Each part of the grid was imported to Ansys Pre as a particular domain. The domains had to be reconnected by the use of *domain interfaces*. In this case, interfaces of the types *fluid-fluid*, *fluid-solid*, *solid-solid* and *fluid-porous* were used, each of them connecting two domains of the given types. For general connections, two types of connection methods are available. More options are available for moving connections for fluid machinery for example.

4.1 Interface Connection Methods

4.1.1 Method 1:1

This connection method is very restrictive as it tries to connect each of the nodes on one side of the mesh with a node on the other side of the mesh which corresponds exactly in location. It allows only a very small amount of spatial tolerance of the pairs of nodes, which leads to a high effort in grid generation. Direct connections were only possible where an interface between a fluid domain and a solid domain inside one grid part was present, for example the fluid-solid-interface between the generator and the surrounding air volume The precise spatial consistency of the nodes makes it possible to pass a variable from one node to the corresponding node during the solution without interpolation. Hereby computing time is saved and numerical errors due to interpolation are avoided. [1]

4.1.2 GGI Method

The GGI (*general grid interface*) method on the other hand allows the combination of arbitrary surface meshes between two grid parts. Consequently, it is no longer necessary to match nodes on both sides and the grid generation process becomes a lot faster and less challenging. In order to pass variables from one side to the other, an interpolation between the nodes on each of the two surface meshes takes place. The interpolation step costs additional computing time and gives rise to numerical errors. The latter may lead to difficulties in convergence during the solution. The interpolation step itself may cause changes of variables like a sudden temperature or pressure change at the interface due to

these numerical errors. Therefore, the variation of variables at the interfaces should be checked in Ansys Post [1].

Figure 4.1 shows, how an interface is defined in Ansys Pre. In the dialog on the left the two interface sides were chosen. In this case, the *fluid-fluid* interface between the unstructured fluid domain *F Vorne* and the structured fluid domain *F Huelle* was defined. *General Connection* was selected in the interface models section as the two domains do not move in relation to each other. The *GGI* connection method is the right choice in this case, as an unstructured and a structured domain are connected and no congruence is given between the nodes on both sides. Alternatively, the option *Automatic* could have been chosen. If so, the solver checks, whether a *1:1* connection is possible and if not, it automatically switches to the *GGI* connection. The two meshes that are being connected are shown in the viewer. They are highlighted in green. It is readily identifiable that there is no congruence between the meshes or nodes on both sides.
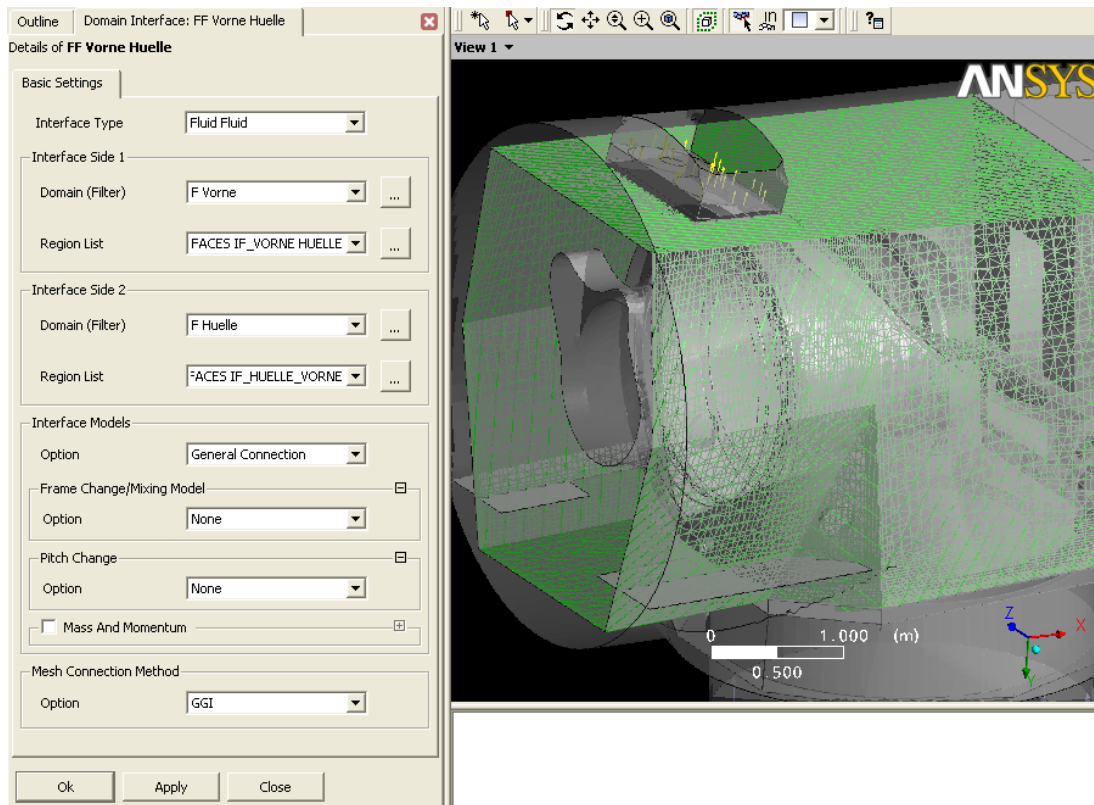

Figure 4.1: Definition of interfaces in Ansys Pre

4.1.3 Comparison

Both interface types have important advantages. However, during the grid generation process, it became clear that only the GGI interface is reasonable for most of the interfaces. Only some fluid-solid interfaces (at the walls of the generator, gearbox and parts of the converter box) could be realized using direct connections, as the solids were meshed with the corresponding surrounding air (the corresponding second surface mesh) at the same time.

The influence of the choice of the mesh connection method on the results and the convergence behavior was not examined in this study.

4.2 Conjugate Heat Transfer

The heat transfer between solid and fluid domains was modeled using *conjugate heat transfer*. This means, that both the solid and the fluid volume are *filled* with a mesh. The two meshes are connected with a 1:1 interface, cf. chapter 4.1.1. The heat flux at this interface is calculated during the solution. The heat flux and the temperature distribution in the solid domain and the flow characteristics, temperatures etc. in the surrounding fluid domain are calculated in parallel. There is no separate solution run for the solid domain. More detailed explanation is to be found in [1].

In order to obtain valid result for the wall temperatures and the heat transfer coefficient, a high resolution of the boundary layer is necessary. See more on this in chapter 6.5 - *Analyzing Control Box Surface Temperatures*.

4.3 Choice of Turbulence Model

At this point, it shall only be briefly mentioned that after detailed investigation of three turbulence models by practical appliance and literature research, it was decided to use the SST *(Shear Stress Transport)* model for the calculation of the final results. For more information on the reasoning for this choice and on the SST-model proceed to chapter 5, where the three turbulence models are tested and compared.

4.4 Porous Domain Model for Gearbox Oil Chiller

The only air outlet of the wind turbine nacelle is situated at the top of the nacelle. A set of two blowers is used to suck the air over two parallel oil-to-air heat exchangers for the gearbox and to release the air into the ambience. In order to keep the global model

and grid for the nacelle as simple as possible, this set of blowers and heat exchangers was separately modeled and numerically calculated. The results were used to develop a simplified model which was then implemented into the global model of the nacelle.

The challenge was to determine the pressure loss of the blowers and heat exchangers at the outlet, as no measured value was available at the beginning of the work for this paper. After all, a characteristic curve became available close to the end of this study, allowing for a comparison of the calculated pressure loss with measurements. It became obvious, that the measured pressure loss was about factor 70 higher than the calculated one. Certainly, the density change of air due to heat release was not taken into account in the characteristic curve. Nevertheless, an error of that dimension cannot be explained only with the density change. The geometric model of the detailed model, cf. figure 4.3a, is suspected of being the origin of the error. In the end, the cubic resistance coefficient in equation 4.3 had to be corrected so that a closer congruence to the measured data was realized for the calculation of the final results for chapter 8 and 9. Although the results of this procedure were not very satisfactory, the procedure shall be presented in this chapter to give an impression of what had been done, and probably the attentive reader can find the error.

The pressure loss coefficient ζ was used to model the heat exchanger by a porous media with a certain pressure loss instead of resolving the detailed geometry in the global grid.
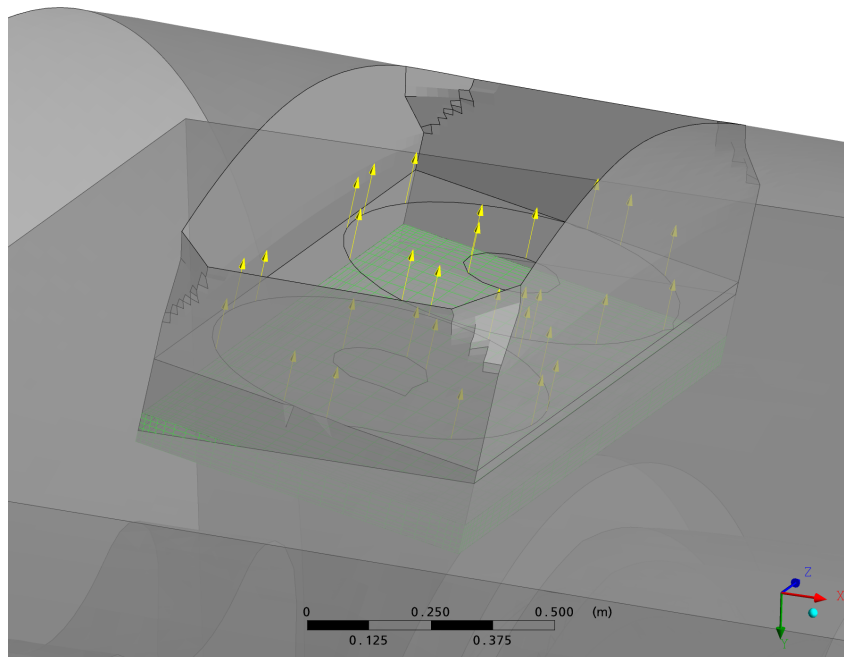

Figure 4.2: Oil-to-air heat exchanger in front of the outlet of the nacelle

The blowers are situated outside the calculation area. Hence, they were modeled through an appropriate boundary condition at the outlet, i.e. the outlet speed and its direction at the opening were defined. Figure 4.2 depicts the upper part of the nacelle with the model for the heat exchangers and the blowers. The boundary condition at the blowers is illustrated by yellow arrows, indicating the fixed direction of the flow. The heat exchanger is highlighted in green. It represents a porous domain for which a pressure loss was defined. The influence of the rotation of the blowers was neglected, which is perfectly legitimate. The air passes through the mentioned finned oil-to-air heat exchanger right before entering the blowers. The finned oil chiller filters the rotational velocity components to a good part.

4.4.1 Calculating the Pressure Loss Coefficient

The determination of the pressure loss coefficient ζ was done by resolving the geometry of the two blowers and heat exchangers in detail with a mesh of 79,324 nodes using two symmetry planes. This model is shown in figure 4.3a. The cooling fins are visible as well as the contraction of the cross section. The model is divided into three domains. The lower domain at the inlet, followed by the domain resolving the cooling fins, where the heat is released and the topmost domain representing the outlet. The latter was meshed using tetraeders and prisms (unstructured), whereas the others were meshed with structured grids. The symmetries are in x- and -z-direction where no blue walls are drawn, so that in x-direction the second half of the first blower and in -z-direction the second blower set is replaced with symmetry boundaries. The simplified model is shown in figure 4.3b. The middle domain is replaced with a much simpler mesh, not resolving the fins. The heat release again takes place in this red part. The mesh size has been reduced drastically for the simplified model and the same symmetry boundaries were used.
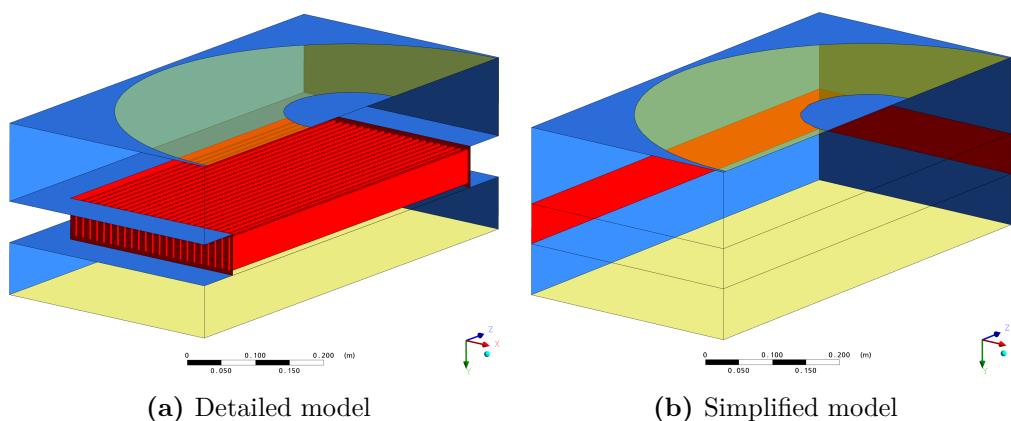

(a) Detailed model (b) Simplified model

Figure 4.3: Models for the oil-to-air heat exchanger and the blowers

The pressure loss of a flow resistance in general is defined as

$$dp_{tot} = \zeta(\frac{\rho}{2})v^2 \tag{4.1}$$

Reorganizing this formula for ζ gives

$$\zeta = 2\frac{dp_{tot}}{\rho}v^2 \tag{4.2}$$

ζ was determined by evaluating the loss of total pressure between inlet and outlet of the heat exchanger domain. The density and the velocity are evaluated at the same point before the heat exchanger.

While ζ can be regarded as constant for simple flow resistances, there is a significant dependency of ζ on the flow velocity when it comes to more complex flow resistances. In the case of a finned oil-to-air heat exchanger the geometry is very complex and ζ is subject to change of flow velocity.

With the above described process, a correlation between ζ and the flow velocity could be found. Another influence on the loss coefficient however is the heat source which results in density changes during the passage through the heat exchanger. As only one operating point was known with both the outlet velocity and the corresponding released heat quantity, it was possible to calculate only one ζ-value including heat release influences. This point was the operating point, i.e. the point of interest. Again, the detailed model was used to find ζ. The only change was the implementation of a subdomain with a total heat source of 17750 W, which corresponds to the heat released at the operating point in one quarter of the geometry. The resulting pressure loss coefficient was found to be slightly higher than without the heat source.

4.4.2 Simple Model for the Complex Heat Exchanger

After the pressure loss coefficient was found for the case including the heat source, the next step was to implement the coefficient to the simple model with the porous media domain, cf. figure 4.3b. The simple model was then used as a part of the global grid of the nacelle.

The quadratic coefficient used in Ansys CFX to define a pressure loss through a porous domain is of the form

$$C_{cubic} = \frac{\rho}{2} K_{loss} = \frac{\rho}{2} \zeta \qquad (4.3)$$

An *expression* was defined in Ansys Pre for C_{cubic}, which uses the calculated ζ value and the actual density. The expression was entered as the quadratic coefficient in Ansys Pre, so that the loss coefficient would be dynamically calculated depending on the actual density of the air flowing through the chiller. Apart form the quadratic loss coefficient, there is am optional linear coefficient. More important is the choice whether *superficial* or *true* velocity is used to *determine* the loss coefficient. True velocity has to be chosen if the loss coefficient was calculated using the actual flow speed in the detailed heat exchanger, as it was done in the case presented. The superficial velocity is to be used in the case that ζ was calculated with the flow speed without taking the contraction of the cross section into account - this would result in lower speeds. [1]

"The volume porosity γ at a point is the ratio of the volume V' available to flow in an infinitesimal control cell surrounding the point, and the physical volume V of the cell" [1].

$$V' = \gamma V \qquad (4.4)$$

The volume porosity is a required input field in the porosity settings tab in Ansys Pre and can be easily calculated due to the geometric relations of the simplified and the detailed model. This factor takes the differences of the flow speed between the simplified model and the detailed model into account.

A directional loss can be defined in Ansys CFX by choosing this option in the *Porosity Settings* tab and defining a multiplier for the resistance coefficient transversal to the specified main flow direction. In this case, a multiplier of 100 was chosen for this transversal loss, as flow in transversal direction to the main direction is inhibited by the cooling fins.

In the simplified model the heat exchanger was implemented as a domain of porous media with a heat source. The simplified model of the blower and heat exchanger set consists of 18,997 nodes compared to 79,324 nodes in the detailed model, both numbers representing one quarter of the actual geometry, taking advantage of two symmetry planes.

The validity of the simplified model was tested by calculating the same operating point as on the detailed model and comparing the results. The volume porosity γ of the porous media domain had to be adjusted until the results were of close congruence with the

detailed model. Optionally, a correction factor could have been implemented to more transparently apply this adjustment.

For the global model of the nacelle, a similarly simple model was implemented. It consists of about 25,000 elements, as it was not possible to take advantage of symmetries. The same settings were made in the porosity settings tab and very similar results were achieved for the pressure loss in the global model.

4.4.3 Problems During the Procedure

The main problem of the procedure is to determine the pressure loss coefficient of the blower set. After it is found, it has to be transformed into the resistance coefficient which is used in Ansys CFX. The coefficients used in Ansys CFX are of a slightly different form but transformation is simple. Although the calculated values for ζ and the volume porosity γ were used, a further correction of γ had to be made in order to achieve the same pressure loss with the simplified model as with the detailed model. Beyond this rather small correction, the already mentioned factor 70 had to be applied to adjust the numerically calculated pressure loss to the measured one, which was taken from the characteristic curve of the heat exchanger and blower set. The now achieved pressure loss after correction is very close to the measurements. The provenance of this disparity could however, not yet be identified. The error is suspected to be found in the geometry of the detailed model.

4.5 Partitioning for Parallel Computing

Ansys CFX uses the *MeTis* method as the standard method for partitioning when using parallel computing. Performance issues have come up during the solution run as a result of the multi domain treatment of the partitioner. As default, the partitioner uses the *independent partitioning* approach which divides each domain into the number of partitions specified in the solver manager, i.e. the number of CPUs. In connection with a big number of domains, this results in a high number of overlapping elements. Overlapping elements are part of more than one partition. They are processed by more than one CPU and the results are used to hand over the flow parameters from one partition to the neighboring. Therefore, overlapping areas cannot be totally avoided in parallel computing. In order to reduce the necessary CPU time for the global solution, it is possible to optimize the number of overlapping elements, which can be done by choosing the optimal partitioning method. For multiple domains, the multi domain option should consequently be set to *coupled partitioning*. The partitioner now ignores domain interfaces and splits the global mesh into a chosen number of parts. This results in a reduced number of overlapping elements, and consequently in reduced computing time. [1]

5 Turbulence Models

"For complex industrial configurations (aircrafts, turboengines, helicopters, ...) the main objective, up to now, remains to prescribe accurately the influence of the turbulence on the mean flow quantities rather than to predict with lot of details the turbulent quantities. In that case it is necessary to evaluate and to select models well-adapted to complex configurations and topologies, ..." [5].

In order to justify the choice of a particular turbulence model for the computation of the solution which will be used for chapter 8 and 9, a comparison of several turbulence models was conducted. In the literature, turbulence models are often compared at an academic level by the use of simple test cases. For these test cases either experimental data, direct numerical simulation *(DNS)* results or both are usually used for validation, as recommended by Hölling [7]. As none of these was available or possible for this paper and as the geometric model was much too complex, such a study was not possible. Moreover, this not the interest of the present paper. However, a general comparison of turbulence models among each other was conducted to investigate whether serious discrepancies in the main flow characteristics arise, see chapter 5.5. Global values of technical interest (mass flow and temperatures at the sample planes in the flow field) were used to evaluate the numerical results, as proposed by Hölling [7]. These main flow characteristics, however, turned out to be quite insensitive to the turbulence model applied. A literature study was conducted beforehand to identify the most promising turbulence models and to get an impression on their general strengths and weaknesses.

5.1 Overview of Examined Turbulence Models

Out of the vast number of available turbulence models, three very commonly used models have been selected and tested for their ability to predict flow and temperature characteristics in this appliance. The three models are the k-ε model, the SST *(Shear Stress Transport)* model and the SSG Reynolds Stress model. They are all available by default in Ansys CFX.

5.2 K-ε Model

According to Cebeci "the k-ε model is the most popular and widely used two-equation eddy viscosity model" [4]. This model can be considered the industry standard for general purpose industrial CFD applications. It offers a good compromise in terms of accuracy and robustness. In Ansys CFX it makes use of scalable wall functions, which allow solutions on arbitrarily fine grids. However, this model may not be suitable for flows with boundary layer separation and flow over curved. [1]

Although this model may not be optimal due to the doubtless occurrence of boundary layer separation and curved surfaces in the air flow situation inside the nacelle, this model was investigated as it can be regarded as industry standard. According to the Ansys CFX documentation, the scalable wall function approach for the modeling of the flow near the wall makes it insensitive for grid resolution near the wall. [1]

5.3 SST Model

5.3.1 Prediction of Flow Separation

Flow separation is a very important phenomenon of flow dynamics. However, the k-ε model tends to predict the onset of flow separation too late which leads to a too optimistic lift for airfoils, for example. The result is a non-conservative prediction of important values. Such a behavior is shown by any turbulence model using the ε-equation. But, also for appliances with heat transfer calculations there is a great influence, as the heat transfer coefficient is strongly dependent on the local flow field. Therefore, flow separation has a big influence on the amount of heat being transferred. However, many turbulence models fail to predict the flow separation. In order to solve this problem, a number of turbulence models have been developed. The most prominent two-equation model amongst them certainly is the SST-model. [1; 4]

The SST-model is a two-equation model similar to the k-ε model. Its main feature is zonal modeling, as it switches to Wilcox's k-ω model near the wall using blending functions. Menter [9] points out its main virtues: "The SST model combines the advantages of the k-ε and the k-ω model to achieve an optimal model formulation for a wide range of applications. [...] It activates the k-ω model in the near wall region and the k-ε model for the rest of the flow. By this approach the attractive near-wall performance of the k-ω model can be used without the potential errors resulting from the free stream sensitivity of that model."

This modification "improves the prediction of flows with strong adverse pressure gradients and separation" as Tuncer and Cebeci acertain [4]. Beyond that it uses a modified definition

for the eddy viscosity in order "to accurately capture the onset of separation under pressure gradients" [9]. These improvements lead to a supreme performance of the SST-model in cases with flow separation.

The SST-model is k-ω based near the wall, but through a blending function the formulation becomes equal to the k-ε equations in the free stream far from the wall. The improved accuracy of this model in flow separation and heat transfer prediction have been stated in many studies [17; 9; 2].

5.3.2 Automatic Wall Treatment

In industrial appliances it is often difficult to ensure the adequate wall resolution which is necessary for a certain turbulence model. Many two-equation turbulence models are very sensitive to wall resolution. In the past, there have been two main approaches for treating the wall boundary layer in a turbulence model.

- The low-Re approach integrates the boundary layer through the thin viscous sublayer. Generally, this approach is preferred as it treats the physical effects better than the later discussed wall functions method. However, the main disadvantage of a strict low-Re model lies in its need for a very fine grid resolution close to the wall, which augments the effort needed for grid generation as well as later computing time. In complex geometries, which are common in industrial appliances, this restriction is essential as it would lead to poor mesh aspect ratios close to walls. Poor mesh quality gives rise to numerical errors.

- As an alternative, wall functions were developed in order to bridge the viscosity affected region with empirical formulations. They presume that the first node lies in the fully turbulent region of the boundary layer and empirical functions connect the wall conditions with the near-wall mesh variables. Consequently, the physics in the boundary layer are not properly resolved, but modeled. This is acceptable in cases where the effects in the boundary layer are not the main interest. In terms of grid generation a fixed distance is required between the wall and the first node next to it, i.e. a fixed $y+$ value. Too low values of $y+$ lead to poorer results, as demonstrated in [9]. Mesh generation became easier with the introduction of scalable wall functions, allowing an adaption of the wall function depending on the local $y+$.

The SST-model introduces blending functions to locally switch from low-Re approach towards wall functions, depending on the local grid dimensions. Consequently, it takes advantage of the robustness of the wall functions in coarse areas while resolving the physics down to the viscous sublayer using the low-Re approach in finer meshed regions. Primarily, however, it gives flexibility during grid generation. The blending function mentioned is amongst others depending on the local $y+$ value, which is the dimensionless wall distance

of the first node. It describes the height of the first node at a wall and by that the mesh refinement. At the beginning of a simulation using the SST-model, the wall scale equation is solved. This equation calculates the distance to the wall for each node, which is required to solve the blending function. [1]

5.3.3 Influence of $y+$ for the Turbulence Models

The appropriate amount of boundary layer refinement is heavily discussed and tested in the literature. For the adequate resolution of the temperature boundary layer, of $y+ \simeq 1$ is very often applied, for example in [9]. The SST-model uses a low-Re formulation for $y+ < 2$ and scalable wall functions if $y+ > 11$. In between, it uses a blending of the two [1]. The SST-model as well as the k-ε model use scalable wall functions if $y+ > 11$. Consequently, it seems important to investigate whether the heat transfer is predicted differently when the low-Re formulation is used. The influence of $y+$ on the wall temperature and the temperature profiles using the SST-model are discussed in detail in chapter 6.5.

5.4 SSG Reynolds Stress Model

This model has been selected to investigate whether second moment closure brings significant changes in the results. For certain, the higher order of this model causes an increased consumption of computing time.

The Ansys CFX documentation recommends the use of Reynolds Stress models for strongly buoyant flows, which is the case in the presented geometry. In particular, the SSG Reynolds Stress model is suggested among the number of Reynolds Stress models available in Ansys CFX. [1]

5.5 Numerical Results for Various Turbulence Models

The three selected turbulence models were compared by applying them to the same meshes with identical boundary conditions and solver settings. The mesh sizes used are represented in the tables 6.2a for the coarser mesh and table 6.2b for the finer one. In chapter 6.1 a detailed description of the meshes used is also given. The boundary conditions are represented in table 6.3 whereas the common solver settings are depicted in table 5.1.

In order to compare the results for the three turbulence models and two mesh sizes in Ansys Post, a session file has been written which generates ten planes of one square meter each. The position of the sample planes is shown in figure 5.1. For each of these sample planes the integral mass flow of air and the average air temperature were evaluated. This

Table 5.1: Solver settings for the turbulence model comparison

Solver settings	
Advection scheme	high resolution
Convergence criteria	RMS
Residual target	10^{-4}
Solver precision	double
Solid time-step control	automatic
Fluid time-step control	varied
Heat transfer	total energy
Solid	steel
Fluids	air, ideal gas
Turbulence model	varied
Buoyancy turbulence	none
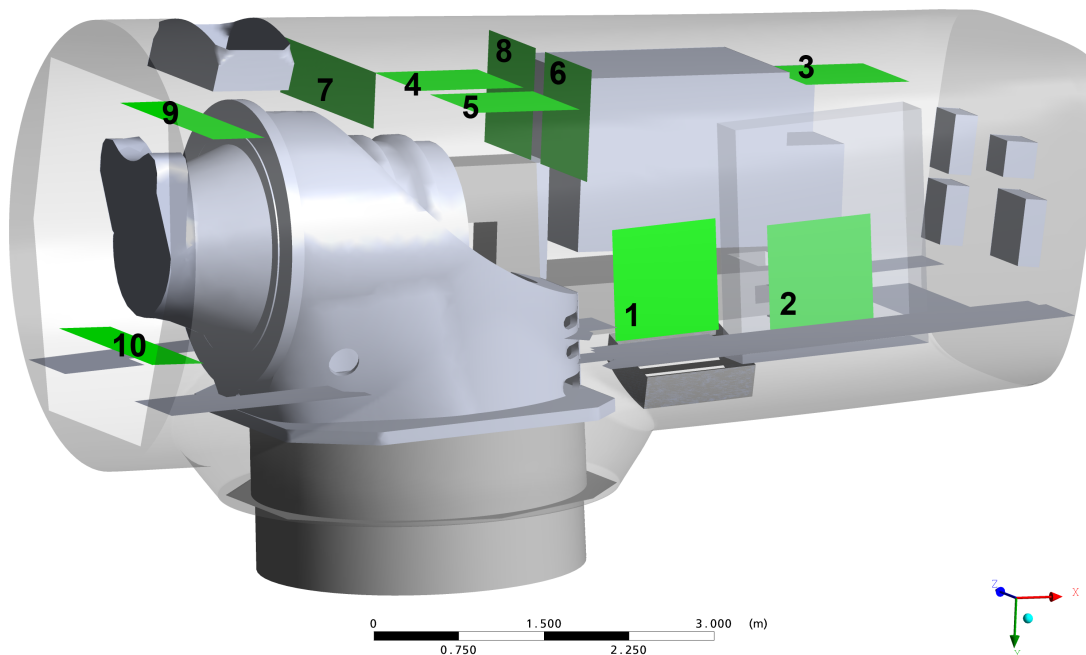
Figure 5.1: The sample planes in Ansys Post.

procedure was developed in order to keep up with Hölling's claim for a comparison on the level of global values of technical interest [7].

At a qualitative level, the results for the turbulence models do not vary much, as can be seen in the following plots. Big differences in the results have to be expected if you go more into details. A comparison with measurements or DNS results cannot be made. So, this turbulence model comparison has to be understood as a test whether crucial discrepancies even in the qualitative results have to be expected. Of course, this study can in no way be compared with studies from simple and analytically or experimentally validated test cases which are often used in the literature.

Figure 5.2 shows the mass flows for each of the ten sample planes. The sign represents the direction of the flow. It is visible that the mass flows are very similar for the three turbulence models at nearly all of the sample planes. The size of the grid has no big influence for most sample planes. For some of the sample planes the direction of the mass flow changes if you compare the turbulence models and the mesh sizes between figures 5.2a and 5.3a. However, the absolute differences are small. The most important differences are visible at the sample planes nine and ten.

The absolute difference between the values at one sample plane, however, are acceptable if you keep in mind that the intention of the whole study is to give qualitative results for the flow in the nacelle.

Figure 5.3 demonstrates that the averaged static temperatures for each of the ten sample planes do not vary much if you compare the turbulence models and the mesh sizes between figures 5.2b and 5.3b. At the level of qualitative information, the different turbulence model results coincide quite good.

There was no notable difference in computing time between the SST and the k-ε models. The SSG Reynolds Stress model, in contrary, took considerably longer during solution runs and showed a lack of stability. A solution run could only be successfully started if a preliminarily calculated result file from a simpler turbulence model was used as an initial guess file.

It can be concluded from this study that the choice of the turbulence model does not essentially influence the expected results, keeping in mind the desired grade of detail. A preference for one particular turbulence model cannot be reasoned out of the presented results. Thus, literature recommendations were favored for the selection of a turbulence model for the further studies effected, see chapter 5.6 and 5.7.
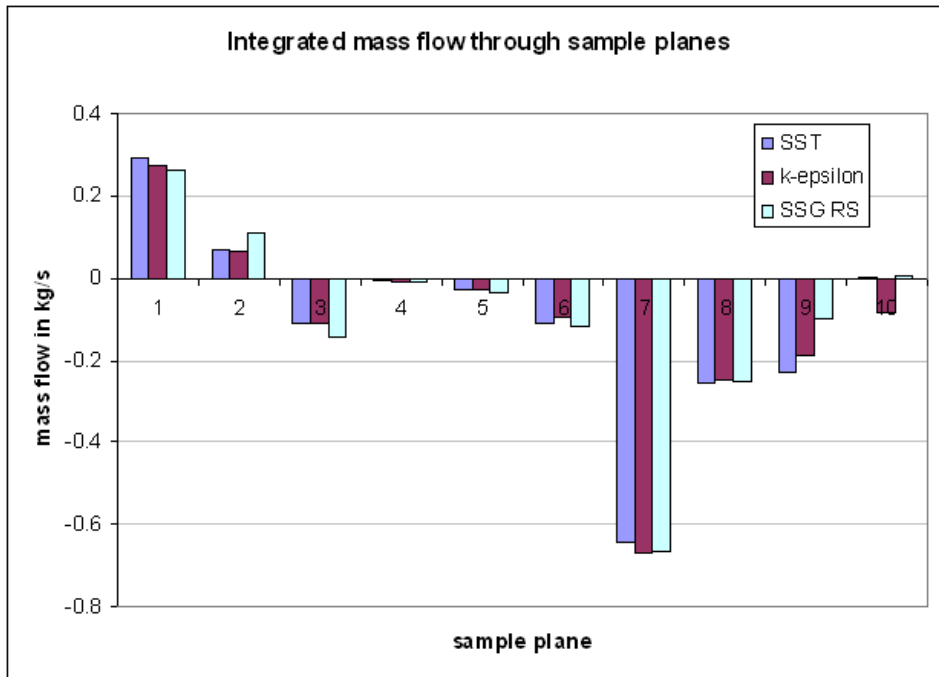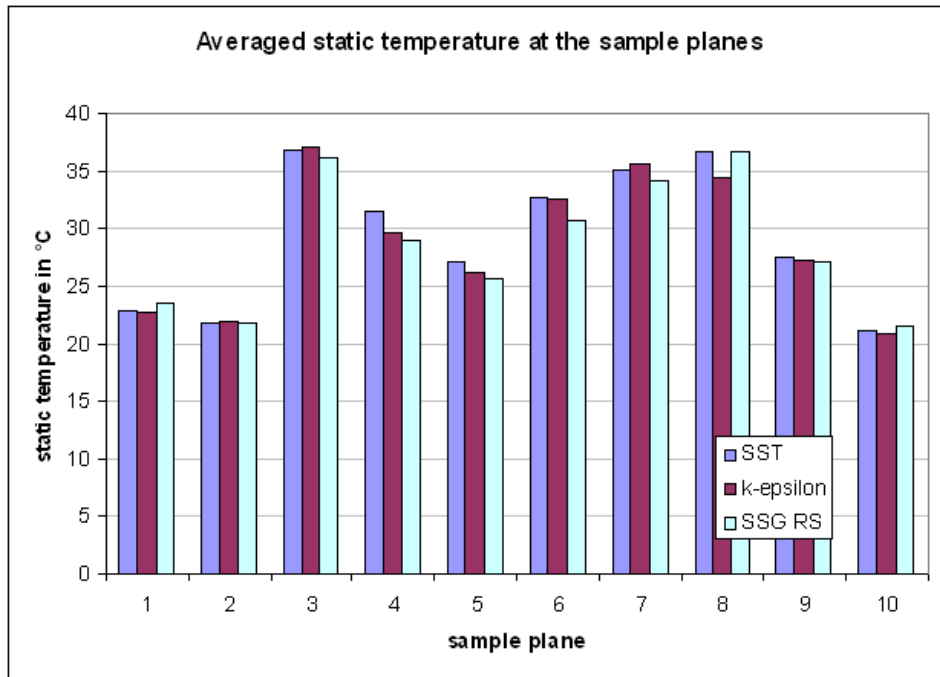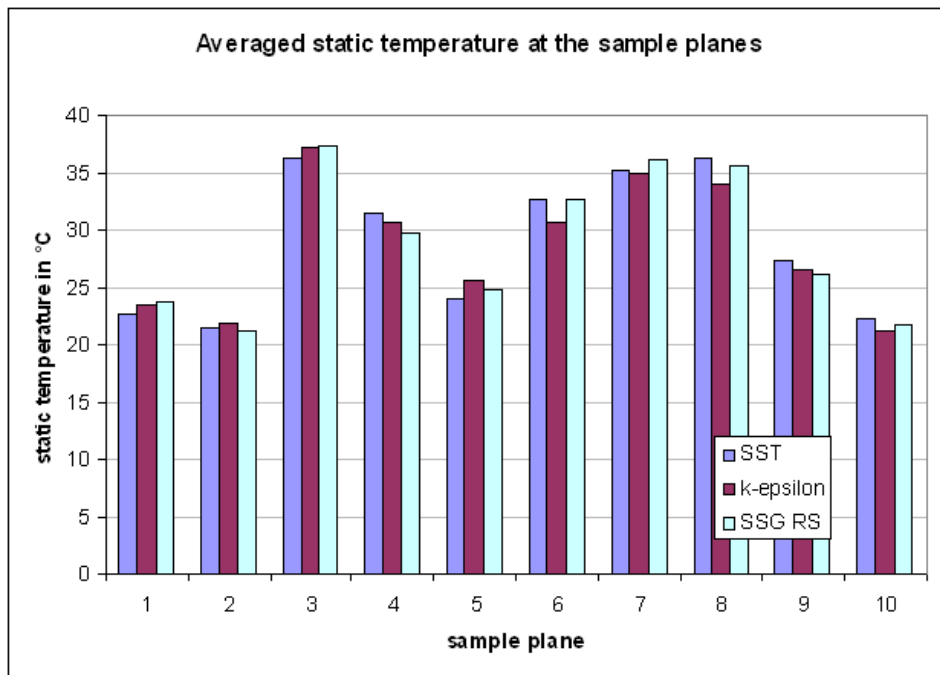
(a) Coarse grid
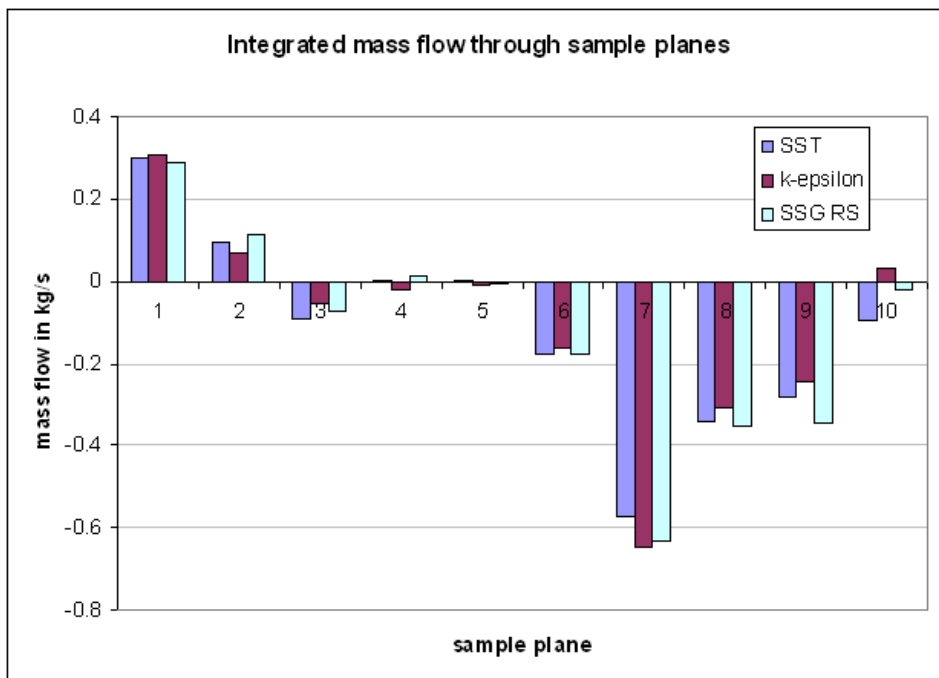
(b) Normal grid

Figure 5.2: Integrated mass flow results at sample planes for the turbulence models

(a) Coarse grid

(b) Normal grid

Figure 5.3: Averaged static temperature results at sample planes for the turbulence models

5.6 Literature Results for the Investigated Models

Several scientific investigations have already been made in other research papers for the comparison of turbulence models with test cases including heat transfer, for example in [9] and [15]. The results pointed out that the SST *(Shear Stress Transport)* model gives the best results for both heat transfer and air flow characteristics. In connection with conjugate heat transfer, the SST-model was considered as the most promising and therefore was focused on. Especially for heat transfer the SST-model gives the best results, provided that the boundary layer is sufficiently resolved by the grid.

Menter et al. [9] point out that scalable wall functions and automatic wall treatment (cf. chapter 5.3.2) "lead to a significant reduction in the sensitivity of heat transfer predictions to the near wall resolution". In this point, the k-ε and the SST-model are similar as both of them use scalable wall functions. Differences arise when continuing to decrease the $y+$ value which causes the SST-model to switch to its low-Re wall treatment, especially in cases with low Reynolds numbers (low turbulence). In these cases, a fine grid resolution and the use of a low-Re wall treatment is essential. Hence the SST-model shows better accuracy than the k-ε model with scalable wall functions. [17]

Vieser has conducted a detailed investigation with a series of test cases comparing the SST-model with k-ε and k-ω models. He uses experimental data and results from simulations with a v2f turbulence model for validation of the results. The latter has shown good performance in the prediction of heat transfer problems. He finds out, that the SST-model is able to reach the same level of accuracy as the v2f-model, despite its lower number of equations. Furthermore, he points out that the grid must be sufficiently fine. However, the automatic wall treatment leads to a significant reduction in sensitivity to near wall resolution. [17]

It was given up on using the SSG Reynolds stress model as Bradshaw states "it is so obvious that stress-transport models are more realistic in principle than eddy viscosity models that the improvements they give are very disappointing and most engineers have decided that the increased numerical difficulties (complexity of programming, expense of calculation, occasional instability) do not warrant changing up from eddy-viscosity models at present. Even stress-transport models often give very poor predictions of complex flows - notoriously, the effects of streamline curvature are not naturally reproduced, and empirical fixes for this have been very reliable" [3].

5.7 Conclusion and Selection of Turbulence Model

The comparison of numerical results showed no severe discrepancy between the results of the three investigated turbulence models. The selection of a promising turbulence model has therefore been justified with the help of literature recommendations, which point out that the SST-model in most cases gives the best results, especially in connection with heat transfer. The k-ε model is often reported to bring worse results than the SST-model. In terms of result accuracy, the SSG Reynolds Stress model showed no outstanding improvement compared to the SST-model. Consequently, the SST-model was chosen for the following studies. Leschziner [8] underlines this choice with his remark that "turbulence modelling, at whatever level, is inevitably an exercise of compromise between predictive realism and computational effort".

6 Grid Size Study

The scientific way of conducting a grid size study is to refine a coarse mesh until no significant change in the solution results can be observed - until *grid convergence* is reached. In this paper, a rather engineer-like approach was made. The goal was to find a reasonable amount of elements, so that the aim of the study could be reached. The aim is, as already mentioned, a qualitative study of the flow characteristics and temperature distribution in the nacelle. Another goal is to make use of the (computational) resources in an economic way. The resource is the workstation on which the computations were running, with a limited amount of memory, restricting the desired grid size. The first grid was therefore fit to the memory available on one workstation. The grid study in this approach was intended to check whether the grid is already fine enough. A finer grid was realized and the results were compared with the normal size grid. As the goal is a result of qualitative nature, a relatively big difference between the solutions for the two meshes was accepted. A coarser mesh was generated in order to see if the same quality of results is achievable with fewer elements, resulting in faster solution runs. It was as well examined whether the grid size has an important effect on the convergence behavior.

It has to be said, that the grid size not only has an effect on the memory and time consumption during the solver run, but also on the disk space which is required for the result files. A small grid keeps solution time short and reduces result file size and memory consumption.

6.1 Description of the Grid

The three grids mainly differ in their boundary layer resolution. An overview over the grid parameters is given in table 6.2a, 6.2b and 6.2c. The element type describes which kind of element has been used to mesh the particular grid part. Hex-type grid parts are *structured*, cf. chapter 3.2.

The first element height describes the distance of the first node to the wall. It is used to describe the wall resolution. The smaller this distance is, the lower the dimensionless $y+$ value will be. Lower $y+$ values allow for some turbulence models a better prediction of the flow parameters close to the wall. This has an important influence on heat transfer and flow separation predictions, cf. chapters 5 and 6.5.

The height ratio is the factor used for the growth law of the boundary layer elements after the first node at the wall. The thickness of an element is the thickness of the preceeding element multiplied with this factor.

For comparison reasons, the quality of the worst element is given. In most grid parts the quality is acceptable (0.2 and higher) to very good ($\approx$1). Only a few grid parts have a quality worse than 0.2, which is usually cited as the lower limit for the quality [1; 9]. A quality value of 1 would indicate a perfectly regular mesh element. However, the number of remaining low quality elements (not shown here) compared to the total number of elements is evanescent.

The standard quality criteria of ICEM CFD have been used to judge the element quality. The quality criterion is depending on the mesh element type. Table 6.1 shows, how these criteria are defined for each element type. Detailed definitions of these and more quality criteria can be found in [13].

Table 6.1: Quality criteria in ICEM CFD

Element type	Quality criterion
Tri	minimum ratio of height to base length of each side, normalized to 1
Tetra	aspect ratio of the tetra element
Quad and Hexa	determinant
Pyramid	determinant
Prism	minimum of determinant and warpage

The height ratio and the first element height have the biggest influence on the total number of elements of each grid part when the geometry becomes complex. Only in a simple case or for tetraeder meshes, the size of the elements in surface direction has an important influence on the element count. For the grid part *Vorne* this size was increased between the normal and the fine mesh size. For the solution quality, the near wall refinement is more important than the resolution in the free stream regime. Especially where heat transfer plays a role, the wall resolution is crucial, which will be discussed in 6.5. The coarse mesh has about 45% of the element number of the normal mesh, which has about 52% of the element count of the fine mesh.

Table 6.2a: The parameters for the coarse mesh

Grid part	Element type	Element count	First element height mm	Height ratio	Worst element quality
Hinten	Hex	33690	25	1.5	0.6
FU	Hex	44000	25	1.5	0.6
Generator	Hex	339462	25	1.5	0.47
Turm	Hex	45400	20	1.5	0.4
Inletgitter	Hex	896	20	1.5	0.93
Kuehler	Hex	684	20	1.5	0.95
Huelle	Hex	271471	25	1.5	0.21
Vorne	Tet, Prism, Hexacore	375397	25-60	1.5	0.14
Luefter	Tet, Prism	10583	50	1.5	0.26
Total		1121583			

Table 6.2b: The parameters for the normal size mesh

Grid part	Element type	Element count	First element height mm	Height ratio	Worst element quality
Hinten	Hex	104027	10	1.4	0.6
FU	Hex	133144	10	1.4	0.57
Generator	Hex	686502	10-25	1.4-1.5	0.58
Turm	Hex	133492	10	1.3	0.37
Inletgitter	Hex	5859	10	1.2	0.98
Kuehler	Hex	4464	10	1.2	0.95
Huelle	Hex	668192	12	1.4	0.35
Vorne	Tet, Prism, Hexacore	738694	20-60	1.2-1.5	0.15
Luefter	Tet, Prism	9592	15	1.3	0.28
Total		2483618			

Table 6.2c: The parameters for the fine mesh

Grid part	Element type	Element count	First element height mm	Height ratio	Worst element quality
Hinten	Hex	316458	5	1.3	0.6
FU	Hex	521220	6	1.2	0.43
Generator	Hex	1489148	8-12	1.2-1.3	0.5
Turm	Hex	364572	5	1.2	0.39
Inletgitter	Hex	9044	5	1.2	0.95
Kuehler	Hex	12555	5	1.2	0.95
Huelle	Hex	1051182	10	1.35	0.25
Vorne	Tet, Prism, Hexacore	1015876	20-60	1.2-1.5	0.12
Luefter	Tet, Prism	19102	3-5	1.2	0.28
Total		4799157			

6.2 Solution Setup

For each of the three meshes, the same boundary conditions and solver settings were applied in Ansys Pre. All solution runs were started with the same set of initial conditions. The initial conditions were calculated using an older version of the normal size mesh - the final normal size mesh was refined at some points. The first solution for the initial conditions was reached in three steps. At first, only an initial guess for the flow field excluding heat sources, and buoyancy was calculated. After that, one solver run was done with heat sources and a final run included buoyancy. The result file of the final run was used as initial guess file for the solver runs with the final coarse, normal and fine meshes.

Tables 6.3 and 6.4 give an overview of the applied boundary conditions and solver settings used for the grid size study.

Table 6.3: Boundary conditions for
the mesh size comparison

Boundary conditions	
Outlet	
Normal speed	$3.3\,\mathrm{m/s}$
Inlet *Turm* and *Huelle*	
Type	opening
Relative Pressure	0 Pa
Flow direction	normal to boundary
Static temperature	20 °C
Turbulence	medium, 5 %
Heat sources with conjugate heat transfer	
FU (converter box)	4080 W
Generator	10630 W
Getriebe (gearbox)	8840 W
Kühler (gearbox oil chiller)	71000 W

Table 6.4: Solver settings for
the mesh size comparison

Solver settings	
Advection scheme	high resolution
Convergence criteria	RMS
Residual target	10^{-4}
Solver precision	double
Solid time-step control	automatic
Fluid time-step control	physical, $0.1\,\mathrm{s}$
Heat transfer	total energy
Solid	steel
Fluids	air, ideal gas
Turbulence model	SST
Buoyancy turbulence	none

6.3 Convergence Behavior

The RMS residual plot for momentum and mass, shown in figure 6.1, demonstrates that the residuals for the momentum do not reach the convergence criterion of 10^{-4}. The solution runs have been stopped as the monitor quantities, namely the averaged static temperature at the outlet, cf. figure 6.2, and the integral mass flows at the inlets, cf. figure 6.3, did not vary much. This level of convergence is acceptable to get an idea of the basic flow phenomena [1].

The Ansys documentation gives several approaches to improve convergence. It was tried to change the time step, improve grid quality and change the advection scheme blend factor with no significant melioration of the convergence behavior. The documentation indicates that transient effects might be the cause for this and for the fact that the mechanisms to improve convergence do not work.

However, resuming the goal of this diploma thesis, the achieved level of convergence is acceptable as far as qualitative results are demanded, provided that the variation of flow parameters due to the transient effects are negligible. (see chapter 7)
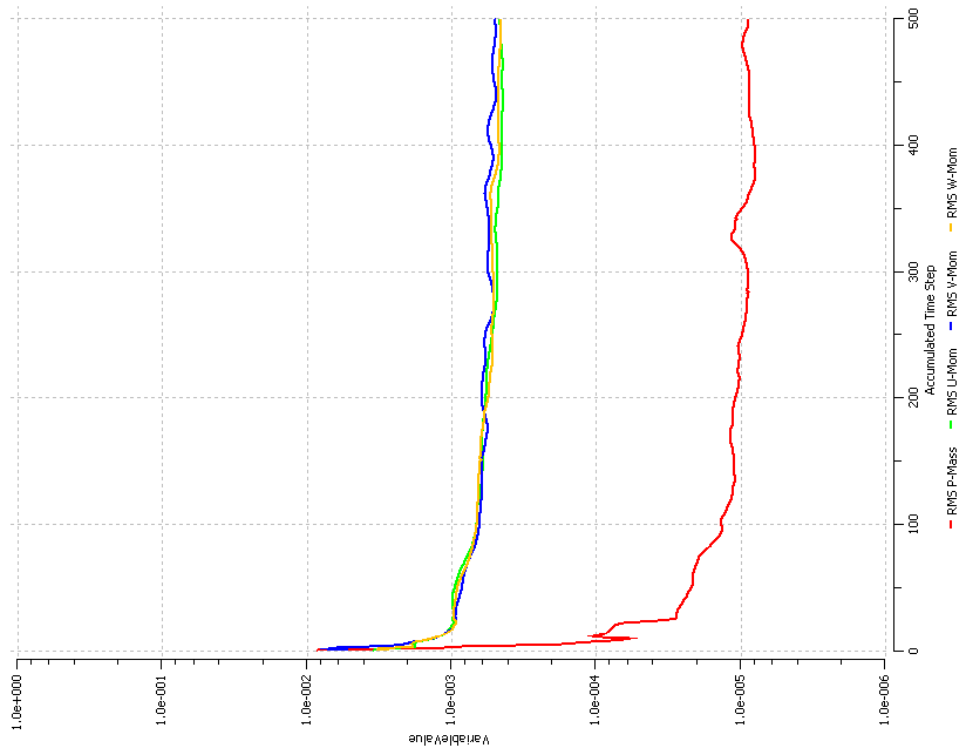
Figure 6.1: Residual plot for momentum and mass for the normal size mesh
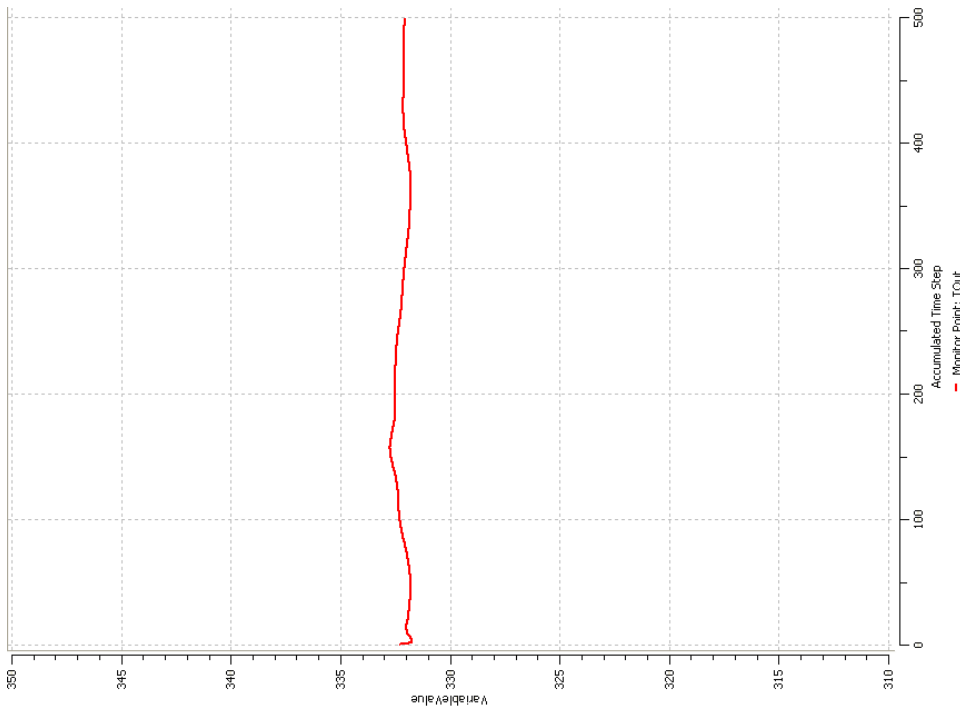
Figure 6.2: Monitor plot for averaged static temperature at outlet in °K
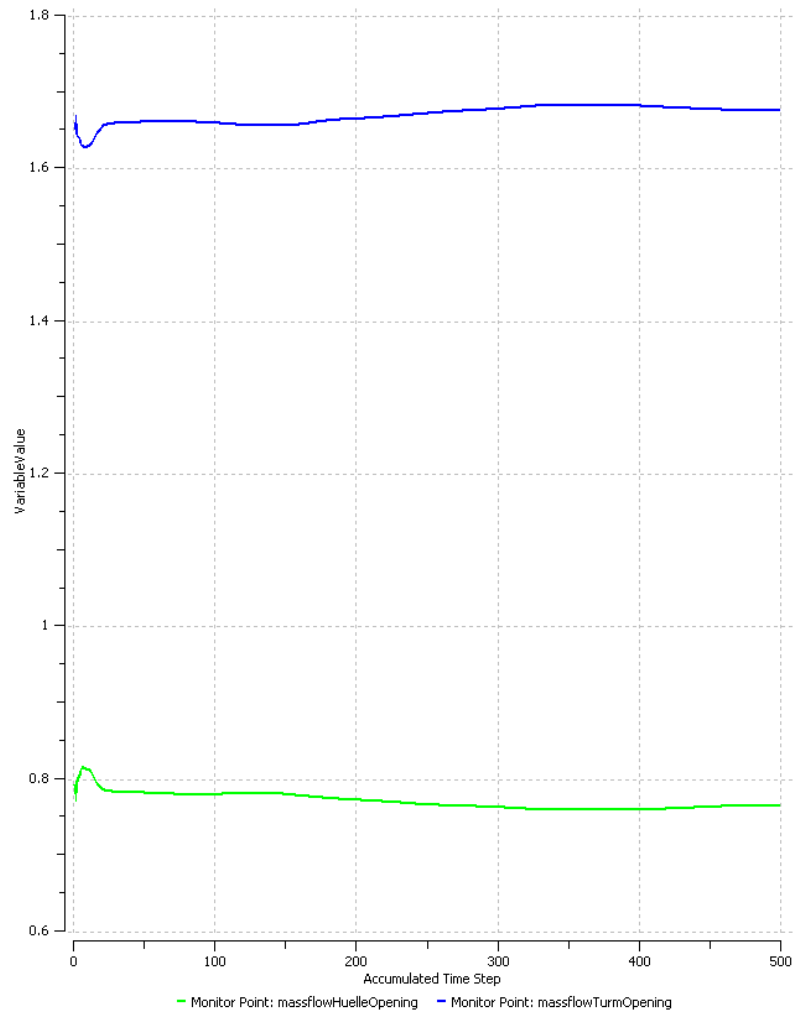
Figure 6.3: Monitor plot of integral mass flows at the inlet openings

6.4 Mesh Size Study Results

Like in chapter 5.5, the numerical results were compared by the use of sample planes. The same session file for creating sample planes was used and the integrated mass flow and averaged temperatures were analyzed. Furthermore, the total mass flow at the two inlets (one at the tower connection, one at the cover) and the air temperature at the outlet were evaluated. The course of action described corresponds to what Hölling [7] recommends as far as interpretation of numerical results is concerned.
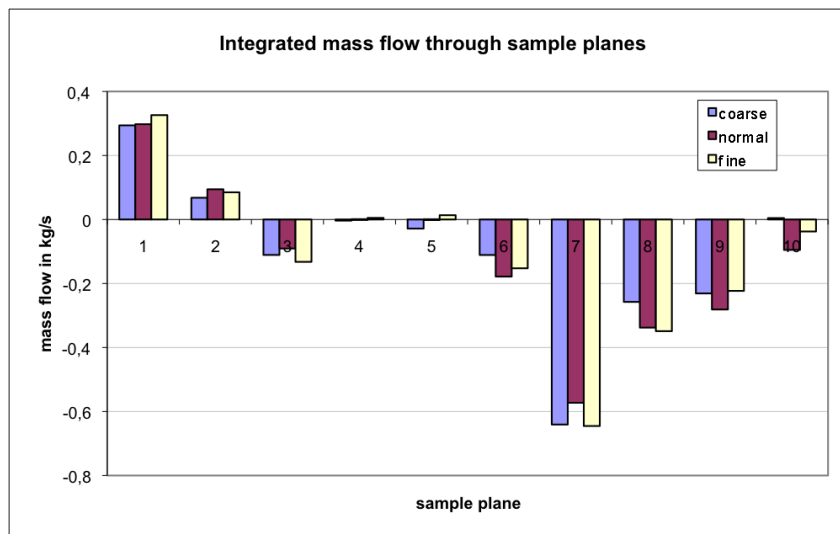
Figure 6.4: Differences in integral of mass flow over the sample planes

Figure 6.4 shows clearly that the integrals of mass flows over the sample planes are of the same order of magnitude for each of the three mesh sizes. The differences are very small and a tendency to one final value cannot be identified, cf. plane seven. In plane four, five and ten, the mass flows even change sign, which means a change of direction of the average mass flow. The absolute change, however, is still very small.

The fact that there is no tendency to one value as well as the bad convergence behavior of the solutions support the assumption that there is no steady state solution for this problem.

Figure 6.5: Mass flows at the inlets

Figure 6.5 demonstrates that the absolute values of mass flows integrated over the inlet openings are nearly identical for the three mesh sizes. This fact is explained by the mass and energy balances, which have to be equal for the three cases, keeping in mind that the boundary conditions were identical in all cases.
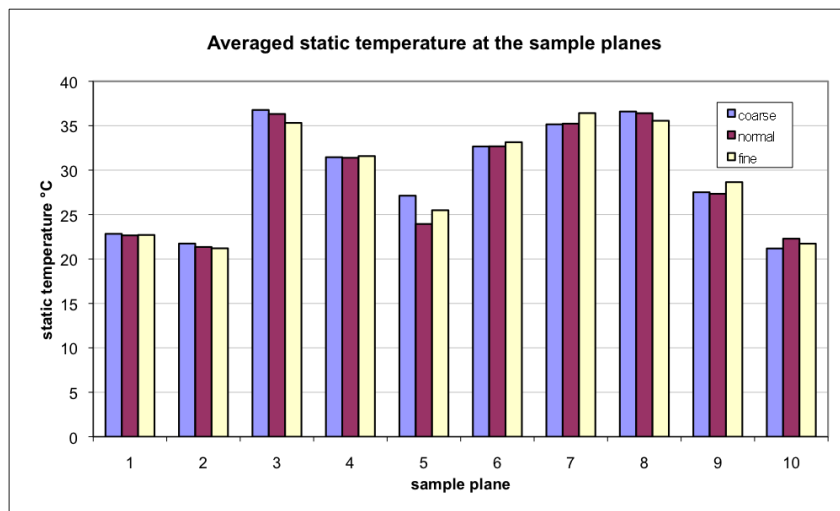
Figure 6.6: Averaged static temperature at sample planes

Figure 6.6 shows the averaged static temperatures at the sample planes. There is no tendency towards one value, see planes five and ten. The absolute variation of the values is very small.
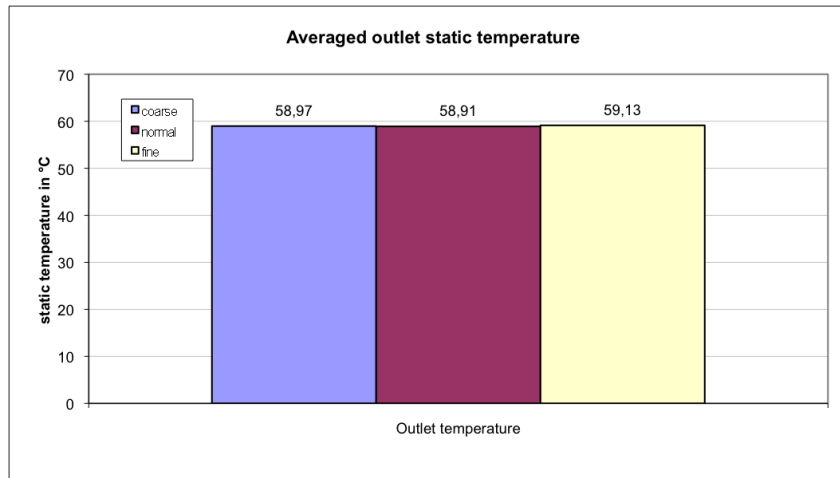
Figure 6.7: Averaged static temperature of the three grid sizes

Similar to figure 6.5, figure 6.7 illustrates that the parameters at the boundaries of the calculation are not influenced by the grid sizes. The temperatures are nearly identical.

6.5 Analyzing Control Box Surface Temperatures

While the flow paths and velocity profiles do not show a big sensitivity to the grid size, the surface temperature at the heat sources show important variances.

To evaluate, whether the use of wall functions or the low-Re method makes a crucial difference for heat transfer prediction, the grid has been drastically refined at one particular location (around the converter cabinet). The study has been conducted on the coarse, normal size and fine meshes. A further refinement was effected only for the grid around the converter cabinet and the mesh domain *FU*. For these fourth and fifth grid sizes, called *FU refined* and *FU superfine*, only the boundary layer of the surface of the converter cabinete in the grid part *FU* of the normal size mesh was further refined. The parameters for the other grid parts and the other surfaces in the grid part *FU* correspond to table 6.2b. The height of the first element was reduced and the growth rate factor was set to 1.2 for the grid part *FU* . The parameters and resulting element counts for the five mesh sizes of the grid part *FU* are summed up in table 6.5. The two adapted meshes for the grid part *FU* were then inserted into the rest of the normal size mesh. A global refinement for all grid parts in this order of magnitude was not achievable due to limited memory.

Figure 6.8 illustrates the stepwise refinement of the boundary layer grids that were realized in the five grid sizes for this study. Each of the five figures shows exactly the same location. The grey area at the left represents a part of the solid domain of the converter cabinet.

Table 6.5: Parameters of the refined surface of
the converter box in the grid part *FU*

Grid part	Element type	Element count	First element height	Height ratio	Worst element quality
			mm		
FU coarse	Hex	44000	25	1.5	0.6
FU normal	Hex	133144	10	1.4	0.57
FU fine	Hex	521220	6	1.2	0.43
FU refined	Hex	1186698	1	1.2	0.4
FU superfine	Hex	1682118	0.5	1.2	0.33

The gridlines normal to the surface are not identical in the five cases, as they are indirectly depending on the changed grid parameters. Figure 6.9 shows temperature contours at the same location. The grid lines are plot for the fluid domain only and the leftmost vertical line designates the wall.

An important change of the temperature profiles can be observed from figure 6.9a to 6.9c. After that, the temperature profiles are very similar. The big difference between the three coarsest and the two finest meshes is that there are several grid nodes in the temperature boundary layer for the two finest meshes. The prediction quality of the wall temperature is closely connected to the way that the turbulence model treats near wall boundary flow and heat transfer. For the prediction of the convective heat transfer at a wall, it is important that the flow in the boundary layer is resolved in detail. This is not possible with the wall function approach used in many turbulence models. According to Neale [11], wall functions are not valid for thermally developing regions. Therefore, it was tried to make use of the low-Re wall treatment of the SST-model by adequately refining the grid, which means resolving the viscous sublayer. According to Tu [16] this requires $y+$ values close to unity, but also values up to $y+ \approx 5$ are acceptable as long as the first node remains within the viscous sublayer. The SST turbulence model implemented in Ansys CFX switches to the low-Re wall treatment, at first partially and starting from $y+ < 2$ it switches completely by use of a blending functions [1]. The grid must be fine close to the wall like it was done for the meshes *FU refined* and *FU superfine*, cf. figures 6.8d and 6.8e. The fine resolution close to the wall ensures that the automatic wall treatment of the SST-model switches from the wall function method to the low-Re method, which is more accurate for heat transfer problems. For details on automatic wall treatment see chapter 5.3.2. In the finest two meshes, the SST turbulence model has obviously switched from wall functions to low-Re formulation. The main temperature change from wall to fluid is resolved with more than one element layer on the fluid side. This is only possible if the dimensionless wall distance $y+$ is very small.
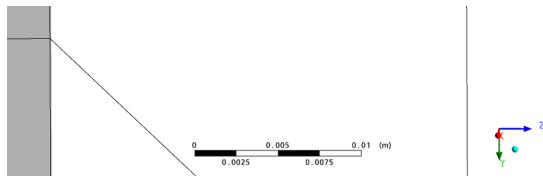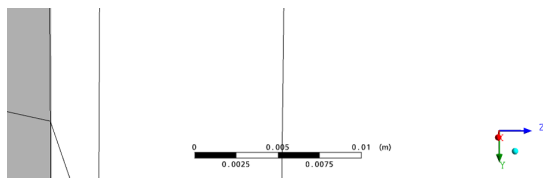
(a) Coarse grid
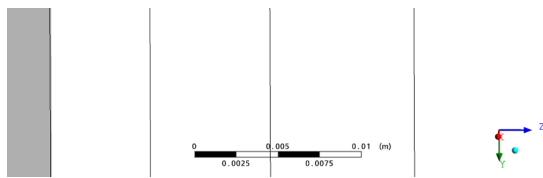
(b) Normal grid

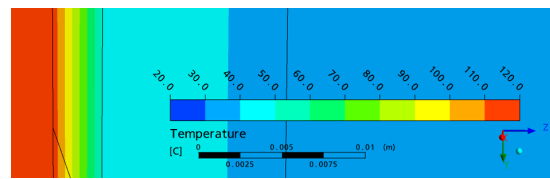

(c) Fine grid
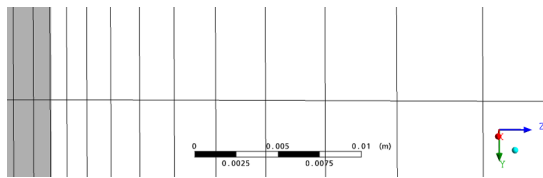
(d) FU refined
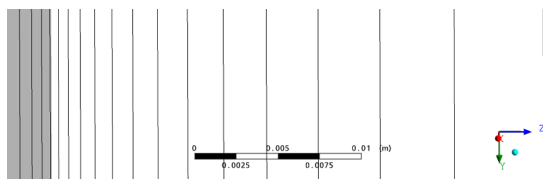
(e) FU superfine
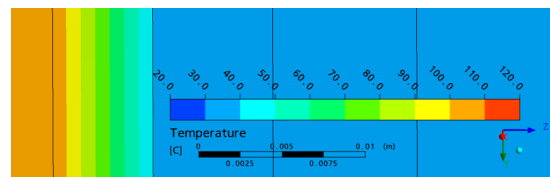
Figure 6.8: Comparison of grid sizes at the converter box surface
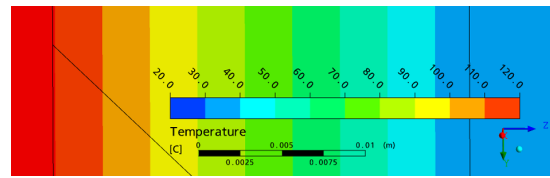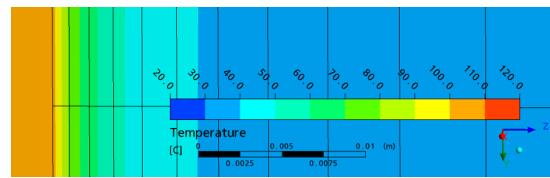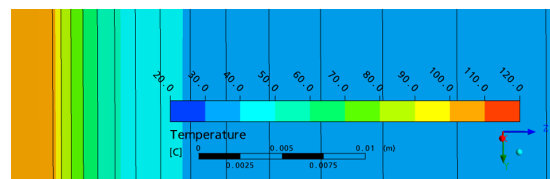

(a) Coarse grid temperatures

(b) Normal grid temperatures

(c) Fine grid temperatures

(d) FU refined grid temperatures

(e) FU superfine grid temperatures

Figure 6.9: Comparison of temperature contours at the converter box
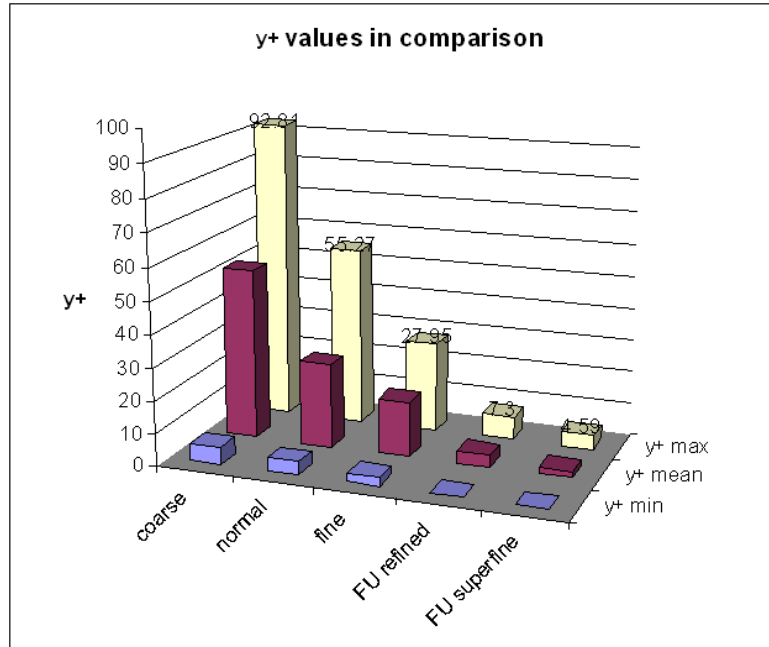
Figure 6.10: Comparison of the y+ values for the five grid sizes
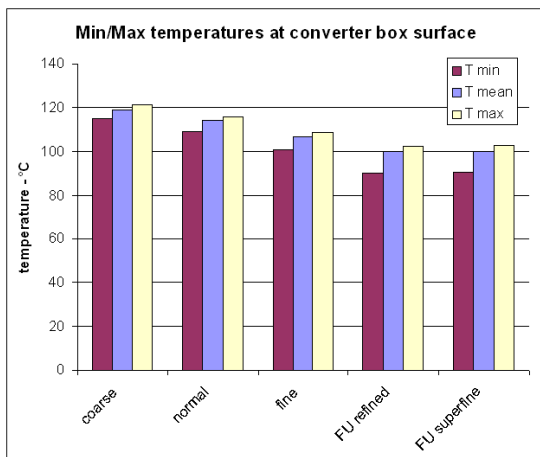
Figure 6.11: Min/Max/Mean temperatures for the grid sizes at the converter box wall
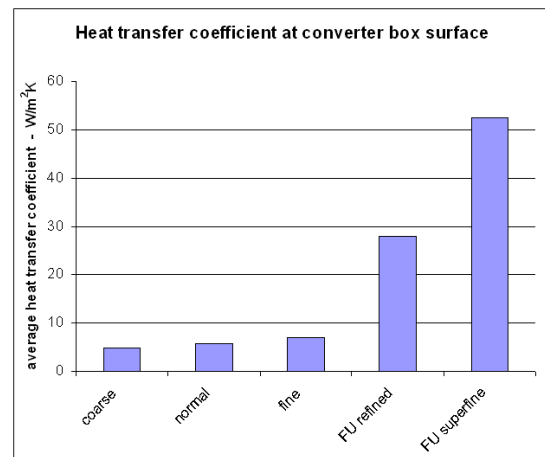
Figure 6.12: Mean heat transfer coefficient for the grid sizes at the converter box wall

The $y+$ values for the five meshes are shown in 6.10. At the converter box surface, the average value for $y+$ for the finest mesh is around 2, which is already a good value for predicting heat transfer with the SST-model. The minimal, maximal and average temperatures at the converter box surface are plot in figure 6.11. The temperature levels decline from the coarsest mesh down to the mesh *FU refined*, whereas the temperature levels of *FU refined* and *FU superfine* are nearly the same. Looking at figure 6.12, a slowly increasing heat transfer coefficient for the three coarsest meshes and a jump for the two finest meshes can be seen. Interestingly, the approximative doubling of the heat transfer coefficient between *FU refined* and *FU superfine* does not lead to further changes of temperature levels.

Obviously, the mesh *FU refined* is *fine enough* for this application. The problem is that increasing the boundary layer refinement for the heat sources in the other domains would lead to an enormous increase of the global element count and was therefore not applicable for this study.
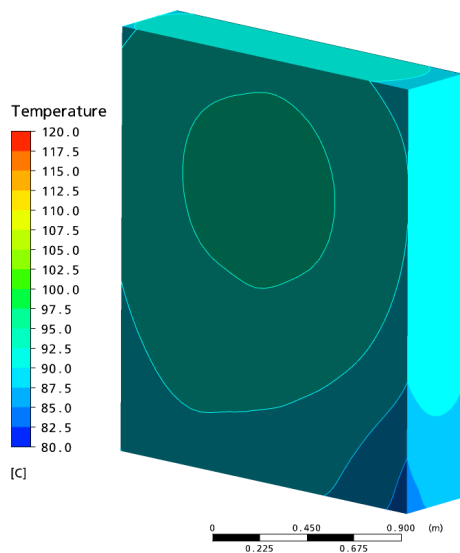
Figure 6.13: Surface temperature as contours for the converter cabinet at the finest grid size
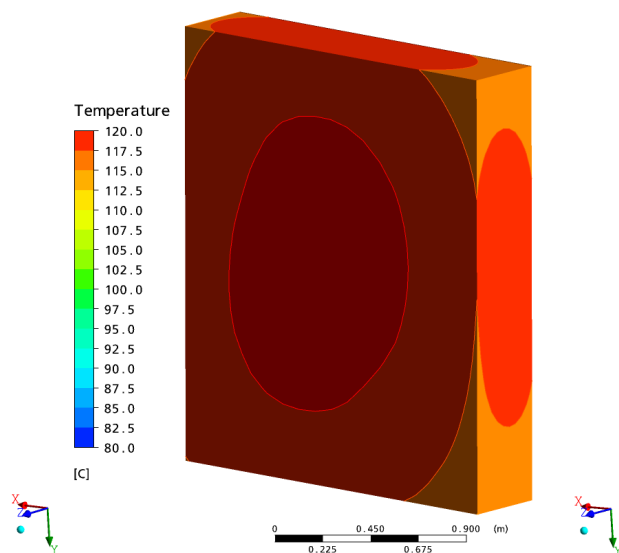
Figure 6.14: Surface temperature as contours for the converter cabinet at the coarsest grid size

Finally, figure 6.13 shows the surface temperatures for the finest grid, i.e. the normal size grid with the superfine mesh around the converter box, whereas figure 6.14 shows the results for the coarsest mesh. The average temperature is about 20°C lower for the refined mesh. The temperature gradients (distance and distribution of contours) for both plots are very similar. The corners are the coldest spots, as expected due to the advantageous volume-to-surface ratio.

6.6 Grid size study conclusion

Grid refinement mainly took place at the surfaces. Analyzing the results of the three grid sizes it becomes obvious that there is no crucial influence at this level of coarsening or refinement respectively as far as flow paths, velocity profiles and the global quantities of mass flow and air outlet temperature are concerned. It is therefore legitimate to use the smallest grid size in order to receive qualitative results for the flow field and air temperature distribution. A investigation of changes due to further coarsening has not been conducted but might be of interest.

The quantities mentioned are not very sensitive to changes in near wall grid size. Other quantities, like the surface temperature and heat transfer coefficient at walls with conjugate heat transfer, show an important sensitivity to the grid size. The resulting values for the surface temperatures, even at the finest grid size, are still by far not realistic. This may however be due to a lack of detail in the geometric modeling of the geometry parts concerned. The converter cabinet, for example, has been modeled as a solid steel cuboid, which is certainly a rude simplification. In real, the converter cabinet contains cavities, cooling fins, a rough surface and has a distinct cooling unit. All these details were left apart. Similar simplifications have been made for the other heat sources (namely the generator, the gearbox and the oil chiller). This has been necessary to keep the number of nodes low and, more important, the amount of work for the grid generation in a reasonable frame. Furthermore, the required mesh for resolving the wall heat transfer in detail would have exceeded the limited memory capacities.

Undoubtedly, the results for wall heat transfer and surface temperatures for the coarse, normal size and fine meshes are incorrect. Nevertheless, they may be useful to identify potential hotspots and to locate regions with high temperature gradients. If a detailed investigation of heat transfer and temperatures is of interest, a separation of the examined grid part from the rest of the problem might be advantageous. For the boundary conditions at the disconnected interfaces the results of beforehand calculated global solution runs could be used. Thus, a high level of refinement might be achievable.

7 Transient Study

For the case that a solution does not reach an acceptable level of convergence, the documentation of Ansys CFX [1] recommends, amongst others, to set up a transient run. This run shall clarify whether the steady state solution cannot reach the convergence criteria due to the nonexistence of a steady state solution. In total, 72 seconds were calculated, using a time step of 0.1 seconds. The coarsest mesh was used for the calculations, cf. table 6.2a. A result file on the same mesh, which RMS residuals had converged to below 10^{-3}, was used to provide initial values for the start of the run.

No steady state solution was reached after 72 seconds. The results of the transient run show a distinct fluctuation of the flow field velocities and temperatures. Sample planes were used to display this variation, like in chapter 6.4. For comparison, the plots for the sample planes 1 and 10 were combined in one diagram. The selection of these two sample planes was made based on the mean value of the mass flows. Sample plane 1 shows the highest absolute mean value for the mass flow, whereas sample plane 10 shows the lowest one. The mass flows and the average temperatures were evaluated for every time step for each sample plane. The resulting plots show an important variation of the target variables.

7.1 Mass Flows at the Sample Planes

Figure 7.1 shows the mass flows for the sample planes 1 and 10 for the calculated 72 seconds. The mean values for each of the two sample planes are given. Their difference is due to the location of the sample planes and their corresponding flow situation. However, the main concern of this diagram is not this difference, but the fluctuation of the mass flows around the mean value of the corresponding plane. One can observe that the absolute amount of deviation is very similar for both sample planes. A periodic behavior or a stationary final value cannot be found for any of the sample planes after 72 seconds.

The deviation of the mass flow from its mean value in percent is of interest to judge the importance of the fluctuations. Figure 7.2 demonstrates this percentage for the example sample planes. The percentage is equal to zero if the mass flow reaches the mean value. The percentage is much more important for sample plane 10, because the absolute value of the mean mass flow is very small compared to its fluctuation. Hence, the percentage is more important for sample plane 10 than for sample plane 1. The absolute variation of the mass flows is of the same order of magnitude for both sample planes. A relation of the mass flows of the sample planes to the averaged total mass flow through the nacelle would increase the comparability of the deviation for different sample planes.

7.2 Temperatures at the Sample Planes

The average temperatures at the example sample planes are demonstrated in figure 7.3 to show the variation of the temperatures over time in the nacelle. The figure shows that there is no steady state solution after 72 seconds. The deviation of the temperatures from their mean value are of the same order of magnitude. Similar to the mass flows, no periodicity of the fluctuation can be observed. The two sample planes show similar mean values for the spatially averaged temperature.

Figure 7.4 demonstrates the deviation of the locally averaged temperature in percent of the corresponding mean value. The percentage is equal to zero if the locally averaged temperature at the sample plane reaches the temporally averaged mean value. The maximum percentage of deviation is lower than 2 percent in the calculated time span. The temperature results are quite reliable if judged by the presented percentage. The comparability of the deviation for different sample planes could be increased by relating them to the averaged outlet temperature, for example.
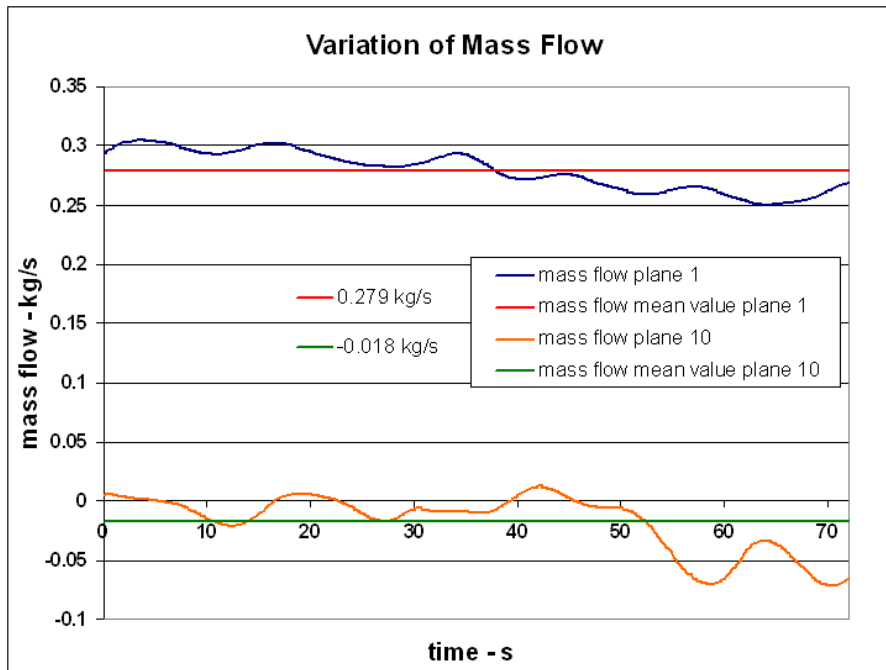
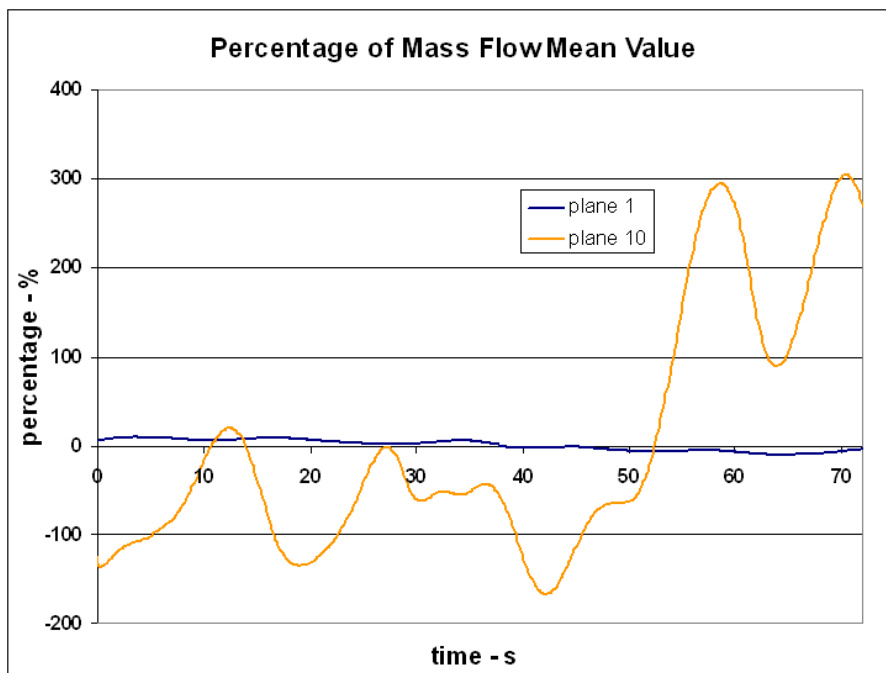**Figure 7.1:** Fluctuation of mass flow at sample planes 1 and 10 over 72 seconds

Figure 7.2: Fluctuation of mass flow in percent of the mean value at sample planes 1 and 10
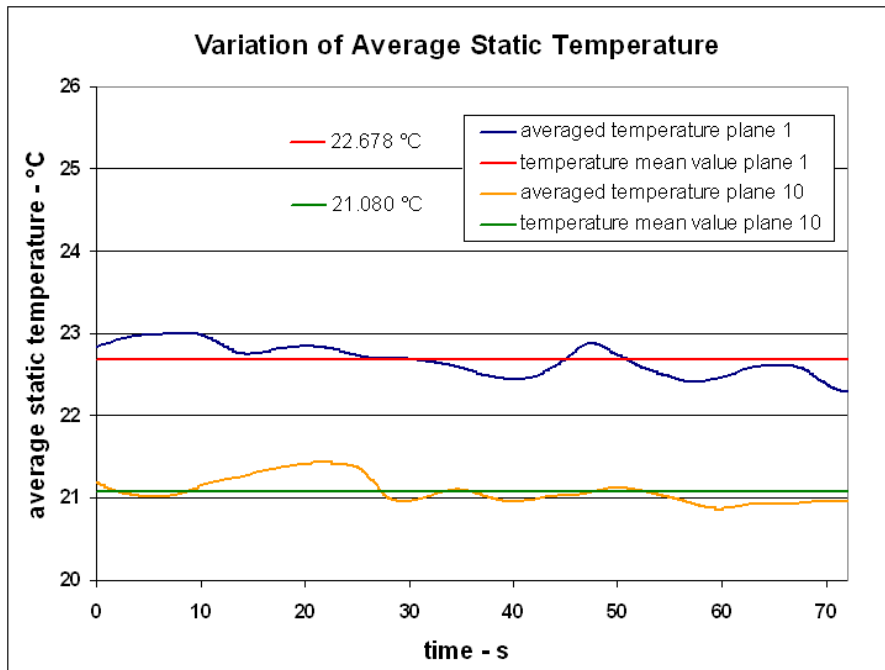
Figure 7.3: Fluctuation of the temperature at sample planes 1 and 10 over 72 seconds
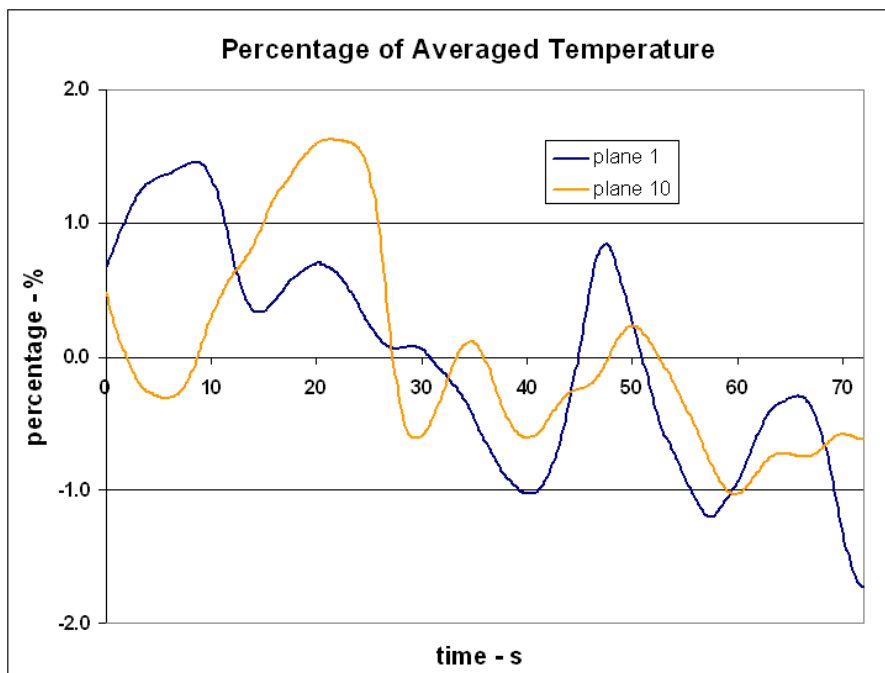

Figure 7.4: Fluctuation of temperature in percent of the mean value at planes 1 and 10

7.3 Mass Flows at the Inlets

Figure 7.5 shows that the fluctuations of the mass flows at the two inlets are directed opposite to each other. The left ordinate shows the scale for the mass flow through the inlet *Turm* at the tower, whereas the right ordinate shows the scale for the inlet *Huelle*, located at the cover of the nacelle.

Figure 7.6 demonstrates that the total mass flow through the nacelle is almost constant over time. The amount of the total fluctuation is very low. This leads to the conclusion, that only the flow paths inside the simulated volume fluctuate. The behavior of the variations is aperiodic.

7.4 Comparison with Steady State Results

The results of the transient calculation were averaged over the 72 seconds to compare them with the steady state solution from the normal size mesh, which was used for the grid study in chapter 6. The characteristics of the normal size mesh are summed up in table 6.2b. For the boundary conditions and the solver setup, see tables 6.3 and 6.4. The transient run should be continued for a longer time span to improve the significance of this comparison. The sample planes were used like before to evaluate the mass flows and the average temperatures at ten positions.

The results for the mass flows are presented in figure 7.7. A strong discrepancy between the averaged transient result and the steady state result is visible for many of the sample planes.

The behavior of the results for the averaged temperatures is similar to the results of the mass flows, cf. figure 7.8. There is a discrepancy of the target values for most sample planes, but the results can still be considered as qualitatively representative.
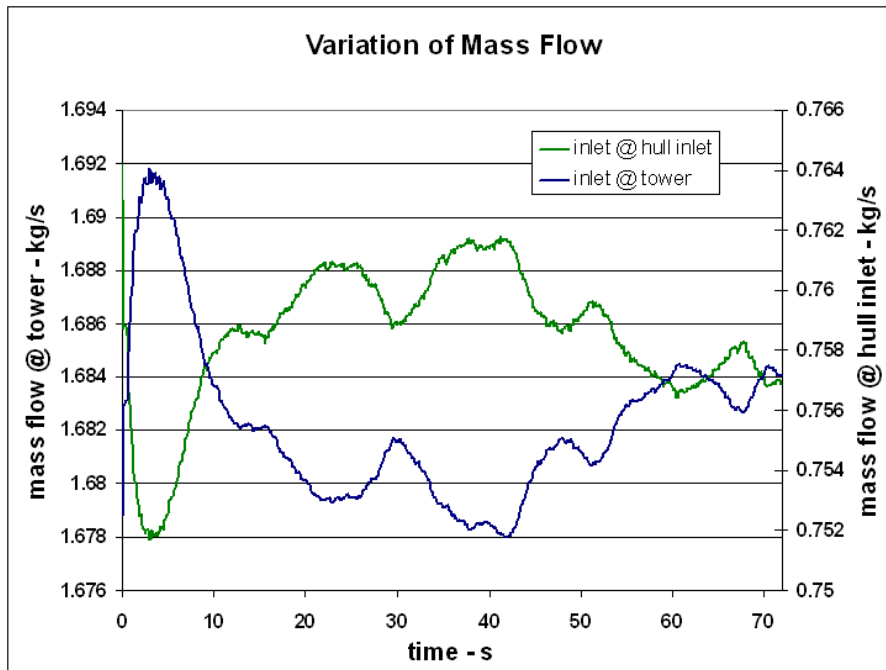
Figure 7.5: Fluctuation of mass flows at the two inlets over 72 seconds
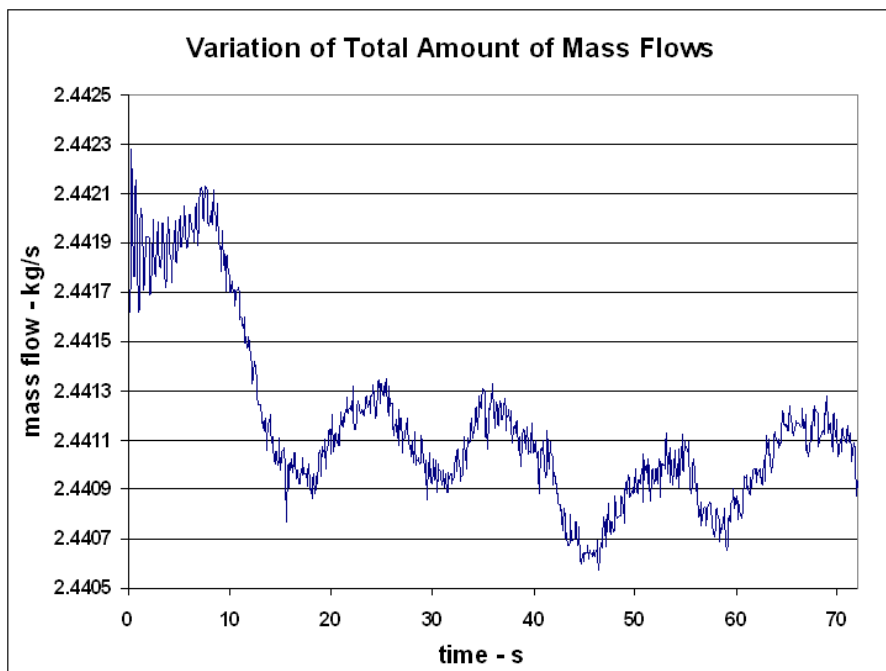
Figure 7.6: Total of the mass flows at the two inlets over 72 seconds
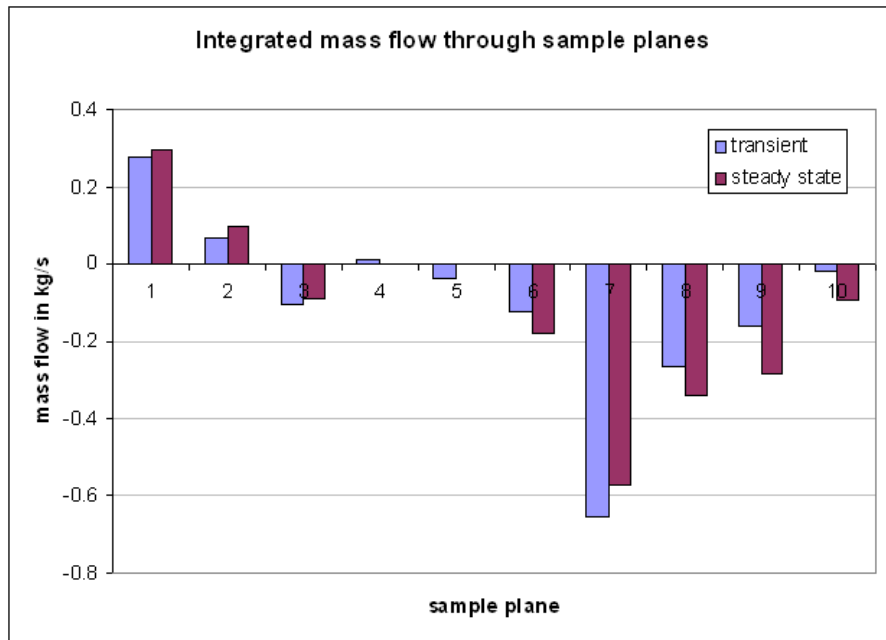
Figure 7.7: Comparison of averaged transient and steady state results for the mass flow at the sample planes
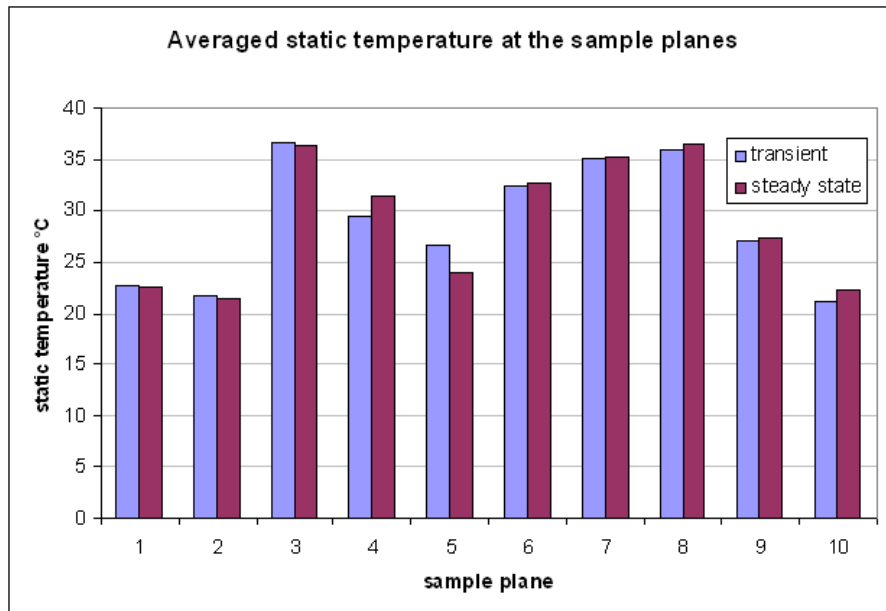

Figure 7.8: Comparison of averaged transient and steady state results for the temperature at the sample planes

7.5 Conclusion

In contrast to the deviation of the mass flows from the temporally averaged mean values, the temperature differences are acceptable if one keeps in mind that qualitative results are wanted. The analysis of the temporally averaged transient results give more reliable values, but the effort required for achieving these results does certainly not stand in relation to the possible gain. It may be a better option to meliorate the fluctuating behavior by minimizing other sources of error, like the grid quality and interpolation errors.

The existence of a steady state solution could not be confirmed with the transient solver run after 72 seconds. Either there is no periodic fluctuation, or the periodic time is bigger than 72 seconds. The aperiodicity of the results raises the question whether a periodic fluctuation will be reached after a longer time span. Continuing the transient run can clarify this question.

Eliminating other possible sources of error is recommended in order to affirm the assumption that a steady state solution does not exist. To do so, the grid quality could be further increased to reduce the influence of numerical errors. Furthermore, the interpolation errors at the domain interfaces could be reduced by combining some of the grid parts. A one-piece unstructured grid could be generated to compare its results with those of the subdivided grid. However, the size and the complexity of the geometry itself certainly have an impact on the behavior of the solution runs.

The strongly unsteady and aperiodic behavior is certainly responsible for most of the convergence problems during the steady state solution runs, as stated in the Ansys documentation [1]. Whatever the source of the aperiodicity may be, it is difficult to evaluate its significance for the following chapters 8 and 9, where the characteristics of the flow and temperature field are going to be analyzed. The results of steady state solution runs were used for these two chapters, so no transient effects were taken into account. It might be reasonable to use time-averaged results of the transient solution as a base for the flow field and temperature analysis. However, such an approach drastically boosts the computing time, which is necessary for one single solution.

8 Analysis of the Flow and Temperature Field

The geometry and model setup were analyzed and discussed in the preceding chapters. In this chapter, the flow and temperature field will be examined based on the final version of the geometry-, model- and solver setup. The solver setup is summed up in table 8.1. The boundary conditions are equal to the ones for the grid size study, cf. table 6.3. The normal size mesh was used as computational grid for this run, cf. table 6.2b.

Table 8.1: Solver settings for the final solution run

Solver settings	
Advection scheme	high resolution
Convergence criteria	RMS
Residual target	10^{-4}
Solver precision	double
Solid time-step control	automatic
Fluid time-step control	local time step, from $5\,\mathrm{s}$ to $0.1\,\mathrm{s}$
Heat transfer	total energy
Solid	steel
Fluids	air, ideal gas
Turbulence model	SST
Buoyancy turbulence	yes

The features of interest were defined by AMSC Windtec as follows:

- Volumetric flow and temperature at a horizontal section through the flow field

- Maximum speed in the flow field

- Streamline plots starting from two inlets, ending at the outlet

- Velocities and temperatures at the gearbox, its oil-chiller and the inlet at the hull

- Temperature distribution inside the heat sources

- Temperature distribution at the hull of the nacelle

These points are analyzed in the following sections.

8.1 Volumetric Flow and Temperature at a Horizontal Section through the Flow Field

The interest is the distribution of the volumetric flow in the computational area. Five horizontal sections through the volume were implemented and split in three parts, see figure 8.1. The parts were distributed in such a way that the front plane (red) displays the flow passing by the gearbox, the middle plane (green) displays the flow entering by the opening at the nacelle hull and passing by the generator and the rear plane (blue) hulls the flow in the rear part of the nacelle.
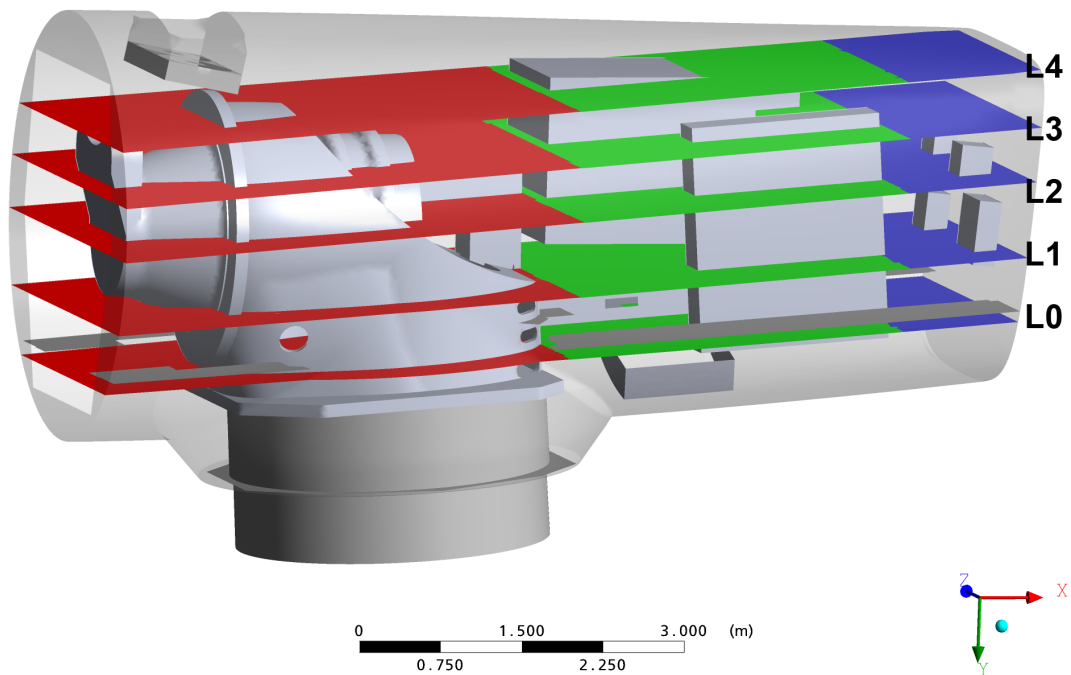
Figure 8.1: Heights and placing of section planes in the volume

The volume flow was evaluated for each of the plane parts at each height. The results are shown in the tables 8.2a, 8.2b and 8.2c. The sign of the flow represents its direction, where a positive value indicates an upwards directed flow. Only in height level L4 of the rear plane a net downwards directed flow can be observed, probably due to its proximity to the roof of the nacelle. The area of each plane was calculated and used to normalize the volume flow to one square meter, which gives the average flow speed. The principal part of the flow passes by the gearbox in the front of the nacelle. This can be explained by the size of the inlet at the tower connection under the mainframe, and furthermore it is close to the outlet. The distribution of the volume flow is very similar for the five heights.

Table 8.2a: Analysis of the five section planes in the front

Front planes height level	Volumetric flow m^3/s	Plane area m^2	Average speed m/s
L0	1.59	13.90	0.11
L1	1.63	12.48	0.13
L2	1.68	11.47	0.15
L3	1.66	12.58	0.13
L4	1.66	14.44	0.12

Table 8.2b: Analysis of the five section planes in the middle

Middle planes height level	Volumetric flow m^3/s	Plane area m^2	Average speed m/s
L0	0.34	9.79	0.03
L1	0.29	10.64	0.03
L2	0.29	7.23	0.04
L3	0.39	7.31	0.05
L4	0.44	7.79	0.06

Table 8.2c: Analysis of the five section planes in the back

Rear planes height level	Volumetric flow m^3/s	Plane area m^2	Average speed m/s
L0	0.09	3.58	0.02
L1	0.09	3.72	0.02
L2	0.07	3.95	0.02
L3	0.03	4.23	0.01
L4	-0.03	3.78	-0.01

Figure 8.2 displays temperature contours for three selected horizontal planes. All three parts of the planes were combined to show the temperature distribution. In height L1 the temperatures are still between 20 and 29°C in the free stream, higher temperatures are only reached close to the heat sources. The same is true for L2, which is situated 70 cm higher than L1, with the difference that the areas of higher temperatures are growing, especially in the rear (right side of depiction) part of the nacelle. The flow speeds are low in these areas which means as well that fresh air is transported there at lower rates. In the front part where the flow speeds are high, the temperatures are much lower even though the gearbox and its support both transfer heat to the fluid. The residence time of the air in the front of the nacelle is much shorter.

The hot boundary layers around the gearbox and its support are considerably thicker than those around the generator and the converter cabinet. Certainly, the grid is to be charged for this. The near wall grid resolution is much coarser in the unstructured grid part around the gearbox, as no wall refinement with prism layers could be realized. The near wall grid resolution is much finer in the structured domain around the generator and the converter cabinet. (compare with table 6.2b, where the near wall resolution is outlined for each grid part)

Temperatures rise considerably on height level L4 of the examined planes. Again, the temperature distribution is unequal. In the rear part the air temperatures reach values of 50°C and more in the free stream regime. The large hot areas above the generator and the gearbox, however, are due to the fact that the horizontal plane cuts right through the temperature boundary layer of the generator, where temperatures are very high. Behind the generator and the converter cabinet, temperatures reach 40°C in considerable areas.

A strong temperature gradient marks the border towards the front part of the nacelle, where temperatures drop to values lower than 23°C. In this location a jet of fresh air from the tower inlet reaches upwards to the roof of the nacelle. This jet of air is then mostly redirected towards the front of the nacelle and only small amounts flow backwards, mixing with the hot air above the generator and the converter cabinet. In the front part above the gearbox, the temperatures at this height level are very low due to the low residence time of the air in this part. Better ventilation of the rear part of the nacelle is recommended.
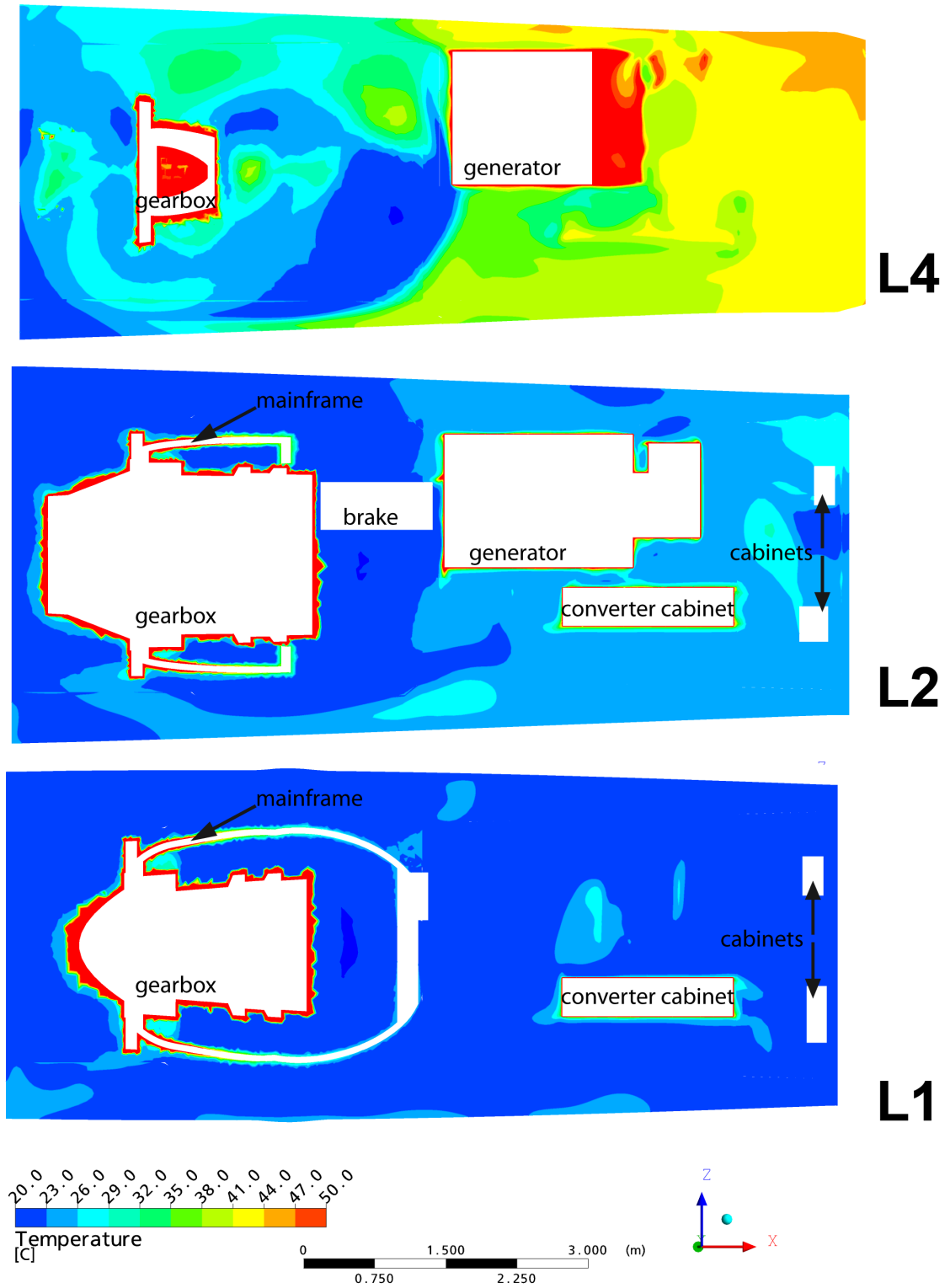
Figure 8.2: Temperature contour plots at the horizontal section planes

8.2 Maximum Speed in the Flow Field

To visualize the regions with the highest flow speeds, a series of iso-volume plots have been realized in Ansys Post. The represented iso-volumes comprise all mesh elements with flow speeds within the speed interval shown in the legend. The speed distribution within these elements is visualized by the color scale.

The maximum speeds in the flow field are naturally to be found close to the outlet ventilation, where speeds between 1.2 and 4.5 $^\mathrm{m}/\mathrm{s}$ are reached. Nowhere else in the nacelle the fluid speeds exceed these values. Figure 8.3 shows an iso-volume plot, picturing speeds between 1.2 and 3.0 $^\mathrm{m}/\mathrm{s}$. The outlet channel is visible as well as a part of the gearbox and its support. The transparent blueish surfaces represent the hull of the nacelle.
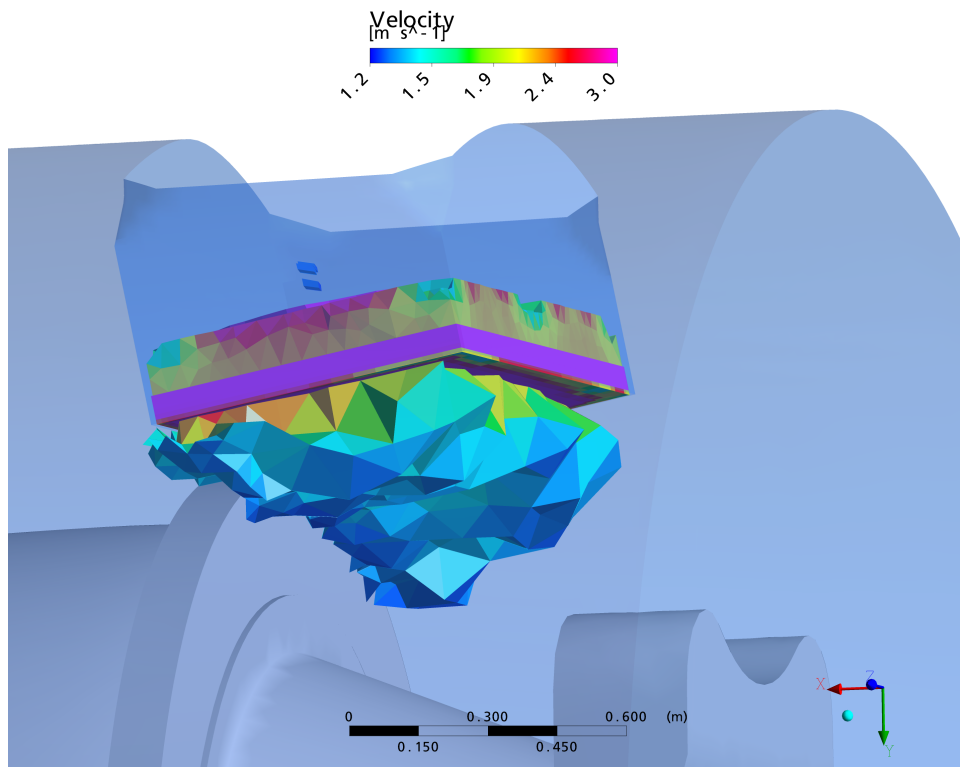
Figure 8.3: Maximum speeds around the outlet fans

The maximum speeds are between 0.8 and 1.2 $^\mathrm{m}/\mathrm{s}$ in the rest of the flow field. Figures 8.4a and 8.4b display iso-volume plots, this time showing speeds between 0.8 and 1.2 $^\mathrm{m}/\mathrm{s}$. The first plot shows speed peaks at the roof of the nacelle hull right above the gearbox, around the fans. Other small areas of high speeds are around the brake, where the flow from the tower inlet passes through a narrowed cross-section.
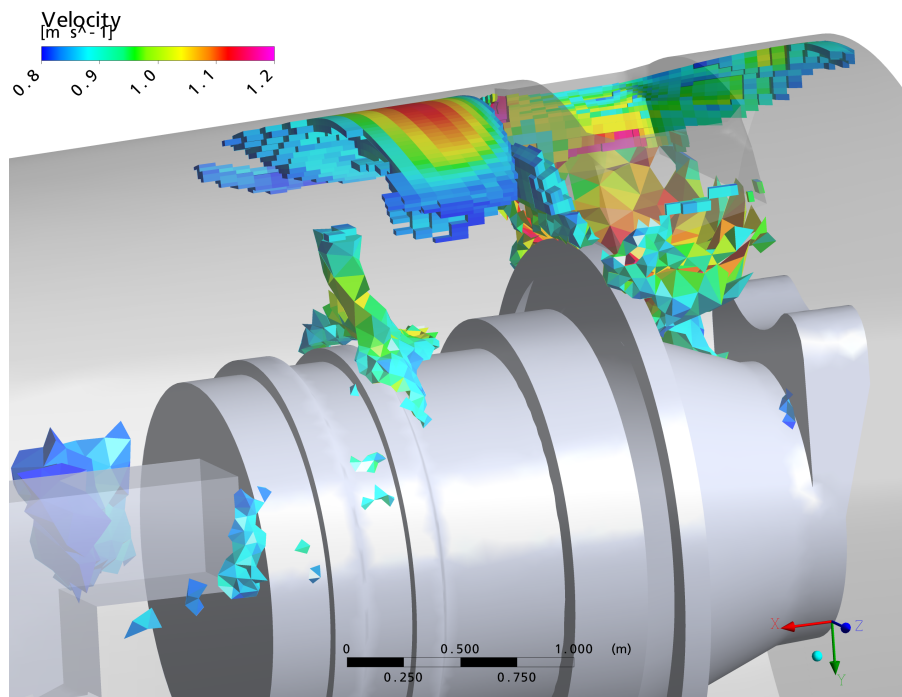
(a) Areas of high speed around the gearbox
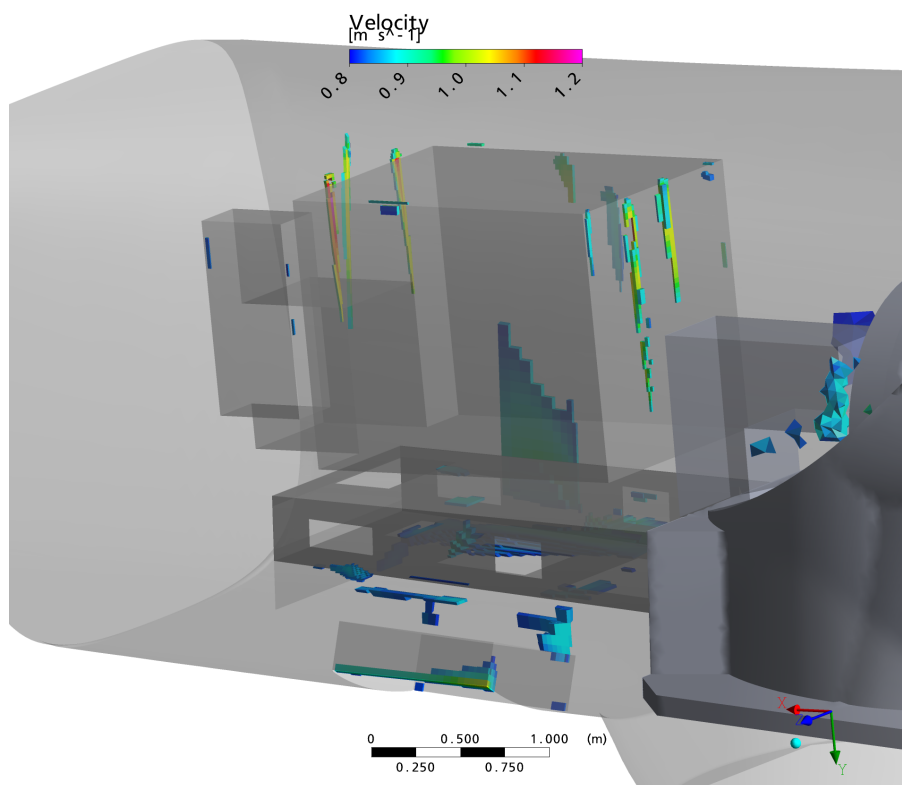
(b) Areas of high speeds in the rear part of the nacelle

Figure 8.4: Iso-volumes of flow speeds in the nacelle

64

Figure 8.4b shows small areas of high speeds in the rear part of the nacelle. To facilitate the inspection, the cabinets in the rear part of the nacelle, the floor elements and the converter box are hidden in this figure. There are some small areas of speed peaks around the inlet. High speeds are reached as buoyancy accelerates the flow at the surfaces of the generator and the converter cabinet. A general increase of the flow speed and flow rate around these two components is desirable to improve the cooling performance. As presented in the streamline plots in chapter 8.3, the flow rates in the rear part of the nacelle are very low.

One interesting detail showing a numerical issue is visible in figure 8.4b. The narrow flow paths at the surface of the generator in upward direction are subject to a sharp cut, all of them approximately at the same height - exactly where the *GGI* interface connection between two grid parts is situated. In these areas, interpolation takes place, which presumably is the cause for the conspicuous sharp cut of the flow speeds. The interpolation error can be avoided by matching the surface grids at the interface connection or by totally avoiding the division into grid parts, with all its effects on grid generation challenges.

8.3 Streamline Plots Starting from Two Inlets, Ending at the Outlet

In this section the most important flow paths in the nacelle shall be identified using streamline plots. The color of the streamline shows the local flow velocity. The interval displayed by the legend is 0 $^m/s$ as lower limit and 0.8 $^m/s$ as upper limit. The upper limit was chosen due to the results from the previous chapter 8.2 which have shown that speeds higher than 0.8 $^m/s$ are very rare in the flow field.

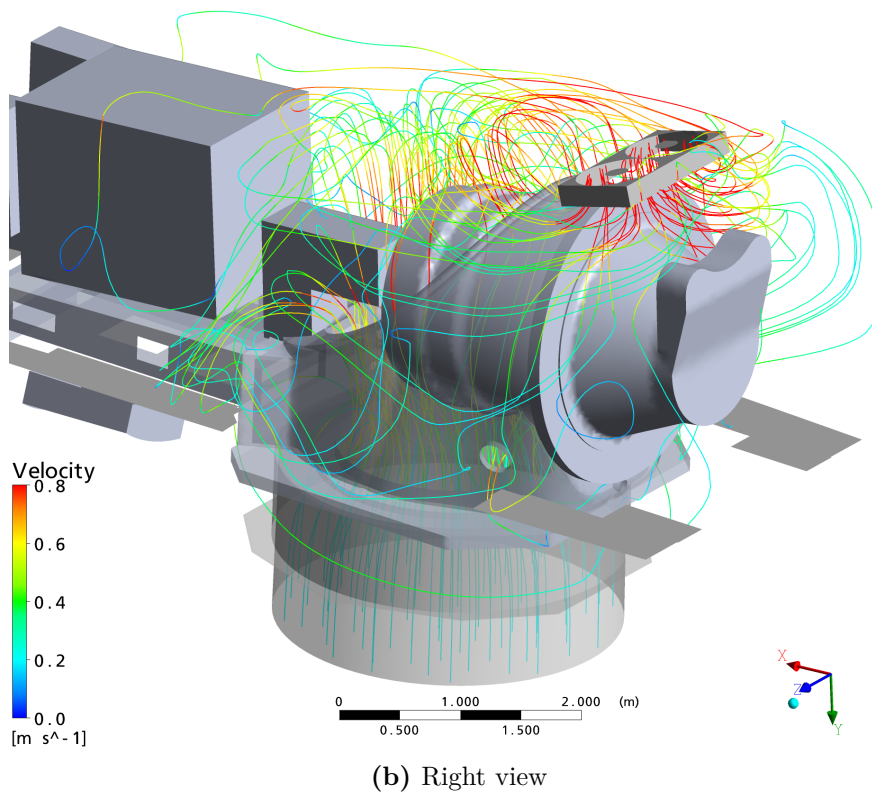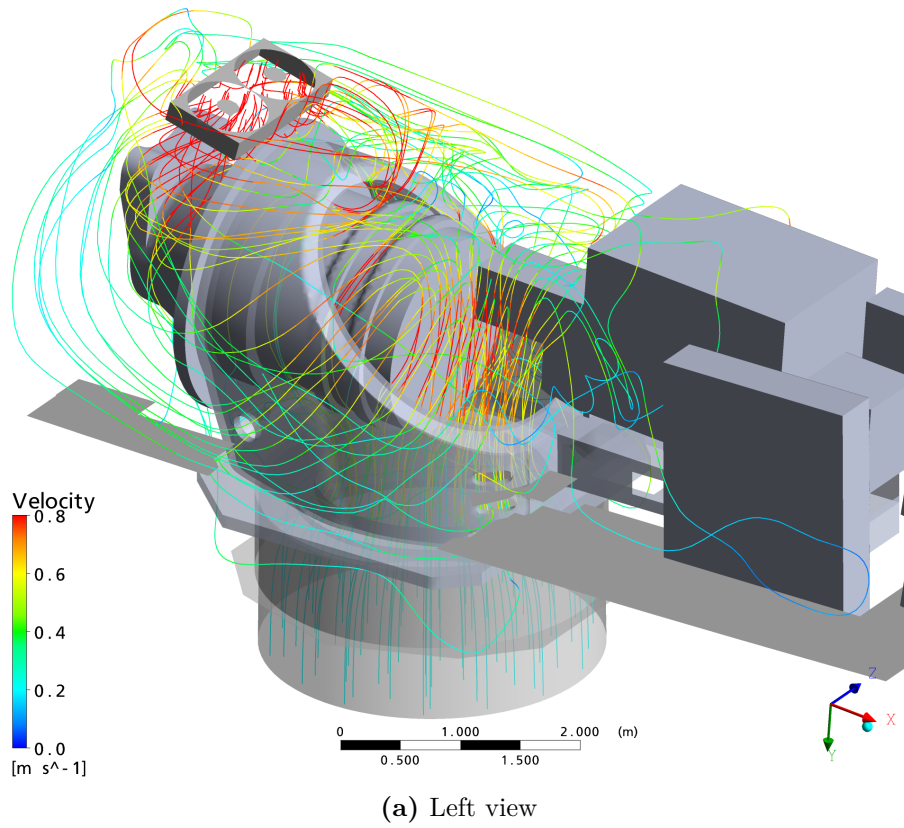Figure 8.5 represents 75 streamlines starting from the inlet at the tower connection. From this inlet, the main flow continues upwards, passes by the gearbox and brake and reaches the roof of the nacelle hull. The jet of air slows down at the roof of the nacelle, which is visible in figure 8.5a. It is mostly redirected to the front of the nacelle, flowing around the mainframe and down on its sides until the air is finally sucked in by the outlet ventilation, passing through the gearbox oil chiller which is situated right before the fans. Only small amounts of the flow entering at this inlet is going through the openings in the mainframe situated in the lower part. There are openings to the front part of the nacelle as well as to the rear part. One small opening is in the connection of the mainframe and the support of the generator, allowing the air to pass inside this bench. Streamlines for this flow path are shown in figure 8.6. Another small part of the air flow is redirected to the back of the nacelle, mixing with the air that is entering through the other opening.

The streamlines passing through the connection between the generator bench and the mainframe are depicted in figure 8.6. The opening connecting the generator support and the mainframe is highlighted with a red parallelogram. One can observe that the flow

through this passage originates from both inlets. At the passage, however, both flows are combined and one can no longer distinguish which part of the flow originates from which inlet. A part of the further flow passing through this connection enters the generator bench. It leaves this bench on the one hand towards the back of the nacelle, flowing by the generator and the converter cabinet. On the other hand a small amount swirls in the rear of the nacelle. Some of the streamlines even end as they reach the walls. Another big part leaves the generator support towards the lower part of the nacelle, flowing around the tower connection and rising upwards in the very front of the nacelle. There, it passes by the front part of the gearbox and goes into the heat exchangers and fans. The third considerable part of the flow leaves the passage surface towards the inner side of the mainframe. It flows towards one of its small openings where it changes to the outside of the support and joins the flow which circled the tower connection.

The situation is more complex for the air flow entering at the inlet, which situated at the hull of the nacelle, beyond the generator bench. This opening is equipped with a variable guide baffle. In this case, it was modeled as fully open with the air flow entering normally to the boundary surface, cf. table 6.3. The generator bench has openings so that the air can pass through it. A large amount of the air entering at this inlet streams upwards through this bench or around it, reaching the generator and the converter cabinet where it gets warmed up and, due to buoyancy, streams upwards while accelerating. As it reaches the roof, the air flows towards the front of the nacelle while a part of it keeps swirling in the rear part of the nacelle at very low speeds. Another part of the air entering at this inlet stays below the floor elements. It is slowly propagating forward around the tower connection until it finally streams upwards around the front of the gearbox. There, it is sucked in by the fans which are purging it out of the simulation volume. The flow velocities of the air entering at the rear inlet are considerably lower than those for the air entering through the tower.

(a) Left view

(b) Right view

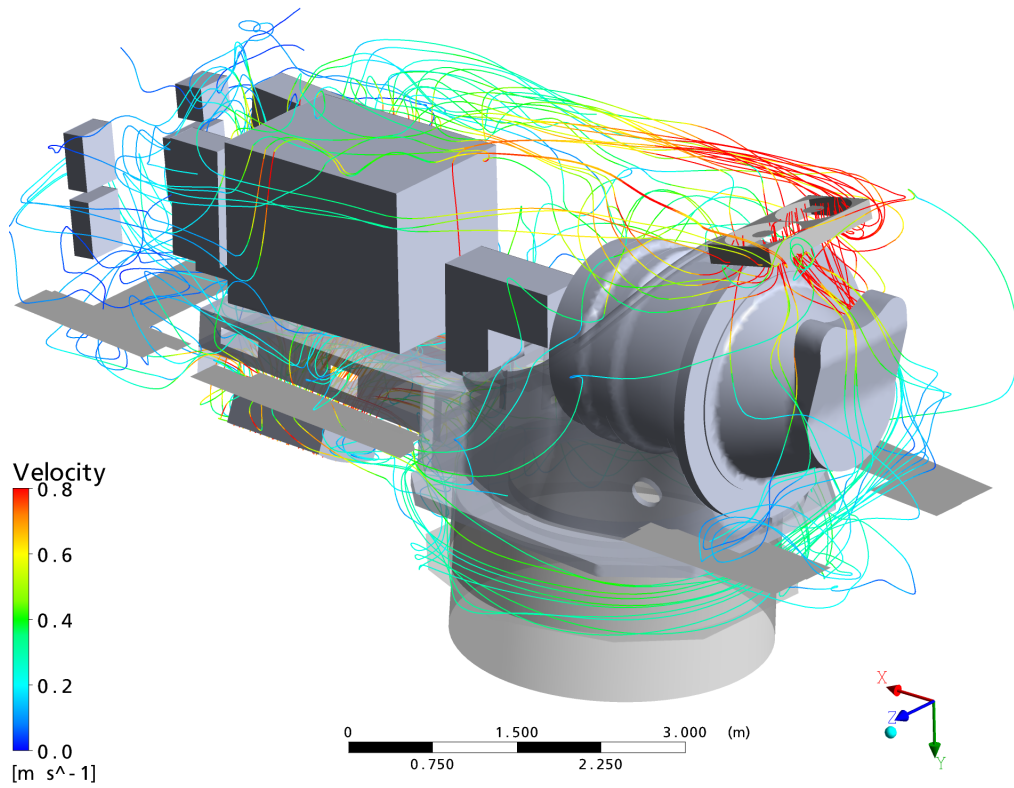**Figure 8.5:** Streamlines starting from the inlet at the tower
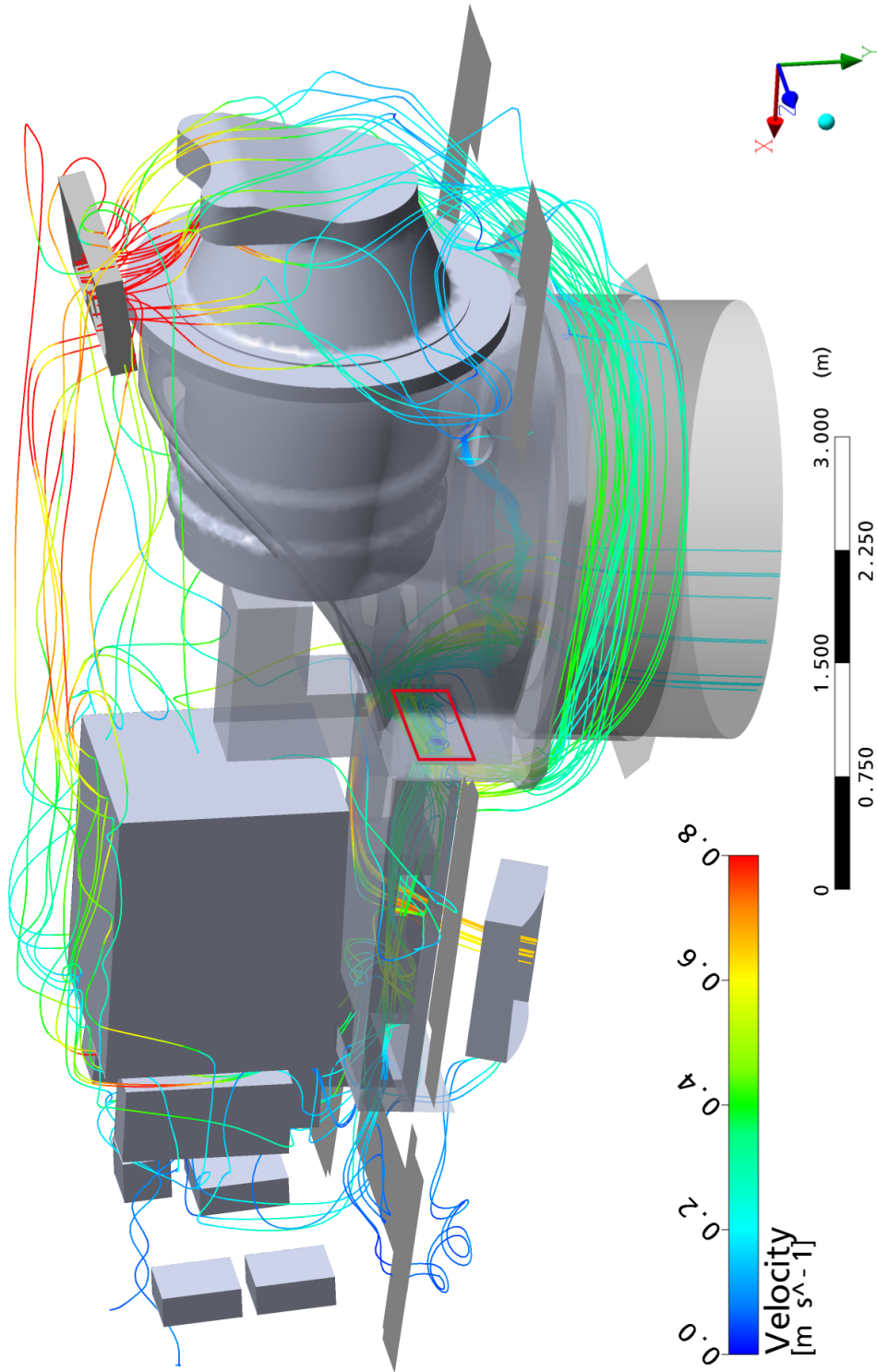
Figure 8.6: Streamlines starting from the connection of the mainframe and the generator support.
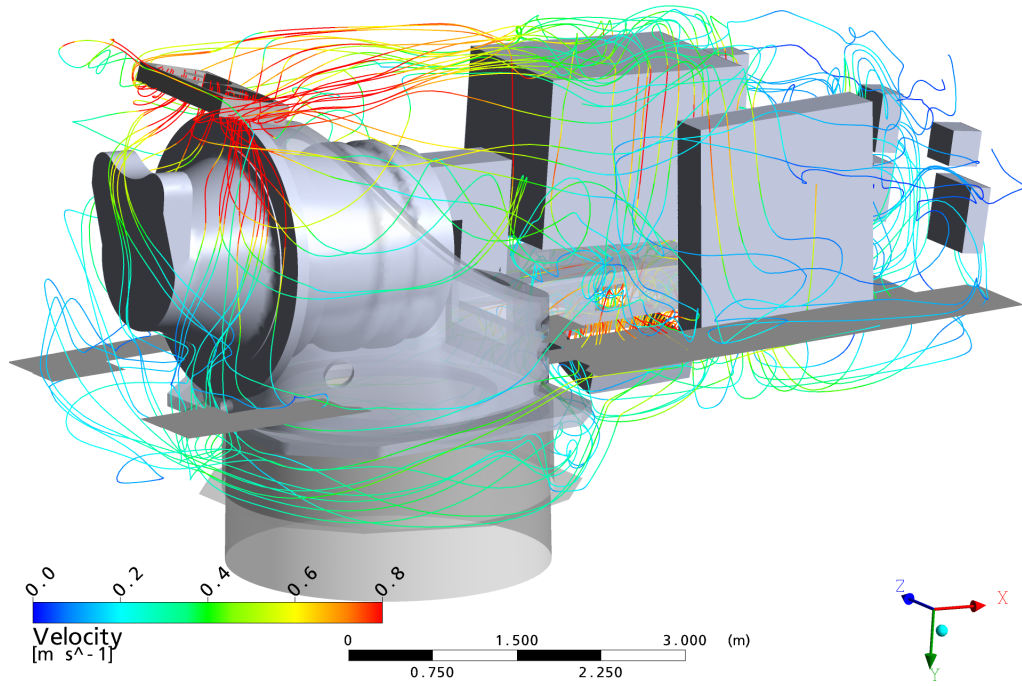
(a) Left view

(b) Right view

Figure 8.7: Streamlines starting from the inlet at the nacelle hull

8.4 Speed and Temperature Distribution at the Gearbox, its Oil Chiller and the Inlet at the Hull

Only the temperatures for the fluid domains are displayed in the following temperature plots. The temperature plots in figures 8.8, 8.10 and 8.12 at the sections through the flow field show temperature jumps where the domains *Vorne* and *Huelle* are connected with a GGI interface. The temperature jumps are due to interpolation between the surface grids at the interfaces, cf. chapter 4.1. In the figures, the temperature jumps are marked with arrows. The interpolation introduces a small numerical error at these locations. In the figures 8.8 and 8.10, however, a similar jump of temperature can be seen where the floor elements are situated, also marked with arrows. Temperature jumps are due to the floor elements at these locations which were modeled as thin adiabatic walls. They inhibit heat and mass transfer and, therefore, a slightly different temperature can be observed above and below the floor elements in some places. In figure 8.12 no such jump can be seen as no floor elements are situated in this place.

The velocity vector plots are placed at the same locations, showing the velocities projected onto the correspondent plane. The length of the vectors has been normalized to better visualize the flow directions. The color of the vectors represents the local flow speed. The legend has been limited to a maximum of 1.2 m/s.

8.4.1 Cross-Section at x=0.5 m

This vertical section of the front part of the nacelle shown in figure 8.8, cuts through the front part of the gearbox. It is placed right before the outlet fan and the oil-to-air heat exchanger. The temperature distribution shows low temperatures in the lower parts of the nacelle. The temperatures are very high in the thermal boundary layer of the gearbox. They locally exceed 60 °C. Right under the roof, the temperature rises and reaches values between 50 and 60 °C. The floor elements and the interpolation errors at the domain interface are clearly visible.

The velocity vector plot, figure 8.9, depicting the same location, shows the upwards directed stream around the gearbox, where buoyancy effects accelerate the flow. The flow situation is disordered in the upper part of the nacelle.
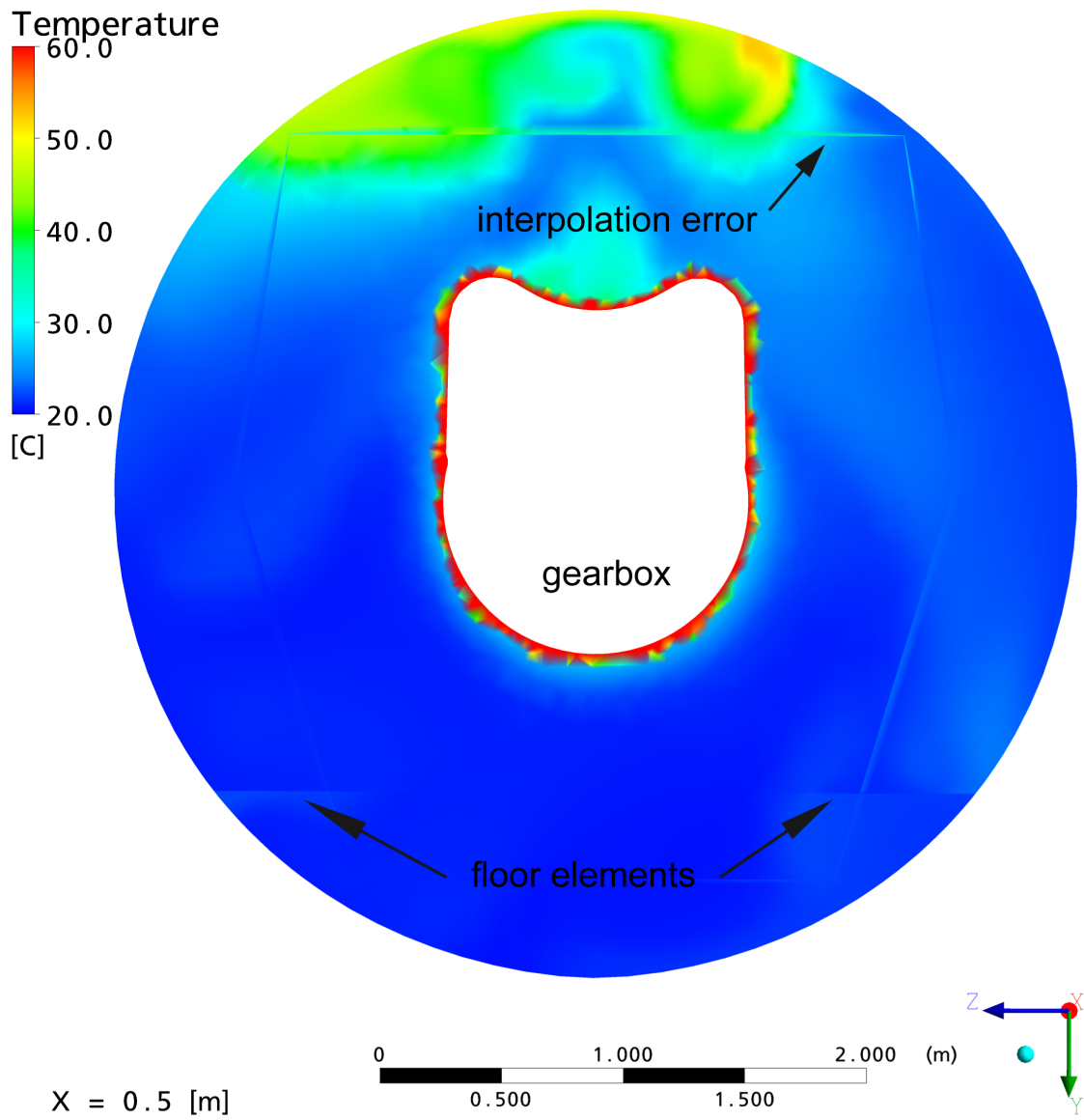
Figure 8.8: Temperature plot on vertical section through the nacelle, x=0.5 m
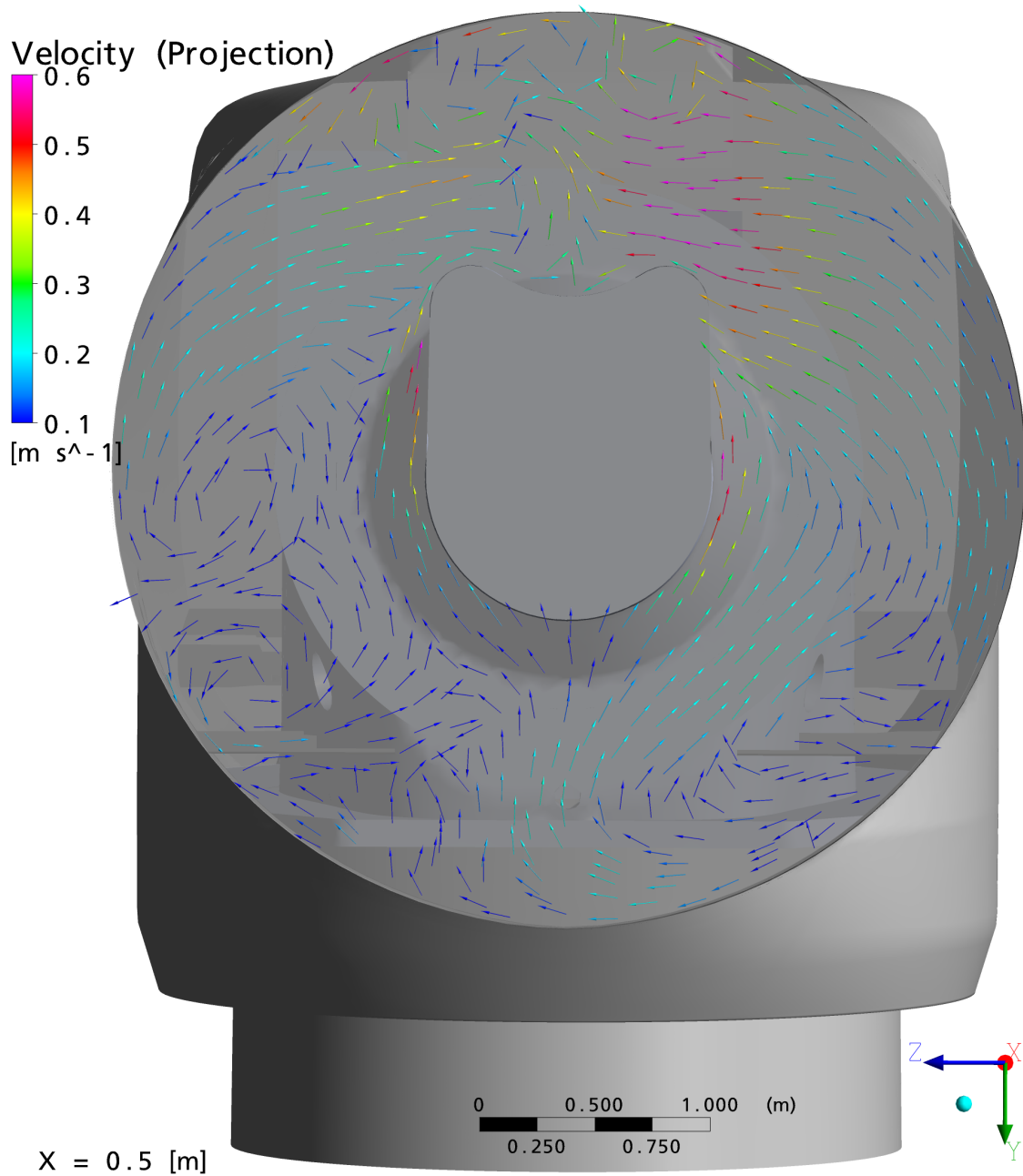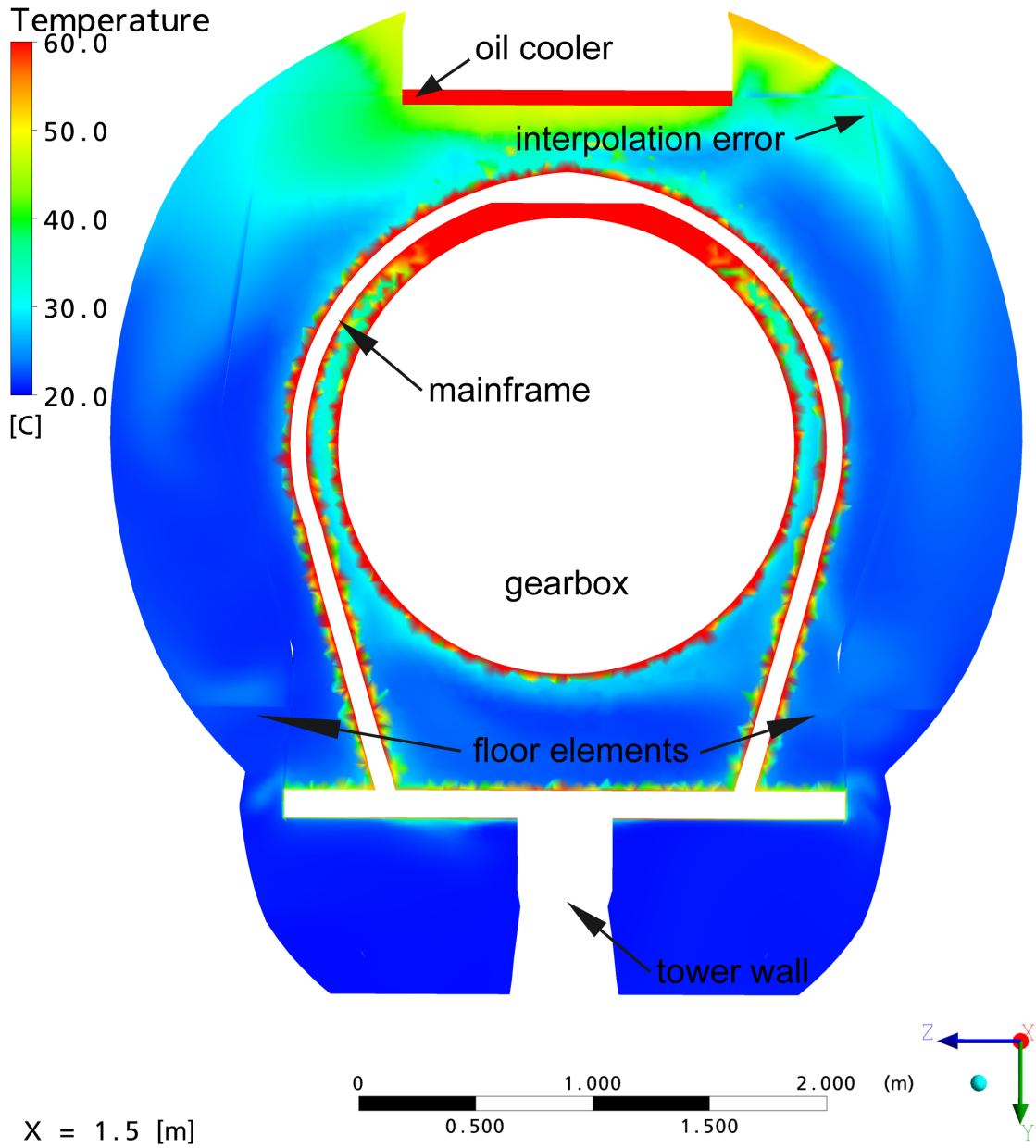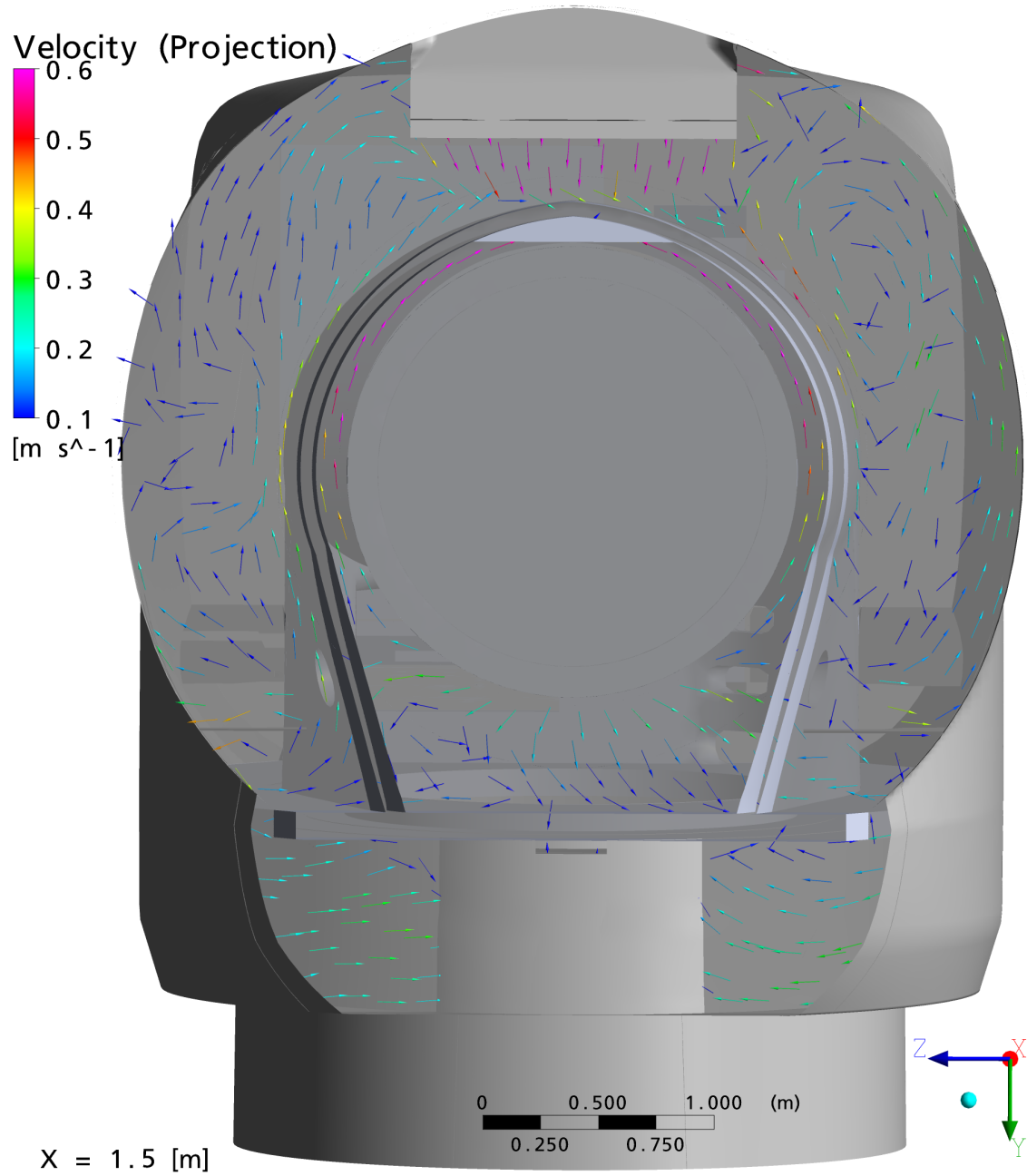
Figure 8.9: Velocity vector plot on vertical section through the nacelle, x=0.5 m

8.4.2 Cross-Section at x=1.5 m

The cross-section at x=1.5 m, figure 8.10, shows a cut not only through the gearbox, but also through the mainframe and the wall of the tower in the lower part. The hot oil-to-air heat exchanger leading into the not modeled outlet channel is also visible right at the boundary of the calculation area. The air temperatures are warmer around the heat exchanger and the fan in the upper part of the nacelle than they are in the lower areas. The warm air is coming from the rear parts of the nacelle where the generator and the converter box have heated up the air.

The temperatures around the gearbox are higher than in the previous figure 8.8. Areas of very hot air are visible in the clear space between the gearbox and the mainframe. The warm air moves upwards and is trapped in the cavity between the gearbox and the mainframe, very well visible in 8.14a. It remains there for a while and gets heated up.

The floor elements are clearly visible in this picture, as well as the fragments due to the interpolation error. The depiction of the temperatures around the gearbox and the mainframe are not as smooth as in the structured grid areas. The jagged depiction of the temperature is caused by the relatively big element size in the unstructured grid part *Vorne*, which contains the gearbox, compared to the fine element size in the structured grid part *Huelle*.

The vector plot figure 8.11 shows a very unstructured flow situation. The most proper flow structures are close to the surface of the gearbox and the mainframe, where buoyancy effects direct the flow paths upwards. A flow towards the middle of the nacelle around the tower below the mainframe is clearly visible.
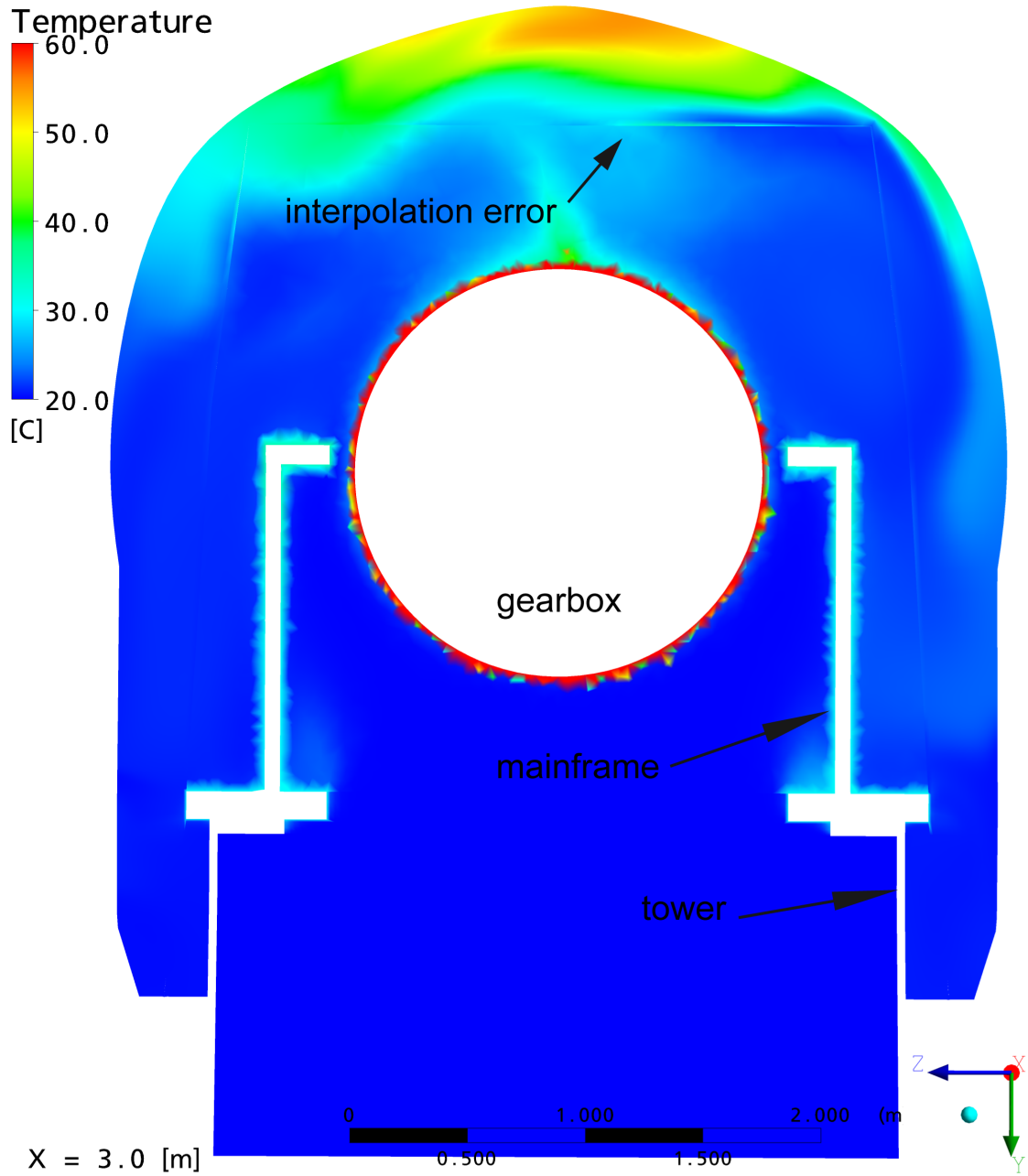
Figure 8.10: Temperature plot on vertical section through the nacelle, x=1.5 m

Figure 8.11: Velocity vector plot on vertical section through the nacelle, x=1.5 m

8.4.3 Cross-Section at x=3.0 m

A third cross-section of interest is displayed in figure 8.12. It is situated behind the outlet fans. The temperature plot shows a region of warm air under the roof. This warm air is mainly arising from the rear part of the nacelle, transporting the heat from the generator and the converter cabinet towards the outlet. The corresponding flow path is visible in the streamline plot in figure 8.7b. The hot air from the surface of the gearbox is rapidly mixed with cool air from the tower inlet due to the fast flow speeds in this area (cf. vector plot figure 8.13) so that only a small stream of moderately warm air originating from the gearbox surface is visible. The air temperatures around the mainframe are low compared to those around the gearbox, as the mainframe is already quite cool in this section.

The velocity vector plot, figure 8.13, shows the distinct jet of air originating from the tower inlet and passing through the mainframe upwards, circling the gearbox. In the upper part of the nacelle, this jet of air causes strong swirls, visible in figure 8.5a. The mainframe and the gearbox again cause a lift due to buoyancy. In the very low part around the tower, the air flow is rather unstructured.

Figure 8.12: Temperature plot on vertical section through the nacelle, x=3.0 m
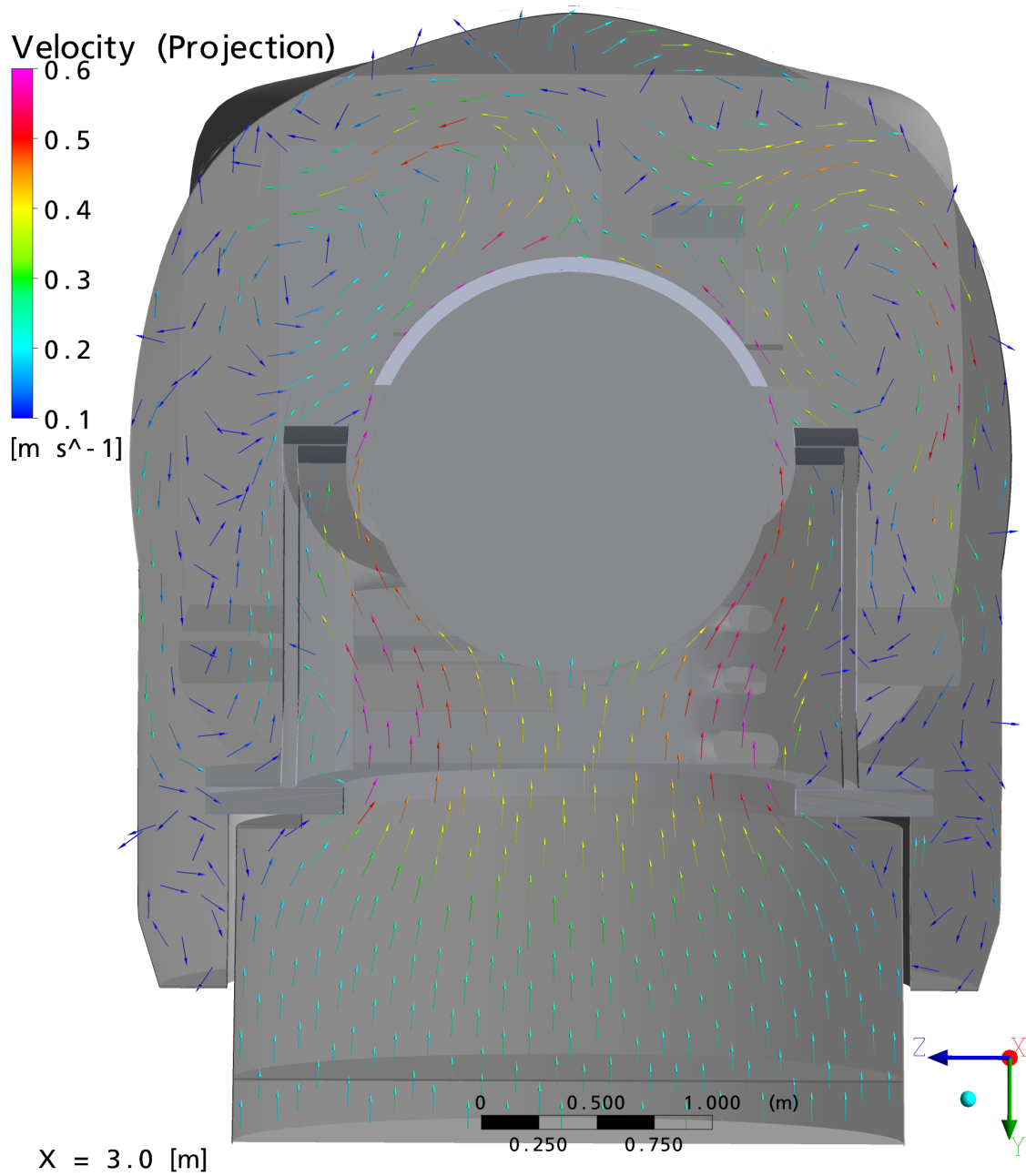
Figure 8.13: Velocity vector plot on vertical section through the nacelle, x=3.0 m

8.4.4 Cross-Section at z=-2.0 m

A section at z=-2.0 m was made in figures 8.14a and 8.14b to demonstrate the flow situation from the z-direction. From this direction, the warm volume of air in the rear part of the nacelle is very well visible. The air gets hotter above the generator and is advanced towards the outlet fans. Mixing with the large amount of relatively cool air from the gearbox takes place right before reaching the outlet fans. The heat-up in the oil-to-air chiller is clearly visible. The cavity where the air is being trapped and getting warm in the upper part of the gearbox can be seen. In the rear part, effects of the floor elements can be seen.

The vector plot 8.14b shows a very unstructured flow pattern in the rear part of the nacelle (left side of the image). The jet of air passing through the mainframe with high flow speeds is very well visible in the front. A flow path towards the outlet fans can be observed right under the roof of the nacelle. It brings the hot air from the generator and the converter cabinet to the outlet. The mixing swirl with the air from the gearbox can be seen. It partly originates from the cavity between mainframe and gearbox.
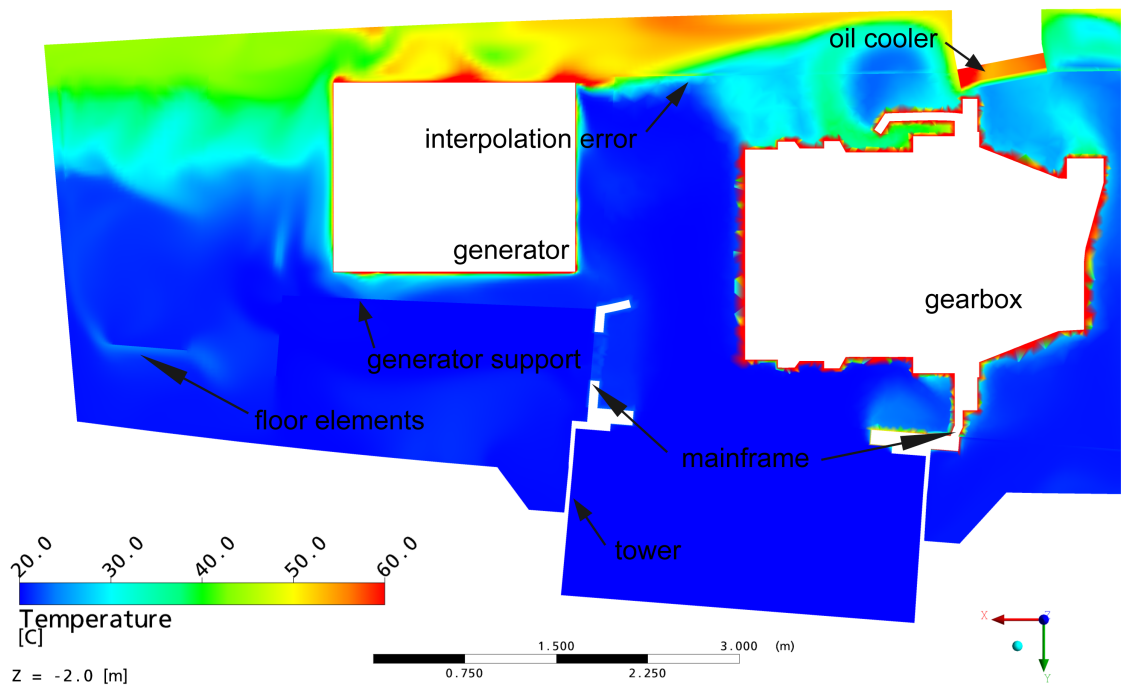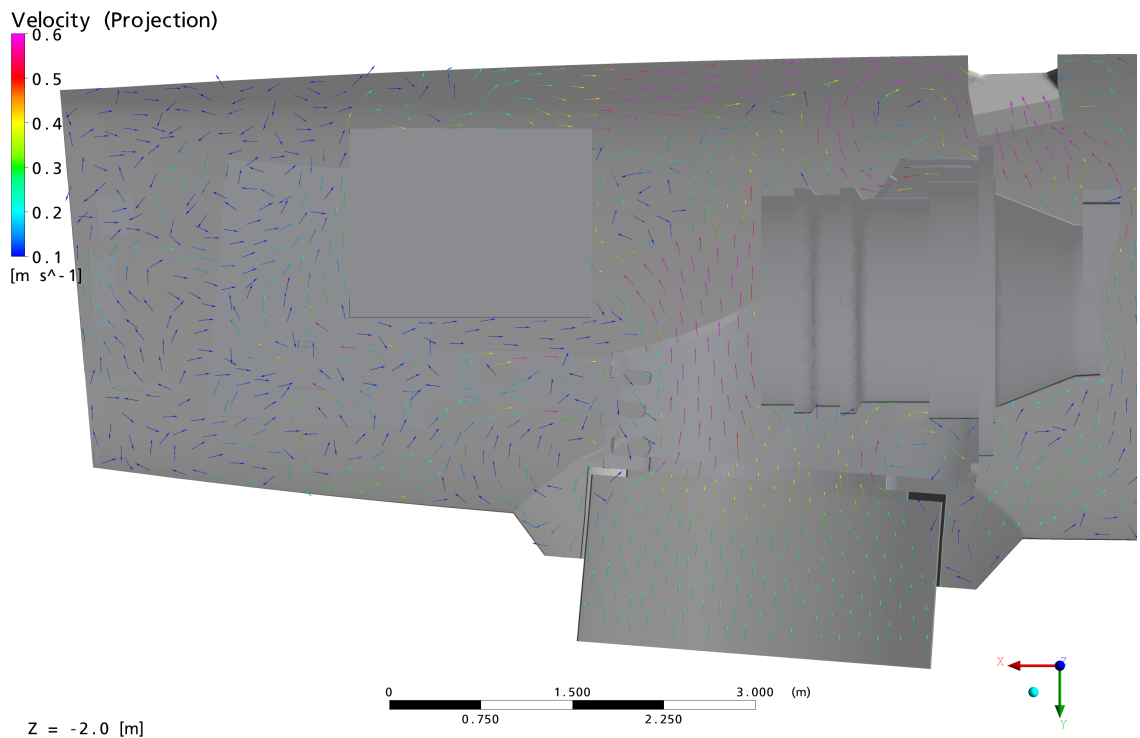
(a) Temperature plot

(b) Velocity vector plot

Figure 8.14: Vertical cross-section through the nacelle showing temperatures and velocities, z=-2.0 m

8.5 Temperature Distribution inside the Heat Sources

Although the temperature values inside the heat sources are to be treated with care, as they are much too high, the distribution of the heat can still be representative. It can show hot and cold spots. As an example, the surface of the gearbox model is shown in figure 8.15a and sections through it are shown in figure 8.15b. As already mentioned, the temperature values between 80 and 115 °C are much too high. The temperature distribution, however, shows that the rear part (right side in the figure) of the gearbox is about 10 to 15 °C hotter than the front part, although the rear part is situated directly above the tower inlet and the cool air streams around it quite fast. Firstly, this can be explained by the shape of the front part. The volume-to-surface ratio is more advantageous in the front than in the rear part. Secondly, the large flange acts as a cooling fin even more as its geometrical model is directly connected to the mainframe with a *solid-solid* interface, allowing heat conduction to take place. As a result, the mainframe gets quite warm although it is no heat source. The connection between the two solids could as well be defined as an adiabatic wall, so that no heat can be transferred through it. The reality lies between these two extremes.

The section through the gearbox in figure 8.15b demonstrates the temperature distribution inside the solid domain of the gearbox. In the inner rear part of the gearbox, a hot spot is visible. Again, the shape has to be made responsible for this, but also the way the gearbox was modeled. It is represented as a fully-fledged solid domain with no cavities, oil cooling or similar details. This is, of course, a rough simplification. Furthermore, the heat generation is uniformly distributed over the whole volume of the gearbox which is not true in real. An inhomogenous distribution of the heat could be modeled. However, no information was available on how the heat generation is actually distributed.
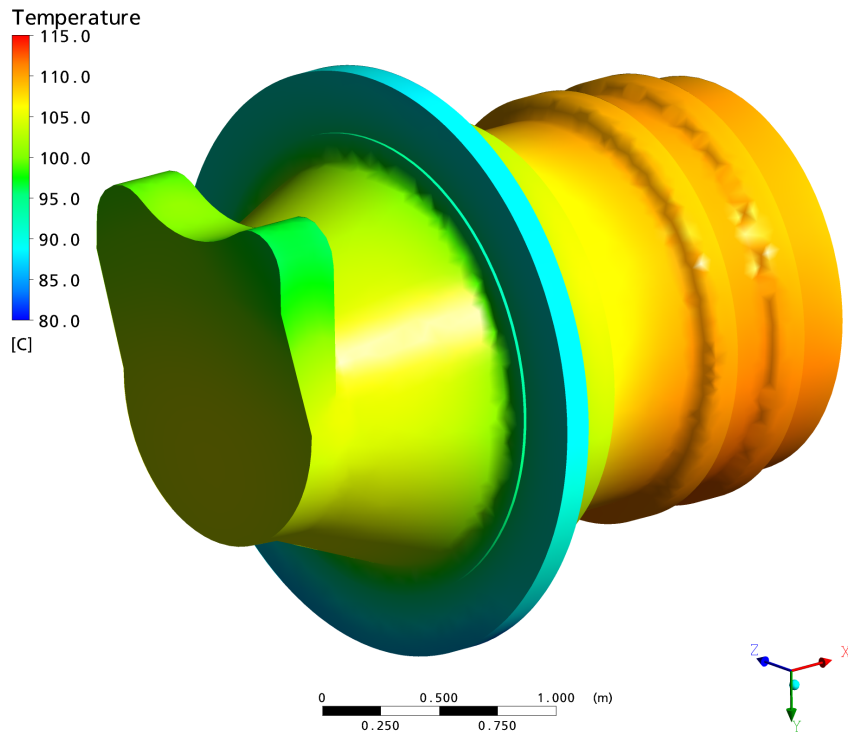
(a) Surface temperatures at the gearbox
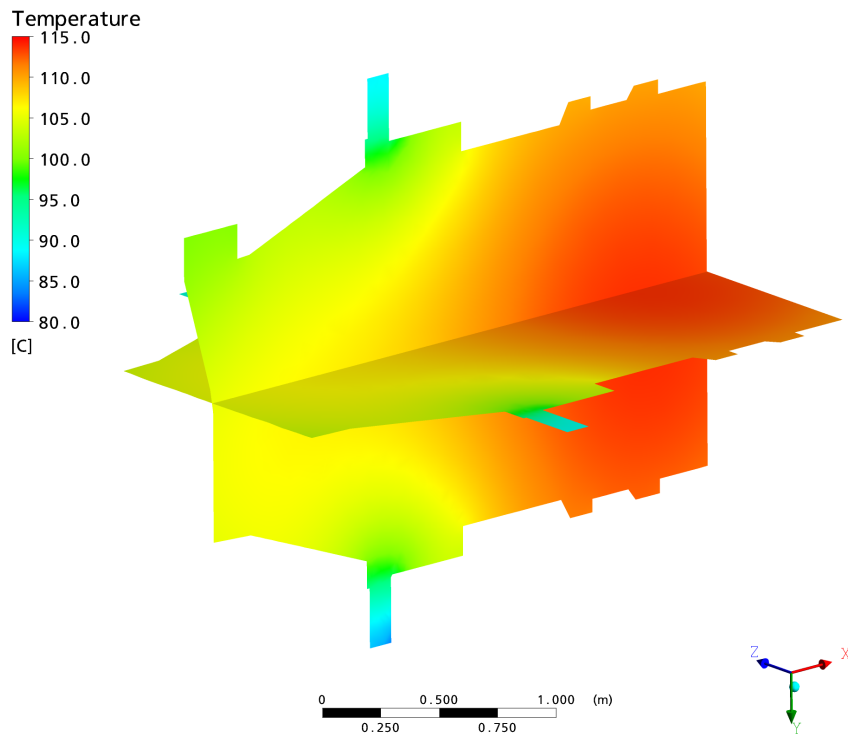
(b) Sections through the gearbox displaying the temperature distribution in the solid

Figure 8.15: Temperature at the gearbox surface and in the solid

8.6 Temperature Distribution at the Nacelle Hull

Figure 8.16 shows temperature contours for the hull of the nacelle. The represented hull temperatures do not comprise any heat loss towards the environment or gains through insolation, which certainly change the temperatures at the hull. This could be modeled by changing the boundary condition of the hull of the nacelle, which is currently defined as an adiabatic wall. The definition of a heat flux at the wall towards the outside could represent such a boundary condition. It would as well be interesting to analyze whether solar heat input towards the inside could be modeled in a similar fashion.

As expected, the lower part is cooler than the upper part where the air passing by the hull is already heated up by the heat sources. It is remarkable that the layer of warm air is thicker in the back (left side in the upper representation) than it is in the front, which was already visible in the analysis of the horizontal section planes in section 8.2. The high temperatures in the rear part is due to the low flow speeds in the rear part of the nacelle, which increases the mixing time and the time until the warm air is transported towards the outlet.

In the view from the top, a hot spot is visible in the lower part of the figure. It is situated above the generator. The numerical results show hull temperatures of up to 60 °C in this area. From there, the heat is transported with the air in direction of the outlet. The streamline plots show this flow path, too. On its way it is mixed with the relatively cool stream of air entering through the tower.

Figure 8.16: Temperature contours on the hull

9 Comparison with Measurements

The search for similar CFD calculations in the literature was not successful apart from a handful of publicized results in chinese language. Therefore, a comparison with measurement results was aspired. Windtec provided a set of data, which was measured on the similar wind energy converter *SG2000 Version 1*. A comparison of the mass flows inside the tower and the temperatures at the walls of the nacelle is presented in this chapter.

9.1 Description of the Setup

The main geometric difference between the two setups is, that the *SG2000* does not possess an inlet at the cover of the nacelle. Air is mainly entering the nacelle through the tower and through leakages, where the nacelle is connected to the tower and to the spinner. In addition to this, another oil chiller for the *supergear* is placed at the rear wall of the nacelle. The air that is passing this oil chiller is blown off into the environment.

The measurements were taken on May 19, 2010 between 9 am and 4 pm in Janov, Czech Republic. The height above sea level is $330\,\mathrm{m}$. The weather conditions were heavily cloudy with scattered rain showers, no insolation, with an outside temperature of about $5\,°\mathrm{C}$. The power production during the measurement varied from $500\,\mathrm{kW}$ to $900\,\mathrm{kW}$. Air speeds and temperatures were measured at a number of positions inside the tower and the nacelle. A thermal camera was used to measure the surface temperatures of the main components in the nacelle. [18]

A solution run with adapted boundary conditions was carried out to match the environmental conditions that were described above as good as possible. The inlet temperatures were adapted. In the measurement report, detailed data for the air temperatures inside the tower are presented. Air temperatures of $8\,°\mathrm{C}$ were measured at the highest platform under the entrance to the nacelle. This value was set as inlet boundary condition for the tower inlet. The inlet temperature for the opening at the cover was set to the outside air temperature of $5\,°\mathrm{C}$. The heat quantities released at the heat sources in the original setup in chapter 8 corresponds to a rated power production of $2000\,\mathrm{kW}$. Hence, the heat quantities needed to be adapted to the approximate average of $700\,\mathrm{kW}$, which were produced that day. The outlet air speed was not changed. According to AMSC Windtec, the operating point of the outlet blowers does not vary with the power production of the wind turbine.

The boundary conditions for this solver run are summarized in table 9.1. The solver setup is identical to the one for the analysis in chapter 8, see table 8.1. The geometry and the grid of the CFD model were not adjusted to the *SG2000* wind energy converter.

Table 9.1: Boundary conditions adapted to the conditions during the measurements

Boundary condition	
Outlet	
Normal speed	$3.3\,\mathrm{m/s}$
Inlet *Turm* and *Huelle*	
Type	opening
Relative pressure	0 Pa
Flow direction	normal to boundary
Static temperature *Turm*	$8\,°\mathrm{C}$
Static temperature *Huelle*	$5\,°\mathrm{C}$
Turbulence	medium, $5\,\%$
Heat sources with conjugate heat transfer	
FU (converter box)	$1360\,\mathrm{W}$
Generator	$3545\,\mathrm{W}$
Getriebe (gearbox)	$2945\,\mathrm{W}$
Kühler (gearbox oil chiller)	$23667\,\mathrm{W}$

9.2 Mass Flow at the Tower Inlet

The air speeds inside the tower were measured at several positions. At the two vents of the tower door, in height of 3 m in the middle of the tower and at a number of positions at the platforms inside the tower. For better comparison, the mass flow at the tower door was deduced from the averaged air speed, the area of the vents, the air temperature and the absolute air pressure. The air speeds at the two tower door vents were measured and averaged in the report. These are the only vents of the tower, hence the mass flow can be considered as constant until the connection with the nacelle, ignoring any leakages.

The volume flow produced by the outlet fans, which was used to determine the outlet air speed, was given only for the operating point of 2000 kW power production. According to Windtec, the operating point of the outlet blower set does not vary. Undocumented measurements of the air velocities at the outlet fans showed speeds around $3\,\mathrm{m/s}$. Consequently, the same resulting normal speed of $3.3\,\mathrm{m/s}$ was used as boundary condition at the outlet for this calculation, see table 9.1.

The CFD model represents the connection of nacelle and tower as a circular opening with the full diameter of the tower. Only the topmost part of the tower, approximately 1 m, is modeled and no platform or any other component, which would induce a pressure loss and a pressure difference compared to the opening at the cover of the nacelle, was comprised in the model. The mass flow at the tower inlet was evaluated. The comparison of the results is presented in table 9.2.

Table 9.2: Mass flow of air at the tower inlet

Air mass flow at the tower inlet		
	measurement	CFD result
mass flow	$0.41\,\mathrm{kg/s}$	$1.59\,\mathrm{kg/s}$

The resulting mass flow of the CFD simulation is about four times higher than the measured one at the similar wind energy converter, see table 9.2. This difference can be explained by three determining factors.

1. Leakage mass flows occur where the nacelle is connected to the tower and to the spinner. They were not taken into account. The leakage mass flows cannot be neglected, according to AMSC Windtec.

2. The pressure loss and the stack-effect due to the tower and its internals were not taken into account in the CFD calculation. If the pressure difference between tower inlet and the inlet at the cover were measured, it could easily be implemented through a change of boundary conditions.

3. The geometries of the CFD calculation representing the *WT2000* and the wind energy converter *SG2000*, where the measurements were taken, are not identical. The main differences were already described above.

The CFD calculation could be adapted to these circumstances by a change of boundary conditions and of the model geometry, provided that appropriate measurement data for the pressure difference and the leakage mass flows is available. Leakages were already roughly measured and documented in the report [18], but not taken into account in the CFD calculation.

The leakages and the geometric differences certainly are the most important reasons for this divergency. They not only have a big influence on the discrepancy of the mass flows discussed in this section, but also on the results in the rest of this chapter. Detailed information on the leakage mass flows and a more detailed geometric model for their implementation are needed to straighten this divergency.

9.3 Wall Temperatures

The wall temperatures were measured to get an idea of the heat being transported over the cover. The sampled points are displayed in figure 9.1. The results for the measurement and the CFD calculation are opposed in table 9.3.

The temperature level of the CFD result was expected to be a lot higher due to the disregard of heat transfer through the cover towards the environment. The heat loss over the cover was estimated to be about 15 kW in the Wikov report [18].

Due to the different geometries of the two cases, it is also not trivial to compare the distribution of the temperatures in the nacelle. In general, the wall temperatures are expected to be high close to the lossy power transforming components, which can be observed in the measurement data. The measured values at the roof over the gearbox and the generator are higher, compared to the values at the sidewalls and in the rear part of the nacelle. The temperatures of the CFD result for the sample points at the roof of the nacelle are generally higher than for the points situated at the side walls.

The points one, two and three come quite close to the measured values. These points are situated very far from differences of the geometry and therefore the CFD results match quite good with the measurements.

Close to point four, the jet of cold air, which is entering the nacelle through the tower, reaches the roof with hardly any interaction with the internals of the nacelle. Consequently, this point remains cold. This jet of cold air is also visible in 8.5b and discussed in the corresponding chapter. However, it presumably does not exist in real. Firstly, due to the drastically lower mass flow through the tower, and secondly due to additional components, that were left away during the simplification of the geometry.

The CFD results for the points five, six and seven show very high temperatures in comparison with the measurements. This can be due to the low flow velocities in the rear part of the nacelle, cf. chapter 8.3. The additional *supergear* chiller and the absence of the inlet at the cover certainly change the flow characteristics in the rear of the nacelle in a very decisive manner.

The results for the points eight to eleven come very close to the measured values. Due to buoyancy and the fact, that cold air enters at the bottom of the nacelle and leaves the nacelle at its top, the air is layered in the nacelle.
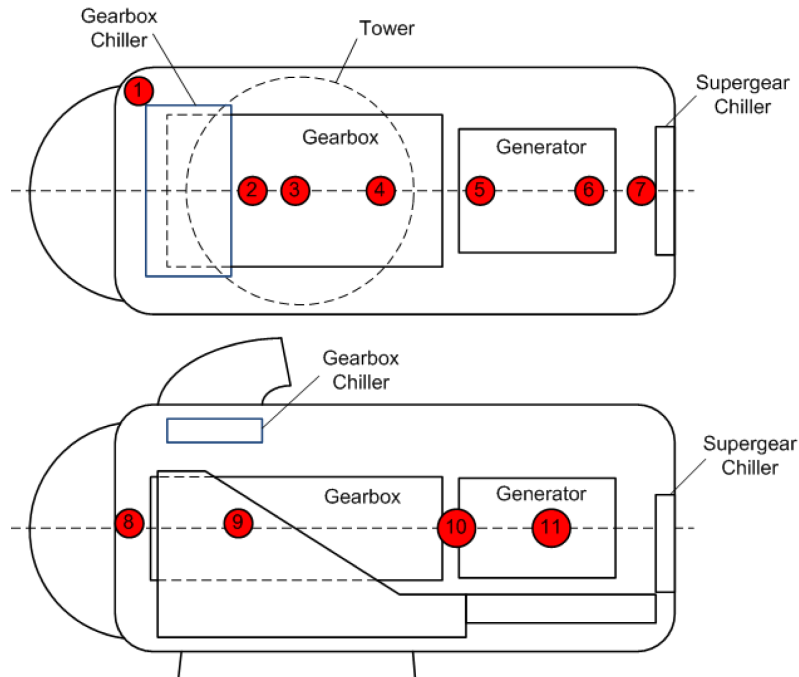
Figure 9.1: Position of the sampled points (taken from [18])

Table 9.3: Measured and calculated cover temperatures in comparison

Nacelle cover temperatures			
pos.	measurement	CFD result	description
1	7.9 °C	11.9 °C	roof: next to gearbox oil chiller
2	16.6 °C	14.1 °C	roof: just behind gearbox oil chiller
3	19.5 °C	11.5 °C	roof: centre over gearbox
4	15.6 °C	8.3 °C	roof: rear end of gearbox
5	10.8 °C	22.9 °C	roof: front end of generator
6	8.4 °C	20.1 °C	roof: rear end of generator
7	6.1 °C	19.2 °C	roof: over super gear unit oil chiller
8	5.0 °C	9.8 °C	side wall: intersection spinner - nacelle
9	7.3 °C	8.6 °C	side wall: next to centre of gearbox
10	7.5 °C	9.8 °C	side wall: between gearbox and generator
11	9.7 °C	10.3 °C	side wall: next to generator

9.4 Concluding Remarks

It is very difficult to compare the measurements with the CFD results because of the differences of the geometries and the ignorance of the volume flow of the leakages. A comparison with measurements taken from the actual *WT2000* wind energy converter is essential, in order to judge the quality of the presented model. Such a comparison will allow an evaluation, whether a CFD model, in general, can correctly predict the flow characteristics in such a complex geometry.

Some decisive discrepancies with the real situation can already be identified and possible solutions are listed below. These adaptions imply a change of boundary conditions in the most simple case. Others require a change of the geometric model and the grid. This list is not complete, but it contains the most urgent adaptions to be accomplished in future.

- Adjustment of the inlet boundary condition for the tower
- Correct model for the flow path from the tower inlet through the main frame up to the roof
- Implementation of the leakages in the model
- Modeling of the heat loss through the cover of the nacelle
- More detailed models for the heat sources
- Exact boundary condition for the outlet fans

10 Conclusions

No major problem arose during the modeling of the inside parts and the hull of the nacelle and a satisfactory model for the geometry was achieved. This model should be rediscussed in consultation with AMSC Windtec, evaluating whether too many details were left apart or if a further simplification is possible. After that, this model can be used for further calculations. It might be worth a try to totally rebuild the grid using unstructured meshing methods. The division of the geometry could be optimized or even avoided, resulting in fewer domain interfaces and fewer numerical errors due to interpolation.

The boundary conditions were basically defined by AMSC Windtec and only one operating point and environmental condition was used for the calculations in the main part of this diploma thesis. A variation of boundary conditions is easily possible, as shown in chapter 9. Hence, different operating conditions can be simulated and compared.

The heat sources were modeled using conjugate heat transfer. Another approach was not tried in accordance with AMSC Windtec. This model appears to be fully capable of capturing the interesting characteristics. The geometric simplicity of the models of the heat sources is to be charged for the lack of conformity with anticipated values for the surface and solid temperatures. In future, these models should be refined.

The modeling of the outlet blower set was treated with dissatisfying results as far as the calculation of a characteristic curve of the pressure loss for the fan and heat exchanger assembly is concerned. The implementation of the values provided by the manufacturer worked very well and a description was given for the necessary procedure.

The flow characteristics of interest inside the wind turbine nacelle were presented and discussed, keeping in mind that the accuracy of the results was *a priori* desired to be of qualitative nature. The latter point can be fulfilled with the outcome of this paper, whereas a study of flow details inside the nacelle using the presented results would certainly be unwise.

The verification of the model has been tried at hand of measurements, which were taken from a similar wind energy converter. The comparison was very difficult due to crucial differences of the geometries between model and sampled geometry. It was concluded that a comparison with the actual model still needs to be done in order to verify the quality of predictions and to ameliorate the CFD procedure.

An evaluation of the cooling and heating performance based on the current CFD model can not be recommended unless this verification and adaption loop is accomplished. Afterwards, a large number of further solution runs with adapted boundary conditions and modified geometry details can be conducted to test several arrangements and boundary conditions. A lot of work still needs to be done to achieve these goals. Nevertheless, a solid base has been laid in this paper.

References

[1] Ansys Europe Ltd: *Ansys CFX Documentation: Ansys CFX User-Guide.* 11.0, 1996-2006.

[2] BARDINA, J. E.; HUANG, P. G.; COAKLEY, T. J.: *Turbulence modeling validation, testing, and development.* In: *NASA TM*, 1997.

[3] BRADSHAW, P.: *The Best Turbulence Models for Engineers.* In: SALAS, M. D. (editor); HEFNER, J. N. (editor); SAKELL, L. (editor): *Modeling complex turbulent flows.* Kluwer Academic Publishers, p. 9–28, 1999.

[4] CEBECI, T.: *Analysis of turbulent flows.* Elsevier Science Ltd, 2004.

[5] COUAILLIER, V.: *Turbulent compressible flow computations.* In: PEYRET, R. (editor); KRAUSE, E. (editor): *Advanced turbulent flow computations.* Springer Verlag Wien, p. 279–315, 2000.

[6] FERZIGER, J.; PERIĆ, M.: *Numerische Strömungsmechanik.* Springer, 2008.

[7] HÖLLING, M.; HERWIG, H.: CFD-TODAY: *Anmerkungen zum kritischen Umgang mit kommerziellen Software-Programmpaketen.* In: *Forschung im Ingenieurwesen* p. 150–154, nr. 3, vol. 68, 2004.

[8] LESCHZINER, M.: *The Computation of Turbulent Engineering Flows with Turbulence-Transport Closures.* In: PEYRET, R. (editor); KRAUSE, E. (editor): *Advanced turbulent flow computations.* Springer Verlag Wien, p. 209–278, 2000.

[9] MENTER, F.; ESCH, T.; KONNO, B.; CARREGAL-FERREIRA, J.: *The SST Turbulence Model with Improved Wall Treatment for Heat Transfer Predictions in Gas Turbines.* In: *Proceedings of the International Gas Turbine Congress.* Tokyo: Gas Turbine Society of Japan, November 2003.

[10] MILES, J.; FARRASHKHALVAT, M.: *Basic Structured Grid Generation.* Butterworth Heinemann, 2003.

[11] NEALE, A.; DEROME, D.; BLOCKEN, B.; CARMELIET, J. : *Determination of surface convective heat transfer coefficients by CFD.* In: *11th Canadian Conference on Building Science and Technology*, 2007.

[12] OECD/IEA (editor): *Technology Roadmap - Wind Energy.* International Energy Agency, 2009.

[13] SAS IP, Inc: *Documentation for Ansys ICEM CFD/AI*Environment.* 11.0, 2007.

[14] SMAILI, A.; MASSON, C.; TALEB, S.; LAMARCHE, L. : *Numerical study of Thermal Behavior of a Wind Turbine Nacelle Operationg in a Nordic Climate.* In: *Numerical Heat Transfer, Part B*, p. 121–141, vol. 50, 2006.

[15] STAMOU, A. ; KATSIRIS, I. : *Verification of a CFD model for indoor airflow and heat transfer.* In: *Building and Environment*, vol. 41, 2006.

[16] TU, J.; YEOH, G.; LIU, C.: *Computational fluid dynamics: a practical approach.* Butterworth Heinemann, 2008.

[17] VIESER, W.; ESCH, T.; MENTER, F.: *Heat transfer predictions using advanced two-equation turbulence models.* In: *CFX Validation Report*, 2002.

[18] WIKOV: *Measurement report WW1-000043.01A for wind energy converter SG2000*, June 2010.

List of Figures

List of Tables